Magnetochiral Effects in Josephson Junctions and two-dimensional Josephson Junction Arrays

DISSERTATION ZUR ERLANGUNG DES DOKTORGRADES DER NATURWISSENSCHAFTEN (DR. RER. NAT.) DER FAKULTÄT FÜR PHYSIK

DER UNIVERSITÄT REGENSBURG

vorgelegt von

Simon Reinhardt

aus Regensburg

im Jahr 2024

Promotionsgesuch eingereicht am: 29. Oktober 2024

Die Arbeit wurde angeleitet von: Prof. Dr. Christoph Strunk

Prüfungsausschuss:

Vorsitzende: PD Dr. Magdalena Marganska-Lyzniak

Erstgutachter: Prof. Dr. Christoph Strunk

Zweitgutachter: Prof. Dr. Jaroslav Fabian

Weiterer Prüfer: Prof. Dr. Jörg Wunderlich

Datum Promotionskolloquium: 3. Februar 2025

Contents

1. Introduction

Currently there is a large increase of global data center energy consumption due to the boom of artificial intelligence (AI). As large computational resources are required for the training and deployment of large AI models, a further increase is expected in the next years [1]. At the same time the efficiency and performance of semiconductor technology is stagnating. In previous decades the performance of integrated circuits was improved by continuous downscaling of transistors. According to Moore's law, the number of transistors in an integrated circuit doubles every two years. While the miniaturization of transistors continues to this day, the performance of general purpose microprocessors has stagnated in the last 20 years [2] and further performance improvements are only possible with specialized domain-specific hardware and by optimizing efficiency of software and algorithms [3].

New concepts of information processing beyond semiconductor technology are needed for further increases in performance and energy efficiency. One of the most promising contenders is superconducting electronics. Superconductivity is a macroscopic quantum effect where charge carriers form a condensate which is described by a complex-valued order parameter. The superconducting condensate can carry dc current with zero dissipation. Another hallmark feature of superconductivity is the quantization of magnetic flux in units of $\Phi_0 = h/(2e) = 2 \times 10^{-15}\,\mathrm{Tm}^2$. The quanta of flux are used as carriers of information in many types of superconducting circuits. Superconducting electronics is part of the IEEE International Roadmap for Devices and Systems (IRDS) [4]. The most basic building block of both quantum and digital superconducting electronics is the Josephson junction. A Josephson junction is created when two superconductors are connected by a weak link, which can for example be an insulating layer or a normal conductor. As predicted by British theorist B. Josephson in 1962, electron pairs (also known as Cooper pairs) can be transmitted through the weak link. The resulting dissipation-free supercurrent is controlled by the difference of the superconducting phases in the two superconducting electrodes [5]. In the most simple case the Josephson supercurrent is given by the *current-phase relation*

$$I = I_c \sin(\Delta\varphi), \tag{1.1}$$

where I_c is the *critical current* of the weak link and $\Delta\varphi$ is the phase difference.

One example of superconducting digital electronics based on Josephson junctions is the Adiabatic Quantum-Flux-Parametron (AQFP) [6]. The basic logic element consists of two Josephson junctions in superconducting loops. Information is processed in the form of flux in the loops. According to Landauer's principle, the minimum dissipation per bit operation is given by $E = \ln(2)k_B T$ [7]. The energy dissipation per bit operation in AQFP logic approaches this thermodynamic limit. An experimental realization of AQFP logic gates with operating clock frequency of 1 GHz demonstrated switching energies of $24k_B T = 1.4\,\mathrm{zJ}$ per Josephson junction [8]. This record low energy consumption is many orders of magnitude below of what is achievable with semiconductor based CMOS logic.

A key challenge of superconducting electronics is the need of cryogenic temperatures. Most technically relevant realizations of Josephson junctions require a temperature below the boiling point of liquid helium (4.2 K). Because of this, it is expected that superconducting electronics will find its first use cases in niche applications. Examples are the control of superconducting quantum computers or applications in outer space where the ultra low power consumption is needed. Moreover, superconducting electronics suffers from a scalability problem. The basic logical elements require an area of many square micrometers.

It is clear that more fundamental research is needed to make superconducting electronics more competitive. One of the main avenues of research deals with the interplay of spin physics and superconductivity. The pairing of electrons (or holes) in the elemental low-temperature superconductors like aluminum or lead is of the spin-singlet type. This means that Cooper pairs are formed from singlet states of carriers with opposite spin and opposite momenta.

One famous example of a superconductor which cannot be described in this picture is $CePt_3Si$, discovered in 2004 [9]. This heavy fermion superconductor features strong spin-orbit interaction, which couples crystal momentum and electron spin. In $CePt_3Si$ the distorted crystal structure breaks the inversion symmetry in the z-direction. This results in spin-orbit coupling of the Rashba type. The most simple case of a two-dimensional Fermi surface with Rashba spin-orbit interaction is illustrated in Fig. 1.1. The Fermi surface is split into two non-degenerate bands where the direction of spin is locked perpendicular to the crystal momentum. $CePt_3Si$ features multiple properties which are not in agreement with spin-singlet pairing. For example, the critical magnetic field which is required to destroy the superconducting state exceeds the Pauli pair-breaking limit. Moreover, thermal conductivity and heat capacity measurements show that this superconductor does not form a complete energy gap in the density of states around the Fermi energy. Another peculiar feature is an antiferromagnetic transition below $T_N = 2.2\,\mathrm{K}$. Superconductivity sets in below $T_c = 0.7\,\mathrm{K}$ and seems to coexist with the antiferromagnetic order. It is expected that superconductivity in $CePt_3Si$ results from unconventional pairing which involves spin-triplet Cooper pairs. The spin-orbit coupling leads to a protection of these pairing type, resulting in the large critical magnetic fields.

More recently a new feature of superconductivity in materials with broken

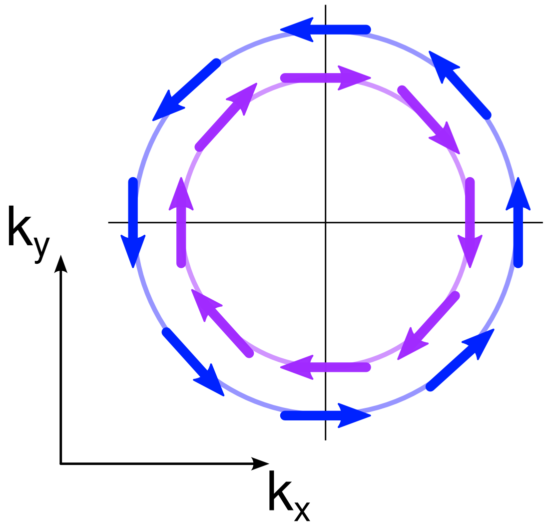

Fig. 1.1.: Fermi surface with helical bands resulting from Rashba spin-orbit coupling. The direction of the spin in the non-degenerate bands is locked, as indicated with arrows.

symmetries and large spin-orbit coupling has been discovered by the group of T. Ono at Kyoto University. In this work the authors studied the synthetic Rashba superlattice [Nb(1 nm)/V(1 nm)/Ta(1 nm)]$_n$ grown by molecular beam epitaxy [10]. This structure features the three group 5 transition metals with large superconducting transition temperatures (A table of the superconducting elements is shown in Fig. 1.2). This structure shows a "Superconducting diode effect": When applying an in-plane magnetic field perpendicular to a bias current, the critical current becomes dependent on the polarity of the bias. The Nb/V/Ta superlattice features spin-orbit coupling of the Rashba type which is caused by the broken structure inversion symmetry in the growth direction. The application of an in-plane magnetic field results in Zeeman interaction which breaks time-reversal symmetry. The diode effect is a consequence of the simultaneous breaking of both symmetries.

Shortly after the discovery of Ando *et al.* our work group at University of Regensburg observed a similar effect in Josephson junctions. The devices studied by our group were fabricated from hybrid superconductor-semiconductor structures featuring an thin aluminum film which is grown on a semiconducting heterostructure with an InAs quantum well. The InAs quantum well features strong Rashba spin-orbit coupling and close proximity of the quantum well to the superconductor results in an induced superconducting gap in the semiconductor. Our group observed both non-reciprocal inductance as well as a diode effect in the Josephson critical current [12]. This discovery adds both new functionality and raises fundamental questions on the interplay of spin degrees of freedom and superconductivity.

The work presented in this thesis continues the exploration of magnetochiral effects in Josephson junctions formed in Al/InAs hybrid structures. Chapter 2 gives an introduction to the theory of SNS Josephson junctions and describes

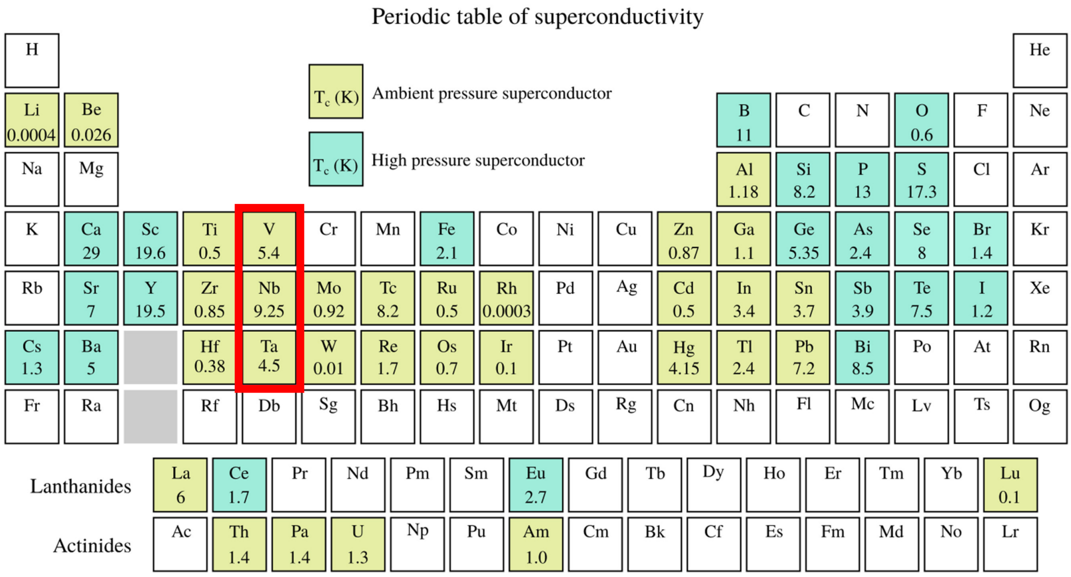

Fig. 1.2.: Periodic table of the elements. Ambient pressure superconductors are colored in yellow. The value given for each element is the superconducting transition temperature T_c. The red box highlights the three superconducting group 5 metals, V, Nb, and Ta, which were used for the ternary Rashba superlattice by Ando *et al.*. Adapted from [11] (licensed under CC BY 4.0).

the novel effects which arise in the presence of spin-orbit coupling and Zeeman fields. The experiment described in Chapter 3 enables the measurement of both anomalous Josephson effect and superconducting diode effect using an asymmetric SQUID device. Both effects can be tuned using a top gate which allows changing of the electron density in the Josephson junction. In the following chapters we study two-dimensional arrays of Josephson junctions (JJAs). Chapter 4 describes a novel type of vortex ratchet effect which arises in ballistic JJA devices. This magnetochiral effect is explained as a consequence of the anomalous phase shift. The inductance of Josephson vortices in two-dimensional arrays is studied in Chapter 5. We observe a characteristic behavior of vortex inductance as a function of frustration and observe nonreciprocal vortex inductance when applying in-plane magnetic fields. Finally, Chapter 6 studies the insulating behavior of the two-dimensional JJAs. The JJAs are tuned to the insulating regime by depleting the electron gas in the junctions with a gate electrode. In the insulating regime we observe critical threshold voltages caused by Coulomb blockade effects. Transport shows thermally activated behavior with an activation energy which depends both on the induced superconducting gap in the semiconductor and the electrostatic charging energy.

2. Introduction to the physics of SNS Josephson junctions

The physics of superconductor/normal conductor/superconductor (SNS) Josephson junctions is a large area of mesoscopic physics research, which is driven by the various different types of materials that can be used as weak links. In general, the current-phase relation (CPR) will reflect the electric properties of the normal conductor (N) and/or its interfaces to the superconducting electrodes.

Going from general to specific, in this introductory chapter we roughly follow the history of the theoretical models developed for the study of SNS junctions. The starting point is the description of weak links based on the Ginzburg-Landau theory. An important result is the Ambegaokar-Baratoff formula, which relates the product of critical current and normal state resistance of a junction to the superconducting gap in the electrodes. A crucial feature of SNS junctions is the emergence of high transparency channels. The high transparency results in non-sinusoidal CPRs with higher harmonics. The first explanation for this behavior was given by Kulik and Omel'yanchuk in the so called "KO-1" theory of diffusive weak links, and we will give a short derivation starting from the Usadel equation, which is the general description of superconductors in the diffusive regime. The more general theory of Furusaki and Beenakker allows the description of junctions with arbitrary transparency and is based on the Bogoliubov-de Gennes mean-field theory. In the ballistic regime the microscopic picture of transport through the junction is described by discrete Andreev bound states in the normal weak link. We then discuss the recent developments in the theory of SNS junctions in systems with broken symmetries. Breaking structure inversion symmetry (SIA) results in spin-orbit coupling (SOC) of the Rashba type. Time reversal symmetry can be broken by a Zeeman term which results when an in-plane magnetic field is applied to a two-dimensional electron gas. The novel effects resulting from the broken symmetries are the anomalous phase shift (φ_0-shift) and the Josephson diode effect (JDE). The recent discovery of these effects triggered a surge of experimental and theoretical activity in the field of superconductivity. A theoretical description of the anomalous phase shift and the Josephson diode effect is given by a recently developed model of our colleague A. Costa from the group of J. Fabian. This model captures all necessary requirements for the description of ballistic junctions formed from a proximitized planar electron gas with spin-orbit interaction and is in good qualitative agreement with experiment.

2.1. Weak links: Ginzburg-Landau theory

In the phenomenological Ginzburg-Landau (GL) theory, the superconducting condensate is described by the complex order parameter ψ. A more detailed introduction to the GL theory can found, e.g., in [13]. The free energy of the superconducting system is given by

$$f_s = f_n + \alpha|\psi|^2 + \frac{\beta}{2}|\psi|^4 + \frac{1}{2m}|(-i\hbar\nabla - e^*\vec{A})\psi|^2 + \frac{\vec{B}^2}{2\mu_0\mu_r} \tag{2.1}$$

with the GL coefficients

$$\alpha(t) = \alpha'(t-1);\ \alpha' > 0 \tag{2.2}$$
$$\beta(t) = \text{const.} \tag{2.3}$$

For a homogeneous superconductor and no gradients of the order parameter, the minimum of the free energy is found for

$$|\psi|^2 = |\psi_\infty|^2 = -\frac{\alpha}{\beta}. \tag{2.4}$$

Near T_c the order parameter scales as $|\psi|^2 \sim (1-t)$. By minimization of the GL free energy functional, one obtains the first GL equation

$$\alpha\psi + \beta|\psi|^2\psi + \frac{1}{2m}(-i\hbar\vec{\nabla} - e^*\vec{A})^2\psi = 0. \tag{2.5}$$

Minimization with respect to the vector potential provides the second GL equation for the supercurrent

$$\vec{J} = \frac{e^*|\psi|^2}{m}(\hbar\vec{\nabla}\varphi - e^*\vec{A}). \tag{2.6}$$

2.1.1. Coherence length

Without a magnetic vector potential, the first GL-equation is a real differential equation. Setting $f = \psi/\psi_\infty$ we get

$$\frac{\hbar^2}{2m|\alpha|}\Delta f + f - f^3 = 0. \tag{2.7}$$

We find the characteristic length scale of variations in f, the GL coherence length, as a function of the reduced temperature $t := T/T_c$

$$\xi(t)^2 = \frac{\hbar^2}{2m|\alpha(t)|} \sim \frac{1}{1-t}. \tag{2.8}$$

From BCS theory it is found that near T_c the coherence length is given by

$$\xi(t) = 0.74 \frac{\xi_0}{(1-t)^{1/2}} \qquad \text{pure limit} \tag{2.9}$$

$$\xi(t) = 0.855 \frac{(\xi_0 l)^{1/2}}{(1-t)^{1/2}} \qquad \text{dirty limit} \tag{2.10}$$

$$\tag{2.11}$$

with the mean free path l and the BCS coherence length $\xi_0 = \frac{\hbar v_F}{\pi \Delta(0)}$. The dirty limit applies if $l \ll \xi_0$, which is the case for most thin-film metallic superconductors. To give an example, we show how to calculate ξ_0 for aluminum. The value for the Fermi velocity is $v_F = 1.6 \times 10^6\,\mathrm{m/s}$ [14]. For the gap we use the BCS value $\Delta(0) = 1.76\, T_c$, so that

$$\xi_0 = \frac{2.2\,\mathrm{\mu m}}{T_c/K}. \tag{2.12}$$

For a typical value of our thin aluminum films the critical temperature is $T_c = 1.5\,\mathrm{K}$, giving $\xi_0 = 1.5\,\mathrm{\mu m}$.

2.1.2. The current-phase relation: Weak links in the Ginzburg-Landau theory

We consider a weak link with length $L \ll \xi$ between superconducting banks. The phase of the order parameter is set to $\varphi(x=0) = 0$ on the left bank and $\varphi(x=L) = \Delta\varphi$ on the right bank. As shown above, the first GL equation is given by

$$\xi^2 \frac{d^2}{dx^2} f + f - f^3 = 0$$
$$\text{with } f := \psi/|\psi_\infty|.$$

For a short weak link with $L \ll \xi$, the first term in the GL equation will be much larger than f and f^3 so that the GL equation simplifies to

$$\frac{d^2}{dx^2} f = 0$$

The solution for the boundary conditions $f(x=0) = 1$ and $f(x=L) = e^{i\Delta\varphi}$ is

$$f(x) = \frac{x}{L}(e^{i\Delta\varphi} - 1) + 1 := cx + 1.$$

The current density in the weak link is found from the second GL equation

$$J \sim -\frac{i}{2}\left(f^* \frac{d}{dx} f - f \frac{d}{dx} f^*\right) = \frac{\sin(\Delta\varphi)}{L}$$

and the current-phase relation (CPR) is given by

$$I(\Delta\varphi) = I_c \sin\Delta\varphi.$$

The free energy of the junction reads as

$$F = \text{const.} - E_j \cos\Delta\varphi$$

with the Josephson energy

$$E_j = \frac{\hbar I_c}{2e}.$$

The supercurrent can be obtained from the free energy using the thermodynamic relation

$$I(\Delta\varphi) = \frac{2e}{\hbar}\frac{dF}{d(\Delta\varphi)}. \tag{2.13}$$

For tunnel junctions Ambegaokar and Baratoff have found the following relation for the product of critical current and normal state resistance:

$$I_c R_n = \frac{\pi\Delta(T)}{2e}\tanh\frac{\Delta(T)}{2k_B T}. \tag{2.14}$$

For $T \sim T_c$ this simplifies to

$$I_c R_n = \frac{2.34 k_B \pi}{e}(T_c - T). \tag{2.15}$$

As will be shown below, this result only holds for tunneling junctions. For diffusive and ballistic SNS junctions larger values of $I_c R_n$ are possible.

2.2. Current-phase relation of diffusive SNS weak links at arbitrary temperature

The GL theory discussed above is only valid when the temperature is close to the critical temperature. The first theory of SNS junctions valid at arbitrary temperatures was developed by Kulik and Omel'yanchuk [15, 16, 17]. This model, which describes junctions in the diffusive limit, is often referred to as "KO-1". The derivation of the KO-1 model starts with the Usadel equations, which give a semiclassical description of disordered superconductors. In the Usadel theory the condensate is encoded in the complex functions $F(\omega, x)$ and $G(\omega, x)$ which are related by

$$G(\omega, x) = \sqrt{1 - |F(\omega, x)|^2} \tag{2.16}$$

The Usadel equation is given by

$$2\omega F(\omega,x) - D\frac{d}{dx}\left(G(\omega,x)\frac{dF(\omega,x)}{dx} - F(\omega,x)\frac{dG(\omega,x)}{dx}\right) = 2\Delta(T,x)G(\omega,x), \tag{2.17}$$

where the diffusion constant is $D = \frac{1}{3}v_F^2\tau$ and the gap parameter $\Delta(T,x)$ is determined self-consistently

$$\Delta(T,x)\log(T_c/T) = \pi k_B T \sum_n \left(\frac{\Delta(T,x)}{\hbar\omega_n} - F(\omega_n,x)\right). \tag{2.18}$$

The sum runs over the fermionic Matsubara frequencies $\hbar\omega_n = (2n+1)\pi k_B T$ (where $n = 0,\ 1,\ 2,\ \ldots$). For a spatially homogeneous system without applied current this gives the well-known temperature dependence $\Delta(T)$ found from BCS theory. A useful approximation over the whole temperature range is given by

$$\Delta(T) \sim \Delta(0)\left(\cos\left(\frac{\pi T^2}{2T_c^2}\right)\right)^{1/2} \tag{2.19}$$

with $\Delta(0) = 1.76\, k_B T_c$ for weak-coupling BCS superconductors.

The supercurrent density $j_s(x)$ is found from the second Usadel equation

$$j_s(x) = \frac{\sigma_N \pi T}{e}\sum_\omega \mathrm{Im}\left(F^*\frac{d}{dx}F\right). \tag{2.20}$$

For a given geometry the second order Eq. (2.17) can be solved for all n after imposing boundary conditions for $F(\omega,x)$ and $\Delta(x)$. For an SNS junction with the N-region at $|x| < L/2$, the boundary conditions for $F(x)$ and $\Delta(x)$ are chosen as

$$\Delta(\pm L/2, T) = \Delta(T)e^{\pm i\varphi/2} \tag{2.21}$$

$$F(\omega, x = \pm L/2) = \frac{\Delta(T)}{\sqrt{\hbar^2\omega^2 + \Delta(T)^2}}e^{\pm i\varphi/2}. \tag{2.22}$$

For short junctions ($L \ll \xi$) the resulting supercurrent as a function of phase bias is

$$I(\varphi) = \frac{4\pi k_B T\Delta(T)}{eR_N}\sum_\omega \frac{\cos(\varphi/2)\arctan(\Delta(T)\sin(\varphi/2)/\delta)}{\delta} \tag{2.23}$$

with $\delta := \sqrt{\Delta(T)^2\cos^2(\varphi/2) + \hbar^2\omega^2}$. The current-phase relation at a given temperature can be found by performing the sum over Matsubara frequencies numerically. The resulting CPRs are shown in Fig. 2.1. For temperatures close to T_c the sinusoidal CPR from the GL theory is recovered. For $T \ll T_c$ the CPRs are strongly skewed. The maximum critical current at $T = 0$ is given by $I_c(T = 0) \sim 1.32\frac{\pi\Delta(0)}{2eR_N}$, exceeding the value of the Ambegaokar Baratoff formula. In the limiting case $T \ll T_c$ the sum over ω in Eq. (2.23) can be approximated by an integral, resulting in the analytical formula

$$I(\varphi, T = 0) = \frac{\pi\Delta(0)}{eR_N}\cos(\varphi/2)\,\mathrm{artanh}(\sin(\varphi/2)). \tag{2.24}$$

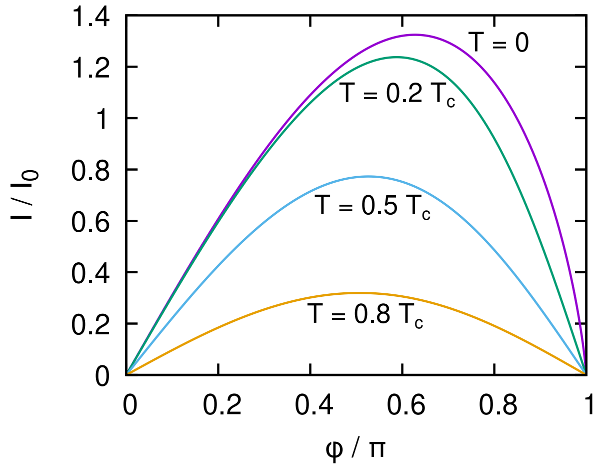

Fig. 2.1.: Current-phase relation from the KO-1 model for different temperatures. The current is given in units of $I_0 = \frac{\pi\Delta(0)}{2eR_N}$.

2.2.1. Short SNS junctions with arbitrary transparency

Ballistic superconducting point contacts where the weak link is described by a delta-like potential barrier were first studied by Haberkorn et al. [18]. The CPR for the SNS weak link with arbitrary disorder was obtained by Furusaki et al. [19, 20] and Beenakker [21] using the Bogoliubov-de Gennes (BdG) mean-field theory. The real-space BdG Hamiltonian is given by

$$H_{BdG}(x, y) = \begin{pmatrix} H_N(x, y) & \Delta(x, y) \\ \Delta^*(x, y) & -H_N(x, y), \end{pmatrix} \tag{2.25}$$

which is a complex 2×2 matrix. The normal state Hamiltonian is given by

$$H_N(x, y) = -\frac{\hbar^2(\partial_x^2 + \partial_y^2)}{2m^*} + U(x, y) - \mu. \tag{2.26}$$

The spectrum is found by solving the eigenvalue problem

$$H_{BdG}(x, y)\begin{pmatrix} u(x, y) \\ v(x, y) \end{pmatrix} = E\begin{pmatrix} u(x, y) \\ v(x, y) \end{pmatrix}. \tag{2.27}$$

The weak link is located at $0 < x < L$. The pair potential $\Delta(x, y)$ is then chosen as

$$\Delta(x, y) = \Delta(x) = \Delta_0(\theta(-x) + \exp(i\varphi)\theta(x - L)), \tag{2.28}$$

which is referred to as the step-function model. The pair potential will actually change on a length scale given by ξ. The step-function model is expected to give a good description if the length L is considered an effective length of the junction. The current-phase relation is obtained from the free energy $F(\varphi)$

$$I(\varphi) = \frac{2e}{\hbar}\frac{dF(\varphi)}{d\varphi}. \tag{2.29}$$

The free energy is found from the spectrum of the BdG Hamiltonian:

$$F = -2T \sum_{\varepsilon>0} \log(2\cosh(\varepsilon/(2T))) + \text{const.} \tag{2.30}$$

At $T = 0$ the free energy is simply the sum of the eigenenergies: $F = -\sum_{\varepsilon>0} \varepsilon$. In the approach of Beenakker the energy spectrum is obtained from the scattering matrix of the normal region. The transmission through the normal region is described by a transmission matrix t_{12}. In the short junction limit the discrete part of the energy spectrum is given by the values

$$\varepsilon_p = \Delta(T)\sqrt{1 - \tau_p \sin^2(\varphi/2)}, \tag{2.31}$$

where $\tau_p > 0$ are the eigenvalues of the positive-definite Hermitian matrix $t_{12}t_{12}^\dagger$. The corresponding current is

$$I_{\tau_p}(\varphi) = \frac{e\Delta(T)}{2\hbar}\frac{\tau_p \sin(\varphi)}{\sqrt{1 - \tau_p \sin^2(\varphi/2)}} \tanh\left(\frac{\Delta(T)\sqrt{1 - \tau_p \sin^2(\varphi/2)}}{2T}\right) \tag{2.32}$$

and for an ensemble of modes τ_p the CPR is found by summing over all modes

$$I(\varphi) = \sum_p I_{\tau_p}(\varphi) \tag{2.33}$$

CPRs $I_\tau(\varphi)$ of a single mode are plotted in Fig. 2.3 for different values of transparency and temperature.

The resulting spectrum of H_{BdG} as a function of phase bias is shown in Fig. 2.2. The discrete part of the spectrum consists of the energy levels of the Andreev bound states (ABS) with $|E| < \Delta$. The ABS are spatially confined in the weak link. The states of the continuous part of the spectrum are extended plane wave solutions with $|E| > \Delta$. In the short junction limit the Josephson current is carried only by the discrete Andreev bound states. For perfect transmission ($\tau = 1$) the critical current of a single bound state is given by the critical current quantum $e\Delta/\hbar$.

Due to the non-linear dependence of the critical current of a junction on the values of τ_p, it is in general not possible to find the critical current from the

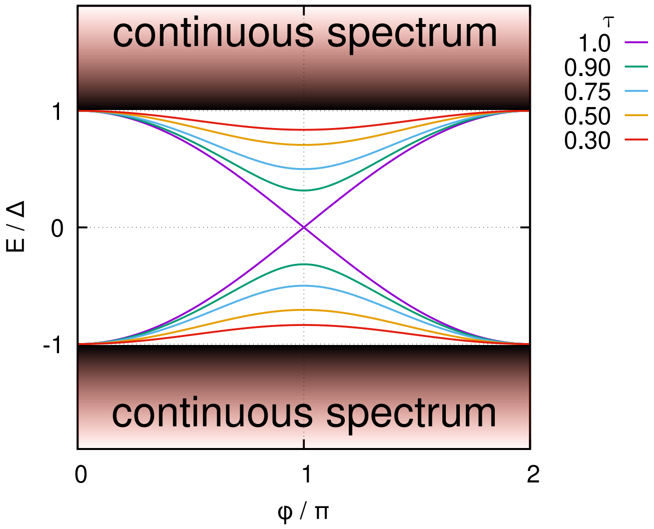

Fig. 2.2.: Discrete and continuous energy spectrum as a function of phase bias. The discrete energy levels of Andreev bound states are shown for different values of the transmission parameter τ.

normal state conductivity of the weak-link without knowing the distribution of the mode transmissions.

For junctions with a large number of channels the summation in Eq. (2.33) can be replaced by an integral, i.e., $I(\varphi) = \int \rho(\tau) I_\tau(\varphi)\, d\tau$, where $\rho(\tau)$ is the transmission eigenvalue density. For disordered weak links the universal distribution function of channel transparency is given by [22, 17]

$$\rho(\tau) = \frac{\pi\hbar G}{e^2} \frac{1}{\tau\sqrt{1-\tau}}$$

where $G = 1/R$ is the conductivity of the weak link. This distribution has peaks at both zero and unity transmission. The requirements for this result are homogeneous disorder and a mean free path shorter than the junction length. It also requires transparent interfaces between the leads and the normal region. For the disordered weak link the current-phase relation for $T = 0$ can now be found by integration

$$\begin{aligned} I(\varphi, T=0) &= \int_0^1 \rho(\tau) I_\tau(\varphi, T=0)\, d\tau = \\ \frac{\Delta(0)\pi G}{2e} \int_0^1 &\frac{\sin(\varphi)}{\sqrt{1-\tau}\sqrt{1-\tau\sin^2(\varphi/2)}} d\tau = \\ &\frac{\Delta(0)\pi G}{e} \cos(\varphi/2)\, \mathrm{artanh}(\sin(\varphi/2)), \end{aligned}$$

which is precisely the result obtained from the KO-1 model. We can define an effective value τ of transmission for the diffusive junction by fitting this CPR with the single-mode CPR $I_\tau(\varphi)$. As shown in Fig. 2.3**c**, a fit to the KO-1 model with reasonable matching is found for $\tau \sim 0.77 \ldots 0.86$. This makes it clear that also in the diffusive limit a large part of the Josephson current is carried by modes with high transmission.

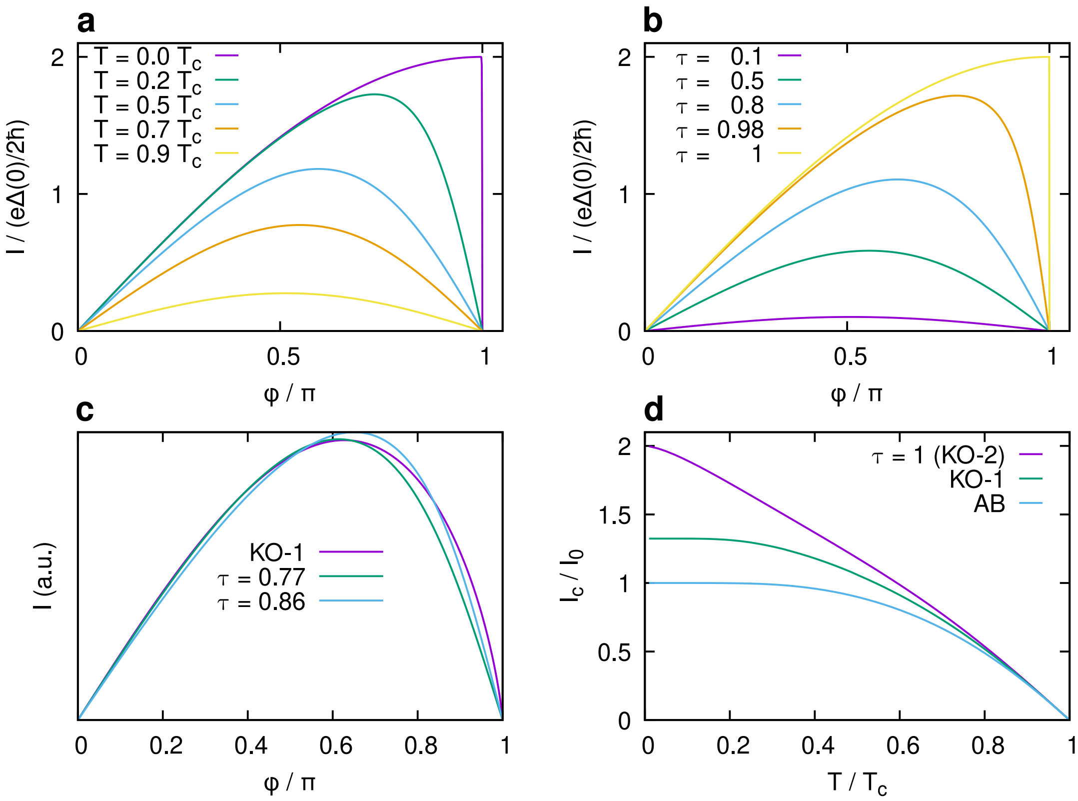

Fig. 2.3.: a, CPR of fully ballistic mode ($\tau = 1$) for different temperatures. **b,** CPR at zero temperature for different transmissions. **c,** Fits of the CPR predicted by the KO-1 model for $T = 0$ using equation Eq. (2.32). **d,** Temperature dependence of the critical current for the fully ballistic model ($\tau = 1$), the diffusive short junction model (KO-1), and the Ambegaokar-Baratov model. The current is given in units of $I_0 = \frac{\pi\Delta(0)}{2eR_N}$

2.3. SNS junctions with spin-orbit interaction

Broken structure inversion symmetry in a confined two-dimensional electron gas leads to spin-orbit coupling (SOC) of the Rashba type, a relativistic effect which can be described by the Hamiltonian

$$H_{SO} = \alpha(\vec{\sigma} \times \vec{k}) \cdot \hat{z} = \alpha(\sigma_x k_y - \sigma_y k_x), \tag{2.34}$$

where the Rashba coefficient α measures the strength of SOC. A detailed introduction to the physics of the Rashba effect can be found in [23]. The SOC results in a spin-split Fermi surface, as shown in Fig. 2.4**a**. An in-plane field breaks time-reversal symmetry and results in an exchange coupling, which is described by the Zeeman Hamiltonian

$$H_Z = \frac{1}{2} g^* \mu_B \vec{B_{\text{ip}}} \cdot \vec{\sigma}. \tag{2.35}$$

This term results in a shift of energy levels by the Zeeman energy $E_Z = 1/2 g^* \mu_B |\vec{B_{\text{ip}}}|$. In a system with Rashba SOC the Zeeman field results in a

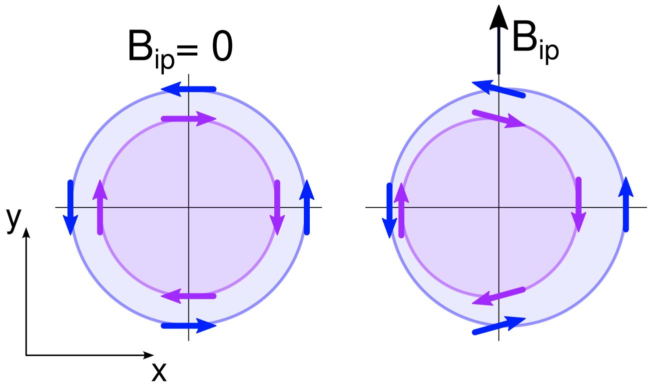

Fig. 2.4.: Left: Fermi-surface of two-dimensional electron system with Rashba spin-orbit coupling. The Fermi-surface consists of two non-degenerate sheets with helical locking of the spin, as indicated by the arrows. **Right:** In the presence of a Zeeman field in the y-direction, the blue Rashba sheet shifts in positive k_x-direction, while the purple sheet shifts in negative k_x direction.

distortion of the Fermi surface, as sketched in Fig. 2.4**b**, where both sheets are shifted perpendicular to the applied field by $\Delta k = E_Z/(\hbar v_F)$.

In the presence of either space-inversion symmetry or time-reversal symmetry, the CPR of a Josephson junction is always antisymmetric $I(\varphi) = -I(-\varphi)$. When both symmetries are broken simultaneously, i.e., by applying an in-plane Zeeman field to a SNS junction with Rashba-type SOC, the CPR can be shifted by an anomalous phase shift: $I(\varphi) = I_c \sin(\varphi - \varphi_0)$. This effect was first proposed by A. Buzdin, who studied clean-limit SNS junctions with Rashba-type spin-orbit coupling and Zeeman fields [24]. The model of Buzdin uses the quasiclassical Eilenberger equations, which describe clean (ballistic) superconductors. The derivation is performed under the assumptions that $\alpha k_F \ll E_F$ and $T \sim T_c$. The resulting CPR is

$$j(\varphi) = j_0 \sin\left(\varphi + 4\frac{\alpha E_Z L}{\hbar^2 v_F^2}\right) \frac{\cos(\frac{4|E_Z|L}{\hbar v_F} + \frac{\pi}{4})}{\sqrt{\frac{4|E_Z|L}{\hbar v_F}}}. \tag{2.36}$$

The anomalous phase shift is therefore given by

$$\varphi_0 = -4\frac{\alpha E_Z L}{\hbar^2 v_F^2}. \tag{2.37}$$

The oscillating factor, which depends on the product of junction length and exchange field, is the typical $0-\pi$-transition behavior known from SFS junctions. For $E_Z = \Delta$ and $L = \xi_0 = \hbar v_F/(\pi\Delta)$ we have $\varphi_0 = -\frac{2}{\pi}\frac{\alpha k_F}{E_F}$ from which it is clear that in this model the anomalous phase shift is small for materials where the spin-orbit splitting energy αk_F is much smaller than the Fermi energy.

More recently also the case of diffusive junctions has been studied extensively by S. Bergeret and coworkers [25, 26, 27]. Their model of diffusive SNS weak links uses a version of the Usadel equation which incorporates arbitrary linear-in-momentum SOC and Zeeman fields. The obtained differential equations for the singlet and triplet condensates are solved by imposing boundary conditions at the interface between superconductor and normal conductor. In the short junction limit and transparent interfaces between S and N regions, the φ_0-shift is given by

$$\varphi_0 = \frac{2E_Z m^{*2}\alpha^3 L^3}{\hbar^6 v_F^2} \tag{2.38}$$

This differs drastically from the ballistic case studied by Buzdin (Eq. (2.37)). The result is derived under the assumption that the order parameter in the superconducting leads is not affected by the inverse proximity effect of the normal conductor. This is not fulfilled for many types of SNS junctions [16] (including the ones with proximitized semiconductor quantum wells studied in this thesis). Therefore it is difficult to make quantitative predictions of φ_0 with Eq. (2.38). In principle one could include the suppression of the order parameter in the leads by defining an effective junction length which exceeds the geometric length of the weak link, but at the moment it is far from clear if this would enable quantitative predictions of the anomalous phase shift for realistic systems.

Neither the ballistic model of A. Buzdin nor the diffusive model of S. Bergeret at al. cover the case of short ballistic planar junctions, which is the relevant case for the modeling of our experiments. The most general technique for modeling SNS junctions with spin-orbit interaction and Zeeman fields is the Bogoliubov-de Gennes (BdG) formalism. The BdG method was used by our colleagues A. Costa, D. Kochan, and J. Fabian to perform extensive modeling of magnetochiral effects in SNS junctions [28]. In the following the technique and the most important results are presented.

The real-space BdG Hamiltonian is given by [29]

$$H_{BdG}(r) = \begin{pmatrix} H_0(r) & \Delta(r) \\ \Delta^\dagger(r) & -\sigma_y H_0^*(r)\sigma_y \end{pmatrix} \tag{2.39}$$

which is a complex 4×4 matrix. The normal state Hamiltonian $H_0(r)$ encodes the normal-state properties of the 2DEG, including the Rashba SOC and the exchange interaction due to the in-plane magnetic field:

$$H_0(r) = \frac{-\hbar^2(\partial_x^2 + \partial_y^2)}{2m^*} + U_{\mathrm{imp}}(x,y) - \mu - i\alpha(r)(\partial_y\sigma_x - \partial_x\sigma_y) + \frac{1}{2}g^*(r)\mu_0\vec{B}\cdot\vec{\sigma} \tag{2.40}$$

The magnetic field is assumed to be in the plane of the 2DEG, so that $B_z = 0$ and no effects due to Fraunhofer interference need to be considered. The in-plane g-factor for an InAs quantum well with thickness $h = 10\,\mathrm{nm}$ is $g^* \sim 10$ [30]. The Rashba parameter α in the near-surface quantum well was measured in multiple works using weak antilocalization analysis [31, 32]. These works found values of the order $\alpha \sim 10\,\mathrm{meVnm}$ and a strong dependence of α on the applied gate voltage which tunes the carrier density. It was found that α

increases with increasing carrier density. The values of α and g^* can in principle be different in the junction region and the electrodes where the 2DEG is covered by the superconductor. The model studied in [28] uses a simplified geometry which captures all the necessary ingredients for the qualitative modeling of both the anomalous phase shift and the Josephson diode effect. The geometry

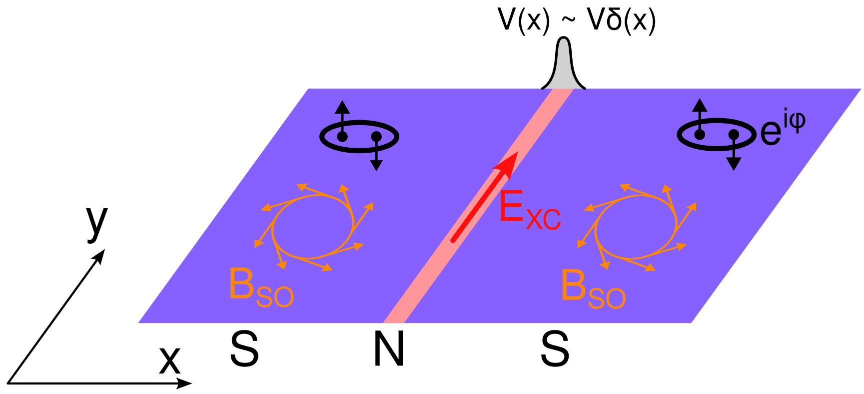

Fig. 2.5.: Geometry of the SNS model. The electrodes (blue) feature singlet pairing and Rashba SOC (spin-orbit field sketched in orange). The one-dimensional weak link (pink) features the Zeeman field and a delta-like potential barrier (adapted from [28]).

of the model is shown in Fig. 2.5. The junction is described by an infinitely thin region between the superconducting electrodes. The Zeeman field is described by the term $H_Z = E_{XC} d\sigma_y \delta(x)$, so that the product $E_{XC}d$ tunes the strength of the Zeeman field in the junction. The junction also includes a delta-potential $U_{\mathrm{imp}}(x, y) = V d\sigma_0 \delta(x)$ which is used to tune the transparency. Apart from the delta-potential the system is fully ballistic without any disorder. The SOC of the Rashba type is constant throughout the geometry. The structure extends infinitely into the x- and y-direction. In the following we use the dimensionless parameters $\lambda_Z = 2m^* E_{XC} d/(\hbar^2 k_F)$ which quantifies the exchange field and $\lambda_{SOC} = \alpha k_F/\mu = 2m^*\alpha/(\hbar^2 k_F)$ which measures the strength of the Rashba SOC. The potential barrier is quantified by $Z = 2m^* V d/(\hbar^2 k_F)$, which is related the effective transparency of the junction by $\tau = 1/(1 + (Z/2)^2)$.

The solutions of the eigenvalue problem $H_{BdG}\psi = E\psi$ for sup-gap energies $|E| < \Delta$ can be found analytically for the described model Hamiltonian. From the obtained bound state solutions one finds the Josephson current as a function of the phase bias by evaluating the current-density operator and numerically integrating over the transverse momentum k_y. The energy-phase relation is found by integrating $I_J(\varphi) = \frac{d}{d\varphi} E(\varphi)$.

Resulting curves $E(\varphi)$ and $I(\varphi)$ for $\lambda_{SOC} = 0.661$ are shown in Fig. 2.6**a**. The anomalous phase shift $\varphi_0(\lambda_Z)$ corresponds to the minima of the $E(\varphi)$ curves. Initially, the shift ($\varphi_0 < 0$ for the used parameters) slowly increases in magnitude until $\lambda_Z = 1.75$. At higher λ_Z the $E(\varphi)$ curves develop a second local minimum, which becomes the global minimum for $\lambda_Z \geq 2.0$. This means that the φ_0-shift undergoes a discrete jump between $\lambda_Z = 1.75$ and $\lambda_Z = 2.0$. This behavior is called 0-π-like transition in analogy to the well-known 0-π transition in SFS Josephson junctions. The 0-π-like transition was first proposed in the work of Yokoyama et al. [33, 34], who numerically studied few-mode nanowire Josephson junctions in the presence of Rashba SOC and Zeeman field. In the two-dimensional planar junctions studied by Costa. et al. the magnetochiral effects are enhanced due to channels with large transverse momentum k_y. On the other hand, the channels with low k_y (i.e. the wave vector points in the x-direction) do not have any contribution to φ_0.

Another magnetochiral effect in superconductivity which is caused by the interplay of spin-orbit coupling and Zeeman fields is the superconducting diode effect. This effect was first observed by the group of Prof. T. Ono when studying MBE-grown $[Nb/V/Ta]_n$ superlattices [10]. The three-layer structure of the superlattices breaks structure-inversion symmetry, leading to strong Rashba-type SOC. When applying an in-plane magnetic field perpendicular to the direction of an applied bias current the authors observed different critical currents for positive and negative polarity of the bias. Before this discovery it was well known that non-reciprocal critical currents can be engineered in systems which break spatial symmetries. The most simple example is the asymmetric SQUID, which will be studied in more detail in the next chapter. The groundbreaking difference in the effect observed by Ando et al. is that the device is symmetric and the rectification is created by acting on the electron spin, i.e., it is an intrinsic and microscopic property of the superconducting material. This unexpected discovery led to a surge of interest in non-reciprocal superconductivity, with several hundred papers on the topic published since then.

Coming back to our theoretical model of the Josephson effect in SNS junctions with spin-orbit coupling, we also observe a non-reciprocal effect in the CPRs shown in Fig. 2.6**b**: The critical currents for positive and negative polarity are no longer equal. This feature of ballistic SNS junctions with SOC and Zeeman field is called the "Josephson diode effect". The diode effect is quantified by the diode efficiency

$$\eta = \frac{\Delta I_c}{I_{c,mean}} = \frac{2(I_{c,+} + I_{c,-})}{I_{c,+} + |I_{c,-}|}, \tag{2.41}$$

where $I_{c,+} > 0$ and $I_{c,-} < 0$ are the positive and negative critical currents, respectively. The positive and negative critical currents as a function of λ_Z are shown in Fig. 2.7**a** and the resulting diode efficiency is shown in Fig. 2.7**b**. Like the anomalous phase shift, the diode efficiency is an anti-symmetric function of the Zeeman field parameter λ_Z, i.e., $\eta(\lambda_Z) = -\eta(-\lambda_Z)$. After reaching a maximum at $\lambda_Z \sim 1.75$, the diode efficiency decreases rapidly and reverses its sign. After the sign-reversal the absolute value of η quickly decreases to zero. Interestingly, the sharp maximum of η followed by the rapid decrease was found in nearly all experimental systems which showed the Josephson diode effect. The sign reversal in the diode efficiency was also found in some systems, but this particular feature seems to be very sensitive to the details of the system [36]. Apart from the anomalous phase shift and the Josephson diode effect another

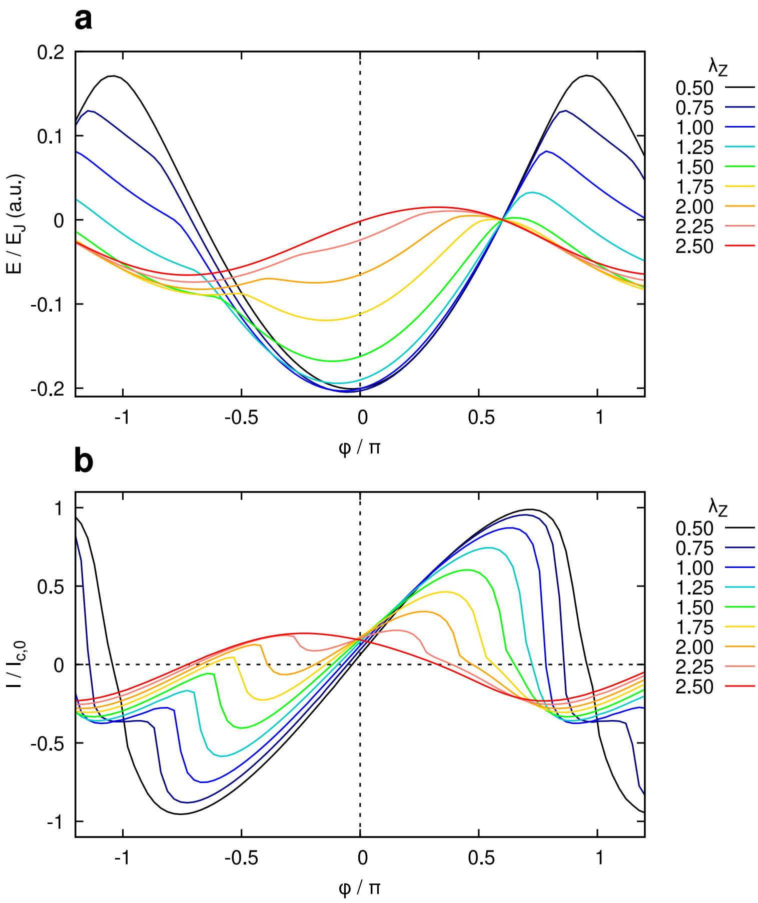

Fig. 2.6.: a, Energy-phase relations calculated for $\lambda_{SOC} = 0.661$ and different parameters of the Zeeman exchange coupling λ_Z. See text for the parameter definitions. **b,** Current-phase relations for the same parameters as in panel **a**. Data from [35].

physical observable which can be used to study the magnetochiral anisotropy of the system is the Josephson inductance. This powerful technique was already described in the thesis of Christian Baumgartner [37].

One alternative to the model used in our work are direct numerical techniques which discretize the BdG Hamiltonian and compute the low energy part of the spectrum, see e.g. [12, 36] for recent examples. This has the advantage that arbitrary geometries of the leads and the junction can be studied. Moreover, it allows to study the effect of a finite g-factor in the electrodes. A big advantage of the model of A. Costa is computational efficiency. This is because no discretization is required to find the energy and shape of the Andreev bound state solutions for each transverse wave vector k_y. The CPR is then found by integration over transverse momenta on the Fermi surface. This enables the computation of the energy-phase and CPR for a wide range of paremeters, namely Zeeman fields, Rashba parameters, barrier potentials, and temperatures.

A striking difference between the anomalous phase shift and the diode efficiency is their temperature dependence. Fig. 2.8 shows the φ_0-shift and the diode efficiency as a function of temperature. While the φ_0-shift is nearly constant up to

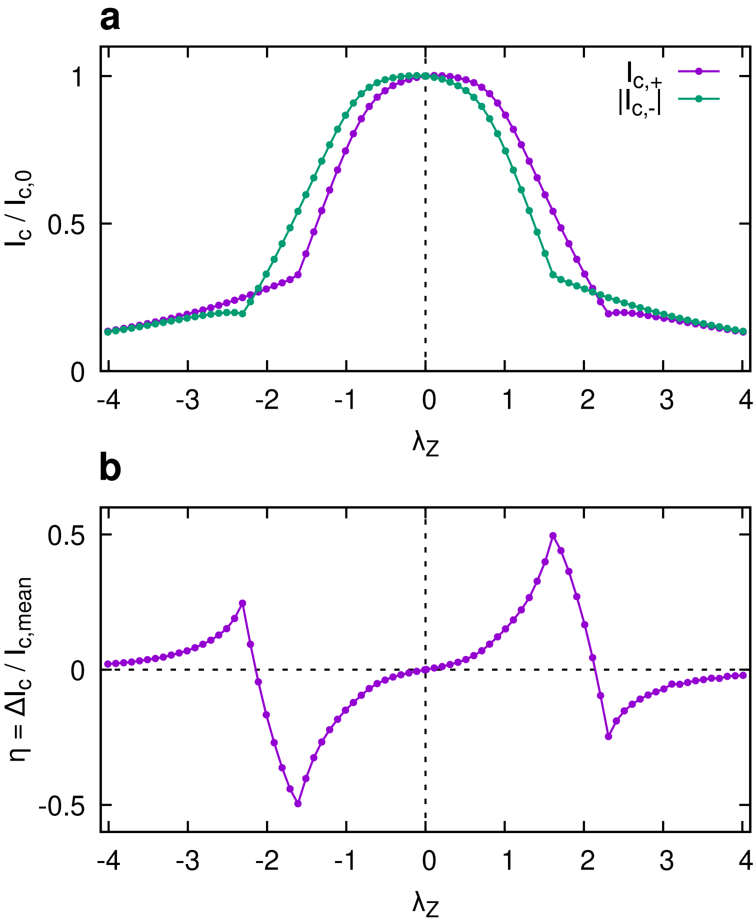

Fig. 2.7.: a, Positive and negative critical current as a function of the Zeeman exchange parameter λ_Z. The strength of SOC is $\lambda_{SOC} = 0.661$. The critical current is normalized to the critical current at zero field. **b,** Diode efficiency $\eta = 2\frac{I_{c,+}-|I_{c,-}|}{I_{c,+}+|I_{c,-}|}$. Data from [35].

the critical temperature, the diode efficiency is rapidly suppressed by temperatures exceeding $0.1T_c$. Unlike the φ_0-shift, the diode effect requires higher harmonics in the CPR. As we have seen before in the Furusaki-Beenakker model, the higher harmonics of the CPR in a ballistic junction are rapidly suppressed by increasing temperature. This was also clearly observed in experiment, as will be shown in Chapter 3.

2.3.1. Recent developments in the theory of the anomalous phase shift and the Josephson diode effect

One requirement for the emergence of the Josephson diode effect are high harmonics in the CPR. As shown above, also diffusive junctions feature non-sinusoidal CPR at sufficiently low temperatures. A recent preprint from S. Ilić et al. studies the Josephson diode effect in diffusive junctions with SOC and Zeeman field using a generalized Usadel diffusion equation, which incorporates

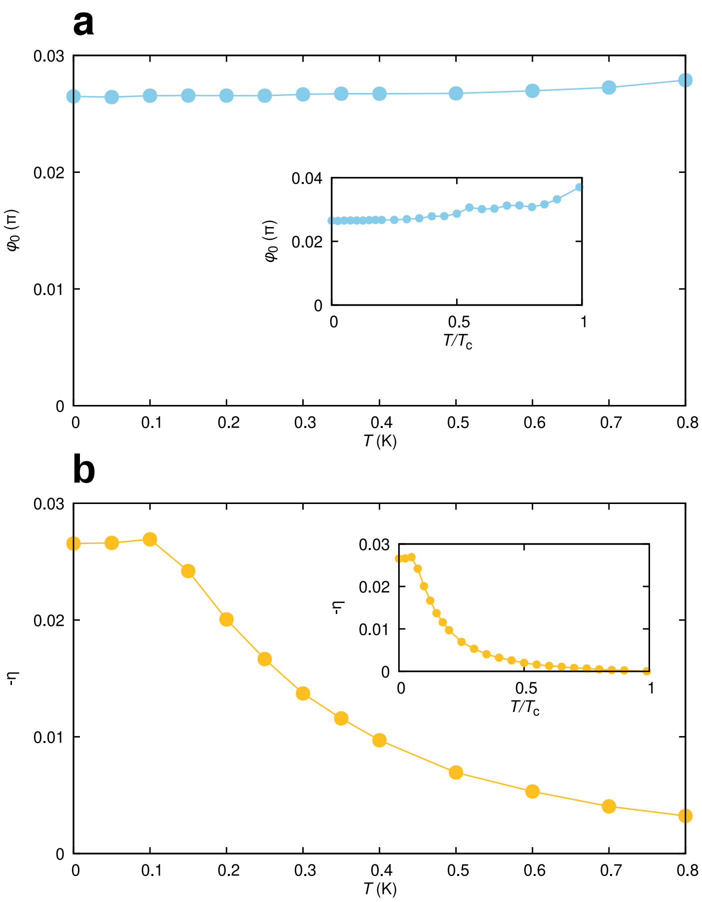

Fig. 2.8.: Temperature dependence of the anomalous phase shift (**a**) and the diode efficiency (**b**) obtained from the model of A. Costa. The used parameters are $\lambda_Z = -0.4$ and $\lambda_{SOI} = 0.661$. Data from [38].

the effects of linear-in-momentum SOC and exchange interaction [27]. After imposing boundary conditions at the interface between superconducting leads and the normal conducting junction region, the CPR is found by numerical solution of differential equations for the singlet and triplet components of the condensate. For this diffusive model, it is assumed that the mean free path $l = v_F\tau$ is much smaller than the BCS coherence length $\xi_0 = \hbar v_F/(\pi\Delta_0)$, and the following hierarchy of energy scales needs to be fulfilled

$$\mu \gg \hbar/\tau \gg \alpha k_F,\, E_Z. \tag{2.42}$$

The condition $\hbar/\tau \gg \alpha k_F$ is equivalent to $l \ll \frac{\hbar^2}{m^*\alpha}$. For a value of $\alpha = 10\,\mathrm{meVnm}$ and $m^* = 0.04m_e$ the resulting condition for the mean free path is $l \ll 200\,\mathrm{nm}$. As we will see in the following chapter, we are clearly not in this limit with our near-surface InAs quantum wells, where typically $l \gtrsim 200\,\mathrm{nm}$. Therefore it is not clear whether disorder induced spin relaxation and singlet-triplet conversion processes play a role in the Al/InAs devices.

Another recent preprint studies the Josephson diode effect for superconducting leads with mixed singlet/triplet pairing [39]. The model studies a single ballistic channel with Rashba-like SOC coupling and Zeeman field in the normal region. For the case with mixed singlet-triplet pairing the BdG Hamiltonian in momentum space is given by

$$H_{BdG}(k) = \begin{pmatrix} H_0(k) & \Delta(k) \\ \Delta^\dagger(k) & -H_0^*(-k) \end{pmatrix}, \tag{2.43}$$

where the pairing potential is composed of singlet and triplet components

$$\Delta(k) = \Delta_s(k) + \Delta_t(k) = |\Delta_s|(i\sigma_y)\psi(k) + |\Delta_t| i(\vec{d}(k)\vec{\sigma})\sigma_y. \tag{2.44}$$

The singlet pairing is described by the even function $\psi(k) = \psi(-k)$, while the triplet pairing is described by the complex vector $\vec{d}$ which is an odd function of momentum: $\vec{d}(k) = -\vec{d}(-k)$. For $\vec{d} \sim (0, 0, 1)$ one obtains opposite-spin triplet pairing of type $|\uparrow\downarrow\rangle + |\downarrow\uparrow\rangle$, while for $\vec{d} \sim (1, 0, 0)$ one obtains equal-spin pairing of type $|\downarrow\downarrow\rangle - |\uparrow\uparrow\rangle$. When time reversal symmetry is not broken, $\vec{d}(k)$ is real-valued and the total spin of the pairing state is zero for each value of k. This is the case studied in [39]. The CPR is studied as a function of the angles between $\vec{d}(k)$, the Zeeman field, and the direction of the spin-orbit field $\vec{B}_{so}$. A large diode efficiency is found when the triplet component $|\Delta_t|$ exceeds the singlet component $|\Delta_s|$. When increasing the ratio $|\Delta_t|/|\Delta_s|$ above a value of ~ 10, a sign-reversal of the diode effect is found. Unlike the models discussed above, this model does not need SOC as an ingredient for the diode effect when the direction of the triplet pairing vector $\vec{d}$ and the Zeeman field in the channel are non-collinear. More work will be required to extend this one-dimensional model to 2D planar junctions. In the 2D case the CPR results from many different channels with different transverse momenta. In the presence of spin-orbit interaction there is a “protected” direction of the triplet pairing vector $\vec{d}(\vec{k})$ which is parallel to the spin-orbit field. For Rashba SOC this means that $\vec{d}(\vec{k})$ must be perpendicular to the momentum vector $\vec{k}$ [40].

3. Asymmetric SQUID measurements: Anomalous phase shift and Josephson diode effect

The measurement of the Josephson diode effect only requires measurements of the critical current in both polarities, which can be performed using a single current biased Josephson junction. In comparison, the measurement of the anomalous Josephson effect is more difficult, as it requires phase biasing of a junction. So far, all published measurements of a φ_0-shift have used a system of two Josephson junctions connected in a superconducting loop, known as a Superconducting Quantum Interference Device (SQUID). In the SQUID the phase over the two junctions in the loop is linked to the magnetic flux through the loop due the fluxoid quantization in the loop.

In the theory of the Josephson diode effect, which was published together with our first demonstration of the effect, it was predicted that the anomalous phase shift and the Josephson diode effect are intimately linked and in the predicted current-phase relations both effects always appear simultaneously. To test this prediction we now present an experiment where both effects can be measured on a single junction simultaneously, e.g. in one cooldown of the junction device. We perform precise measurements of the anomalous phase shift as a function of top-gate voltage, direction of the in-plane magnetic field, and temperature. This reveals a strong link between both effects. However, the temperature dependence of both effects shows that the anomalous phase shift is only a necessary and not a sufficient requirement for the Josephson diode effect. The results of this chapter are published in the article [38].

3.1. SQUID basics

This section introduces the basic behavior of the "textbook"-SQUID device. We start by assuming that the junctions have sinusoidal CPRs and neglect inductive effects in the SQUID circuit. Later in this chapter we will extend this basic model by allowing arbitrary CPRs. We will also have to include inductive screening effects caused by the large kinetic inductance of our thin superconducting films. The screening effects will turn out essential for the description of the measured interference patterns.

The basic SQUID device is shown in Fig. 3.1. The two Josephson junctions on the left and the right have critical currents $I_{c,1}$ and $I_{c,2}$, respectively. The total current of the device as a function of the gauge-invariant phase differences on the junctions is given by

$$I = I_1 + I_2 = I_{c,1}\sin(\gamma_1) + I_{c,2}\sin(\gamma_2). \tag{3.1}$$

The difference of the two phases is constraint by the fluxoid quantization relation

$$\gamma_2 - \gamma_1 = 2\pi(\Phi/\Phi_0 + N), \tag{3.2}$$

where Φ is the externally applied magnetic flux through the loop and $\Phi_0 = h/(2e) \sim 2 \times 10^{-15}\,\mathrm{Tm}^2$ is the superconducting flux quantum. The critical current of the SQUID can now be found using basic trigonometric identities:

$$I = I_{c,1}\sin(\gamma_1) + I_{c,2}\sin(\gamma_1 + 2\pi\Phi/\Phi_0) = \tag{3.3}$$

$$\sqrt{I_{c,1}^2 + I_{c,2}^2 + 2I_{c,1}I_{c,2}\cos(2\pi\Phi/\Phi_0)}\,\sin(\gamma_1 + \delta(I_{c,1}, I_{c,2}, \Phi)), \tag{3.4}$$

where the phase offset δ does not depend on γ_1. The critical current of the SQUID is therefore given by

$$I_c(\Phi) = \sqrt{I_{c,1}^2 + I_{c,2}^2 + 2I_{c,1}I_{c,2}\cos(2\pi\Phi/\Phi_0)}. \tag{3.5}$$

If the critical currents of the two junctions are different, the critical current of the SQUID oscillates between a maximum value of $I_{c,1} + I_{c,2}$ and a minimum value of $I_{c,1} - I_{c,2}$, as shown in Fig. 3.1. We also have to deal with CPRs which are not sinusoidal. In this case the critical current needs to be obtained numerically by finding the maximum and minimum values of $I_1(\gamma_1) + I_2(\gamma_2 = \gamma_1 + 2\pi\Phi/\Phi_0)$.

SQUIDs with large asymmetry of the critical currents can be used to measure current phase relations. Setting $I_{c,1} \gg I_{c,2}$ in Eq. (3.3) and ignoring the second-order term $(I_{c,2}/I_{c,1})^2$ yields

$$I_c(\Phi) \sim I_{c,1} + I_{c,2}\sin(\Phi/\Phi_0 + \pi/2), \tag{3.6}$$

showing that the modulation of the critical current is given by the CPR of the small junction.

3.2. Asymmetric SQUID device

The asymmetric SQUID device is fabricated from a molecular beam epitaxy grown heterostructure featuring an InGaAs/InAs/InGaAs quantum well. The

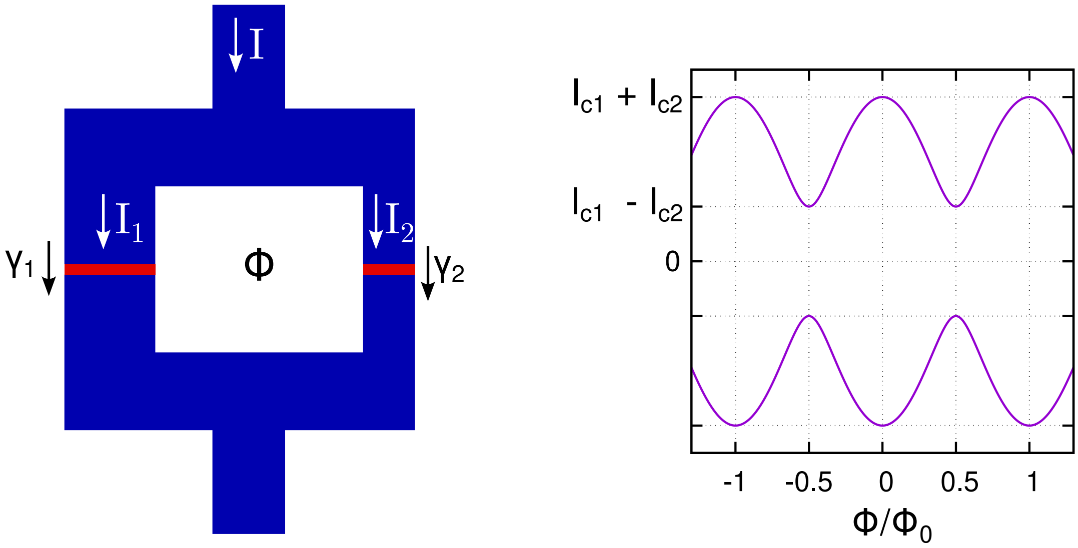

Fig. 3.1.: Left: Basic asymmetric SQUID device consisting of two Josephson junctions in a superconducting loop. Right: Critical current of the asymmetric SQUID as a function of the magnetic flux Φ through the loop. The flux through the loop is measured in units of the superconducting flux quantum $\Phi_0 = \frac{h}{2e}$.

semiconductor stack is capped with a 5 nm thick epitaxial layer of aluminum. The characterization of the two-dimensional electron gas and the superconducting aluminum film are described in Appendix A. The peak mobility of the two-dimensional electron gas is $\mu > 60\,000\,\mathrm{Vs/cm^2}$ at a carrier density $n \sim 5 \times 10^{11}\,1/\mathrm{cm}^2$. A schematic of the device geometry is shown in Fig. 3.2**a**. A large reference junction JJ1 and a small probe junction JJ2 are defined by selective removal of the superconductor. The probe junction JJ2 is covered by a top gate which is used to tune the carrier density of the electron gas in the semiconductor below the junction. A false color scanning electron microscope image of the device is shown in Fig. 3.2**b**. The turquoise areas correspond to the pristine superconductor-semiconductor layer stack. In the yellow areas the aluminum film is selectively removed, while the semiconductor layers are still fully present. In the remaining gray areas the semiconductor is deeply etched, so that this part of the device is electrically insulating. The diameter of the loop is $d_{\mathrm{loop}} \sim 40\,\mu\mathrm{m}$. The reference junction (JJ1) is approximately $28\,\mu\mathrm{m}$ wide and 120 nm long. The probe junction (JJ2) is $2.7\,\mu\mathrm{m}$ wide and 100 nm long. Both junctions are capped by aluminum oxide grown by atomic layer deposition, which serves as gate dielectric. Finally, JJ2 is covered by a Ti/Au gate electrode. The image shown in Fig. 3.2**b** was taken before the growth of the gate dielectric.

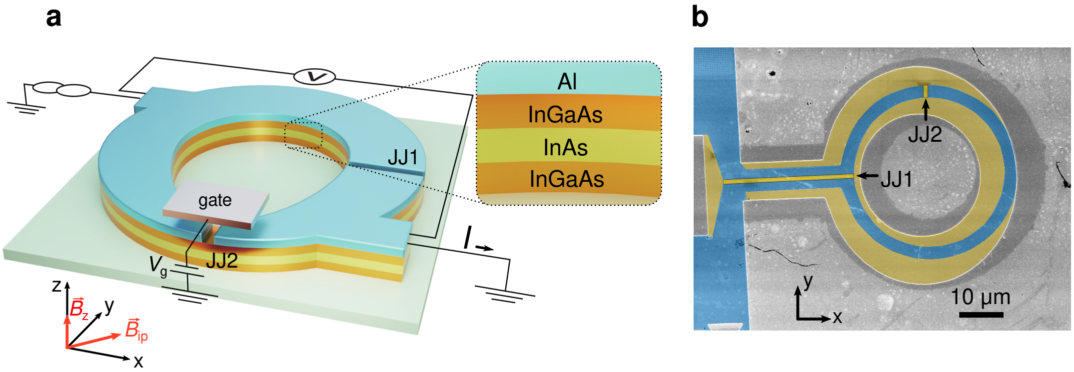

Fig. 3.2.: **a**, Schematic of the device geometry of the asymmetric SQUID device. The electron density in the small junction JJ2 can be tuned with a top gate. **b**, False-color scanning electron microscopy image of the device before deposition of the aluminum oxide dielectric. The pristine Al/InAs stack is shown in turquoise, the areas of etched aluminum with the pristine semiconductor stack are shown in yellow. In the grey regions the semiconductor is deep etched. Fabrication and SEM imaging of the device was performed by T. Ascherl.

3.3. Gate dependence of the anomalous phase shift

Fig. 3.3 shows a color map of the differential resistance versus out-of-plane field B_z and DC current I, measured with an applied field $B_y = -100$ mT at $T = 40$ mK. The black regions correspond to the superconducting regime below the critical current of the SQUID device while the purple regions correspond to the dissipative state above the critical current. The fast oscillations of the critical current have a period of 1.8 µT, corresponding to a flux quantum $\Phi_0 = h/2e$ applied to the loop. These fast oscillations are superimposed to the central part of the Fraunhofer pattern of the reference junction. The Fraunhofer pattern of the small junction is not relevant as it would appear only on field scales of the order of 1 mT. The plot displays an evident asymmetry around the $B_z = 0$ and $I = 0$ axes, while it is approximately point-inversion-symmetric around the origin, namely $I_c(B_z) \approx -I_c(-B_z)$. The fast oscillations of the critical current have a strongly skewed sawtooth-like shape. Moreover, the amplitude of the oscillations differs drastically in different regions of the interference pattern. These features can be explained by screening effects in the SQUID. This screening effect is not a self-field effect due to magnetic flux generated by the currents flowing in the SQUID device. As we will see, the main cause for the screening effect is the large kinetic inductance of the ultrathin aluminum film. The value of the kinetic inductance can be estimated from the normal state resistance and the critical temperature. For low frequencies $\hbar\omega \ll 2\Delta$ the imaginary part of the complex conductivity of the film is given by [13, Sect. 3.10.5]

$$\sigma_2 = \frac{\sigma_n \pi \Delta(T)}{\hbar\omega} \tanh\left(\frac{\Delta(T)}{k_B T}\right), \tag{3.7}$$

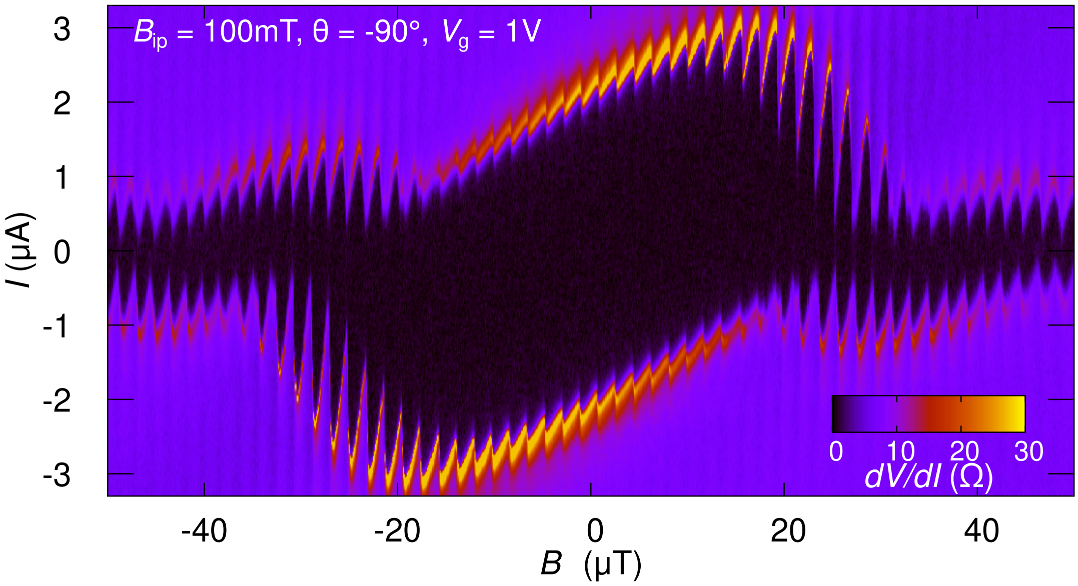

Fig. 3.3.: SQUID interference pattern. Differential resistance $dV/dI(I = I_{\text{bias}})$ is measured using the SR830 digital lock-in amplifier together with the Stanford Research SR552 bipolar preamplifier. The in-plane field is set to $B_{\text{ip}} = 100\,\text{mT}$.

where σ_n is the conductivity in the normal state. The sheet resistivity is then given by $R_\square = 1/\sigma_\square = d/\sigma_n$, where d is the film thickness. The sheet inductance of the Al film is

$$L_\square = \frac{1}{\omega\sigma_{2,\square}} = \frac{\hbar R_\square}{\pi\Delta(T)\tanh(\frac{\Delta(T)}{k_B T})}. \tag{3.8}$$

This value can now be estimated from the known material parameters. The sheet resistance of the aluminum film is $R_\square = 36\,\Omega$ as shown in Appendix A. The gap energy Δ can be estimated from the critical temperature using the weak coupling BCS result $\Delta(T = 0) = 1.764\,k_B T_c$. The measured value of the critical temperature is $T_c = 2.07\,\text{K}$, and from this we obtain $\Delta(T = 0) \sim 300\,\mu\text{eV}$. The resulting value of the kinetic inductance of the aluminum film is $L_\square(T \ll T_c) \sim 25\,\text{pH}$. The total expected kinetic inductance of the loop is $L_{\text{loop}} = N_{\text{loop}} L_\square \sim 1\,\text{nH}$. For a current in the loop of $I_{\text{loop}} = 1\,\mu\text{A}$, the screening flux is $L_{\text{loop}} I_{\text{loop}} \sim \Phi_0/2$, showing that the screening flux generated by the circulating current is of the same order as the superconducting flux quantum. We now present an extended circuit model of our device, which includes the kinetic inductance of the loop and the the electrodes of the reference junction. The minimum model which captures all relevant effects is show in Fig. 3.4**a**. The reference junction JJ1 is modeled as a network of N JJs in parallel, each with critical current $I_{c,1}/N$. Setting $N = 20$ is sufficient to model the central lobe of the Fraunhofer interference pattern of JJ1. The effective area of JJ1 is A_{ref}, while the area of the large loop is A_{loop}. The positive and negative critical currents for a given out-of-plane field B_z can be calculated as a function of the phase difference γ_{JJ2} over JJ2. Fixing a value of γ_{JJ2}, all the other phase differences and currents in the circuit can be found by repeatedly using the fluxoid quantization relation for all loops in the system. For example, the

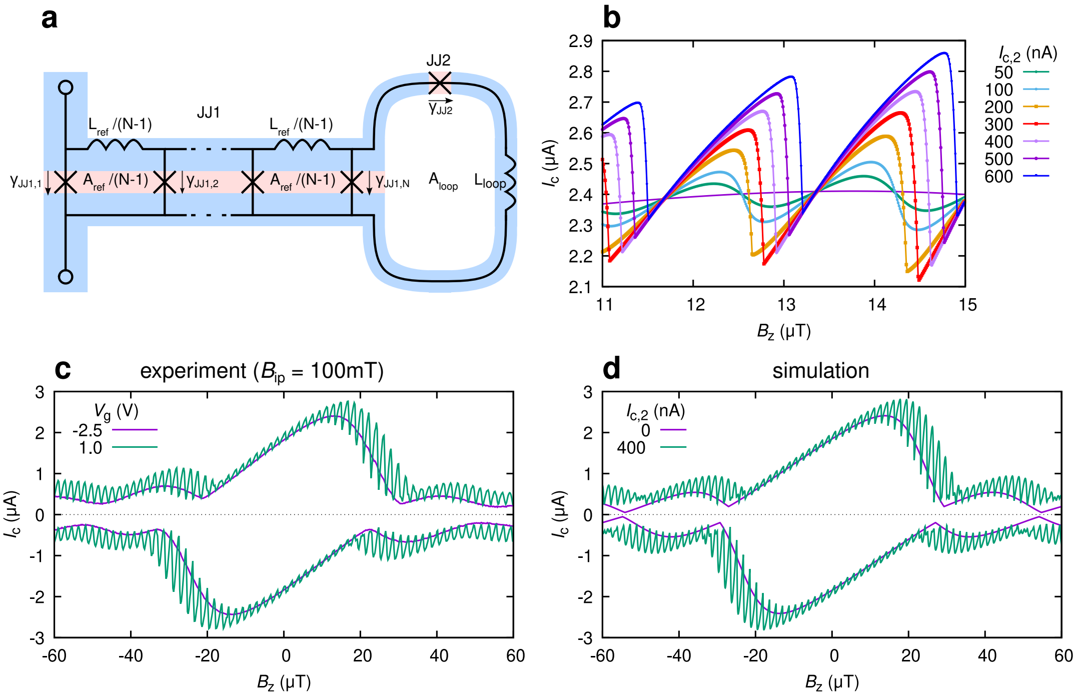

Fig. 3.4.: **a**, Minimal circuit model of the SQUID device. **b,d**, Simulated critical currents of the SQUID with parameters as described in the text. **c**, experimental values of positive and negative critical currents for $B_{\rm ip} = 100$ mT and $\theta = -90$ °.

phase difference $\gamma_{\rm JJ1,N}$ over the rightmost junction in JJ1 is given by

$$\gamma_{{\rm JJ1},N} = \gamma_{\rm JJ2} - 2\pi(B_z A_{\rm loop} - L_{\rm loop} I_{c,2} \sin(\gamma_{\rm JJ2}))/\Phi_0. \tag{3.9}$$

The phase differences $\gamma_{{\rm JJ1},i}$ are then found as

$$\gamma_{{\rm JJ1},i} = \gamma_{{\rm JJ1},i+1} - 2\pi(B_z A_{\rm ref}/(N-1) - L_{\rm ref}/(N-1) I_i)/\Phi_0, \tag{3.10}$$

where $I_i = I_{i+1} + I_{c,1}/N \sin(\gamma_{{\rm JJ1},i+1})$ is the current flowing through the inductor between junctions i and $i+1$. Finally, the positive and negative critical currents of the circuit are found as the extremal values of $I_0(\gamma_{\rm JJ2})$. In Fig. 3.4**b,d** we demonstrate this model by simulating the SQUID critical current as a function of the out-of-plane field B_z. The parameters correspond to an applied in-plane-field of $|B_y| = 100$ mT. A good match to the experimental data shown in Fig. 3.4**c** can be found with the following parameters: $A_{\rm loop} = 1150\,\mu{\rm m}^2$, $I_{c,1} = 2.48\,\mu$A, $A_{\rm ref} = 70\,\mu{\rm m}^2$, $L_{\rm ref} = 0.8\,$nH, and $L_{\rm loop} = 1.5\,$nH. From the value of $L_{\rm loop}$ we determine the sheet inductance of the aluminum film $L_\square = L_{\rm loop}/N_{\square,\rm loop} = 1.5\,{\rm nH}/46 \sim 30\,$pH, which is in good agreement with the value estimated above from the sheet resistance.

The geometric inductance of the loop is small in comparison with the kinetic inductance. The geometric inductance of the loop can be approximated using the known result for a circular ring made from a wire. The inductance is

$$L_{\rm loop,geo} = \mu_0 R(\ln(8R/a) - 7/4) \tag{3.11}$$

for a loop radius R and a wire radius $a \ll R$ [41, p. 234]. Using $R = d/2 = 20\,\mu\text{m}$ and $a = w/2 \sim 1\,\mu\text{m}$ results in $L_{\text{loop,geo}} \sim 80\,\text{pH}$. We conclude that the geometric contribution to the screening effects can be neglected.

Given the large distortion of the critical current oscillations it might seem difficult to extract information about the anomalous phase shift. As we show now, this is actually not the case and the extraction of the anomalous phase shift is not affected by the screening effects. Fig. 3.4**b** shows the simulated SQUID critical currents for different values of the critical current of the small probe junction. The skewness of the oscillations increases with increasing critical current. For the purple reference line the critical current of JJ2 is set to zero. The intersection point with the reference line is the same for all curves. At this intersection point the current in the loop and JJ2 is zero and therefore at this particular point of the SQUID interference pattern the inductance of the loop has no effect. We only consider the intersection point where $I_c(B_z)$ has positive slope. The intersection points with negative slope correspond to the maxima of the energy-phase relation and are not relevant for the study of the anomalous phase shift, which is defined as the phase at the minimum of the energy-phase relation.

Panels **a-c** of Fig. 3.5 show high-resolution measurements of the SQUID critical current near the peak of the central lobe of the interference pattern. At a gate voltage of $V_g = -2.5\,\text{V}$ (black line) no oscillations are visible, meaning that the junction JJ2 is completely pinched off. While it is not possible to find the absolute value of the anomalous phase shift, the excursion with gate voltage can be found with high precision. To this end we extract the parameter $\Delta\varphi_0(V_g) := 2\pi(B_0(V_g) - B_0(-2.5\,\text{V}))A_{\text{loop}}/\Phi_0$. In panels **a** and **c** the in-plane field is aligned perpendicular to the direction of current in the junctions, while in panel **b** the field is aligned in the direction of current. For the perpendicular configurations we observe sizable values of $\Delta\varphi_0$, while it is close to zero for the parallel configuration. The behavior of $\Delta\varphi_0$ as a function of gate voltage is shown in Fig. 3.5**d** for different rotation angles of the in-plane field. For the perpendicular configuration this plot shows a monotonic increase of the effect with gate voltage. The dependence of $\Delta\varphi_0(1\,\text{V})$ on the rotation angle between current and in-plane magnetic field is shown in Fig. 3.5**e** for an in-plane field with magnitude 100 mT. As φ_0 is a magnetochiral quantity caused by Rashba SOC and Zeeman field, the expected behavior is $\varphi_0 \sim (\vec{B}_{\text{ip}} \times \vec{I}) \cdot \vec{e}_z \sim \sin(\theta)$. The measurement is in very good agreement with the expected sinusoidal dependence.

With this experiment it is not possible to measure the absolute value of φ_0, as this would require knowledge of the out-of-plane field B_z with an accuracy far below $1\,\mu\text{T}$. This is not feasible in this experiment as large in-plane fields of order 100 mT need to be applied, which always have a small misalignment into the out-of-plane direction. Additionally, the tilt angle of the sample with respect to the direction of the in-plane field changes when rotating the sample with the cryogenic piezo rotator.

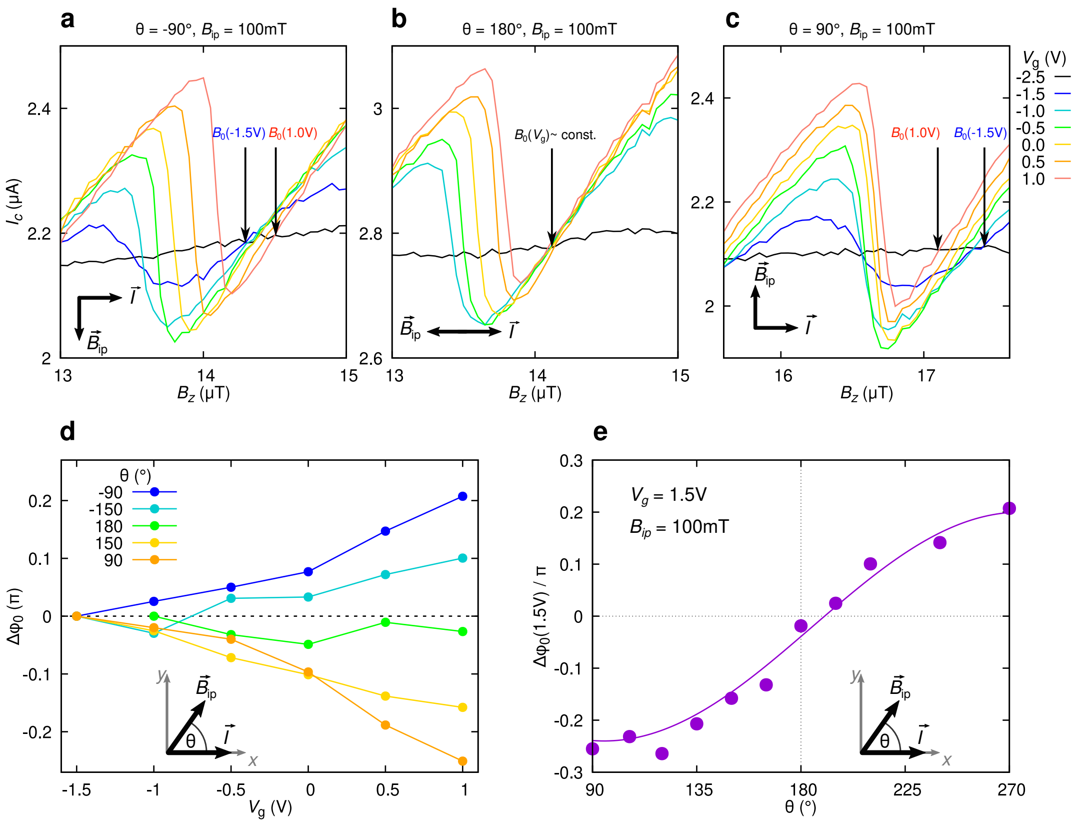

Fig. 3.5.: a-c, SQUID critical current as a function of B_z for different orientations of the in-plane field. The magnitude of the in-plane field is $B_{\mathrm{ip}} = 100\,\mathrm{mT}$ and the temperature is $T \sim 40\,\mathrm{mK}$. Different colors correspond to different values of the gate voltage. The $V_g = -2.5\,\mathrm{V}$ line is intersected by the $I_c(B_z)$ curves at the field values $B_0(V_g)$. **d**, Phase shift $\Delta\varphi_0$ as a function of gate voltage for different orientations of the in-plane field. **e,** Shift of the crossing point $\Delta\varphi_0(1\,\mathrm{V}) := 2\pi(B_0(1\,\mathrm{V}) - B_0(-2.5\,\mathrm{V}))A_{\mathrm{loop}}/\Phi_0$ as a function of the angle between B_{ip} and the current. The solid line is a sinusoidal fit. A good fit requires a small shift of the sine function in both x and y direction. The values shown in **c,d** are found by averaging over many measurements (see text).

The first measurements of the anomalous phase shift in Al/InAs based junctions were performed by the group of J. Shabani [42, 43]. These pioneering works were performed with symmetric SQUIDs using two 4 µm wide junctions, both covered by separate gate electrodes. The asymmetry of the SQUID was generated by depleting one of the two junctions. In comparison to our device, the junctions were fabricated with much narrower leads, however the exact geometry is not provided in these works. The narrow leads make the junctions more resilient to in-plane fields applied in the perpendicular direction, allowing the detection of a critical current for field magnitudes up to 850 mT. The authors claimed the observation of a 0-π-like transition together with a reentrant critical current. Unlike the theory presented in the preceding chapter, the 0-π-like transition in these works was interpreted as a signature of a topological phase transition. In our device the maximum possible in-plane magnetic field for which a critical current can be observed is much lower. One possible explanation is the different geometry of the junction electrodes. The extended electrodes in our device could lead to strong orbital pair breaking for large in-plane fields. The largest field magnitude for which a measurement of $\Delta\varphi_0$ is possible in our device is 250 mT. Fig. 3.6 shows the value of $\Delta\varphi_0(V_g = 1\,\mathrm{V})$ as a function of the field magnitude for the perpendicular configuration ($\theta = -90°$). This measurement shows a saturation of the anomalous phase shift for $|B_y| > 100\,\mathrm{mT}$. The extraction of $\Delta\varphi_0$ from the measured $I_c(B_z)$ curves is only possible for in-plane fields with a magnitude above $\sim 100\,\mathrm{mT}$. For lower in-plane fields the higher critical currents of the junctions lead to larger screening effects. Because of the large screening the $I_c(B_z)$ curves no longer intersect with the reference line obtained by pinching off the small junction. One example of this behavior can be seen in Fig. 3.8**a**, which shows $I_c(B_z)$ curves obtained at $|B_{\mathrm{ip}}| = 50\,\mathrm{mT}$. In this data only the curve with $V_g = -1.5\,\mathrm{V}$ intersects the reference line while for all higher gate voltages the critical current is always above the reference line. This effect can also be found when simulating the $I_c(B_z)$ curves using the presented circuit model. The simulated curves are above the reference line when the dimensionless screening parameter $I_{c,2}L_{\mathrm{loop}}/\Phi_0$ exceeds a value of 0.5. We conclude that the used technique of extracting $\Delta\varphi_0$ from the measured data is only possible when the magnitude of the in-plane magnetic field is above $\sim 100\,\mathrm{mT}$.

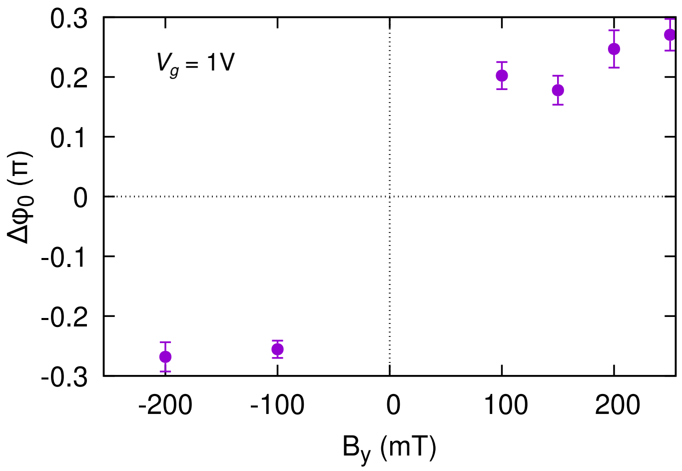

Fig. 3.6.: $\Delta\varphi_0$ as a function of in-plane field magnitude measured at $V_g = 1\,\mathrm{V}$ at a rotation angle of $\theta = -90°$. The values are obtained by averaging over 40 gate voltage cycles. The error bars correspond to the standard deviation of the individual values.

In the works of the Shabani group the parameter $\Delta\varphi_0$ was extracted by fitting the complete $I_c(B_z)$ curves to a SQUID model with ballistic current phase relations, using the critical currents, anomalous phase shifts and transparencies as fitting parameters. This way both $\Delta\varphi_0$ and the junction transparencies were extracted from the measured data [42, 43]. These experiments were performed on heterostructures with relatively thick aluminum films (10 nm instead of 5 nm used in our work) and screening effects due to kinetic inductance were not taken into account in the data analysis. A major difference of the method presented in this thesis is that we do not require to know the shape of the current phase relation. The only requirements for our technique are a large asymmetry of the critical currents ($I_{c,\mathrm{ref}} \gtrsim 10 I_{c,\mathrm{probe}}$) and that the probe junction can be pinched off completely by the top gate.

One problem encountered in our experiments is a slow drift of the out-of-plane magnetic field B_z. This occurs especially directly after the refilling of liquid helium and nitrogen into the dewar. The high accuracy of the presented data was made possible by repeated cycling of the gate voltage, i.e., the data shown in Fig. 3.5**a-c** are recorded many times (most data was obtained using 40 repetitions). The evaluated $\Delta\varphi_0(V_g)$ values shown in Fig. 3.5**d,e** are found by averaging over the individual measurements.

3.4. Gate dependence of the Josephson diode effect

The measured $I_c(B_z)$ curves can also be used to extract the efficiency of the Josephson diode effect which occurs in the small probe junction in the presence of an in-plane magnetic field. Fig. 3.7 shows simulated $I_c(B_z)$ curves for realistic parameters corresponding to an in-plane field of magnitude 50 mT. The critical current $I_{c,2}$ is extracted as the maximum difference of $I_c(B_z)$ and the reference line where $I_{c,2} = 0$: $I_{c,2} = \max(I_c(B_z) - I_{c,\mathrm{ref}}(B_z))$. It is found that this extracted critical current is reduced by a factor of three when compared to the actual critical current of JJ2 used in the circuit simulation. This is an effect of screening which reduces the amplitude of the critical current oscillations. However, as shown in Fig. 3.7**b**, the extracted critical current is proportional to the real critical current, as can be seen from the perfect match with the linear fit. This proportionality is tested for both sinusoidal and ballistic CPR of the probe junction. Therefore, the diode efficiency can be found by extracting $I^+_{c,2}$ and $I^-_{c,2}$ from the measured data. The negative critical current needs to be found from $I_c(B_z)$ measurements with negative bias current polarity.

Fig. 3.8**a** shows $I_c(B_z)$ oscillations for both positive and negative polarity of the bias current measured at an in-plane field of $B_y = -50\,\mathrm{mT}$. The critical currents of the measured oscillations are shown in Fig. 3.8**b,c** for different values of the gate voltage.

The diode efficiency is defined as

$$\eta = \frac{I^+_{c,2} + I^-_{c,2}}{(I^+_{c,2} + |I^-_{c,2}|)/2}, \tag{3.12}$$

where $I^\pm_{c,2}$ are the values of the critical current extracted from the data as shown in Fig. 3.8**a**. The resulting diode efficiencies as a function of gate voltage are shown in Fig. 3.9**a-e**. As the measurement of the critical current is affected by drift of the out-of-plane field, all measurements of $I_c(B_z)$ are repeated by cycling the gate voltage many times. The error bars shown in the plots are

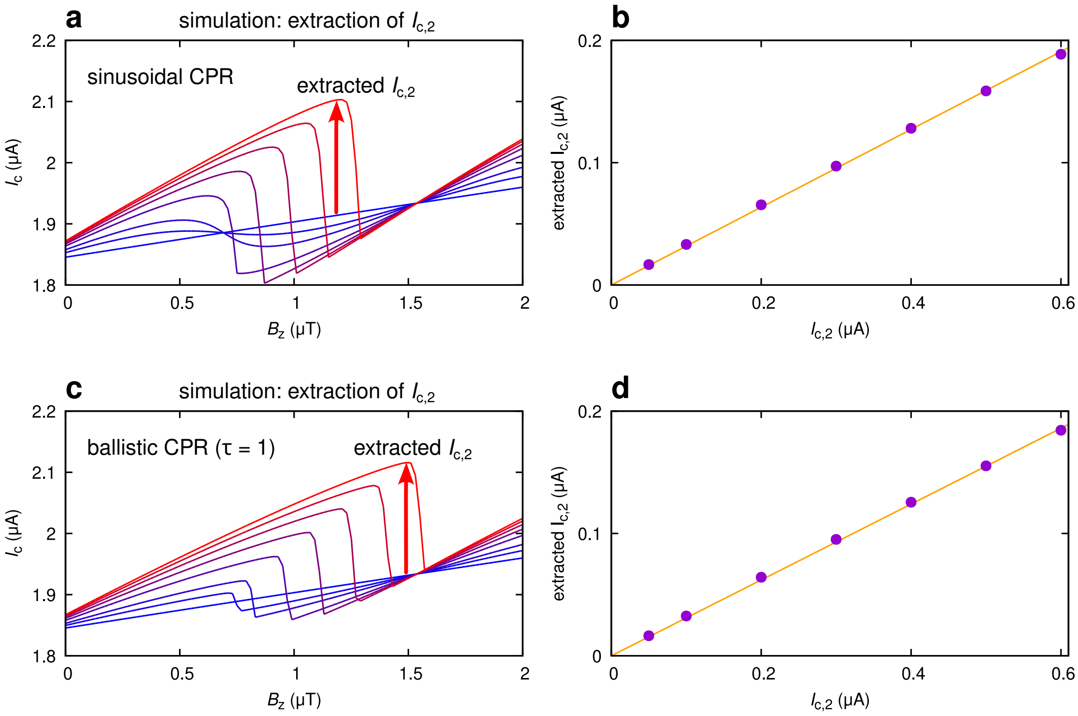

Fig. 3.7.: a, Extraction of the critical current $I_{c,2}$ from the SQUID oscillations. The CPR of JJ2 is $I_2(\gamma) = I_{c,2}\sin(\gamma)$. **b,** Dependence between the extracted and the actual critical current. A linear fit is shown in orange. **c,** Extraction of the critical current for the case where JJ2 has a fully ballistic CPR with transparency $\tau = 1$. **d,** Dependence between the extracted and the actual critical current for the case of a ballistic CPR. A linear fit is shown in orange.

obtained from the standard deviation of the individual measurements. The curves can be fitted using $\eta(V_g) = \eta(-1.5\,\mathrm{V}) + A \cdot V_g$, where the constant A is the gate slope of the diode efficiency. All curves feature a spurious offset $\eta(-1.5\,\mathrm{V})$, which is present even when the applied in-plane field is zero. As shown by simulations, the proportionality constants between the real critical current and the extracted critical current are in general slightly different for each individual SQUID oscillation. The extracted diode efficiency $\eta_{\text{extracted}}$ is then affected by an offset, which is independent of gate voltage. Assuming that α_+ and α_- are the proportionality constants for the positive and negative critical current, the extracted diode efficiency is

$$\eta_{\text{extracted}} = 2\frac{\alpha_+ I_c^+ + \alpha_- I_c^-}{\alpha_+ I_c^+ + \alpha_- |I_c^-|} \sim \eta_{\text{real}} + \frac{\alpha_- - \alpha_+}{\alpha_+}. \tag{3.13}$$

This approximation is valid if α_+/α_- is close to unity. We conclude that only the slope of $\eta(V_g)$, and not the absolute value, can be extracted reliably from the data without having further knowledge of the $\alpha_\pm$ constants. Fig. 3.9**f** shows $d\eta/dV_g$ as a function of the in-plane field applied B_y. The observed curve is anti-symmetric with sharp extrema at $B_y = \pm 50\,\mathrm{mT}$. This is the behavior which is expected from our earlier measurements of the diode effect. In [12] the extrema of the rectification were obtained at slightly larger field of $B_y = \pm 75\,\mathrm{mT}$. The reason for this difference is not clear at the moment. The main difference in

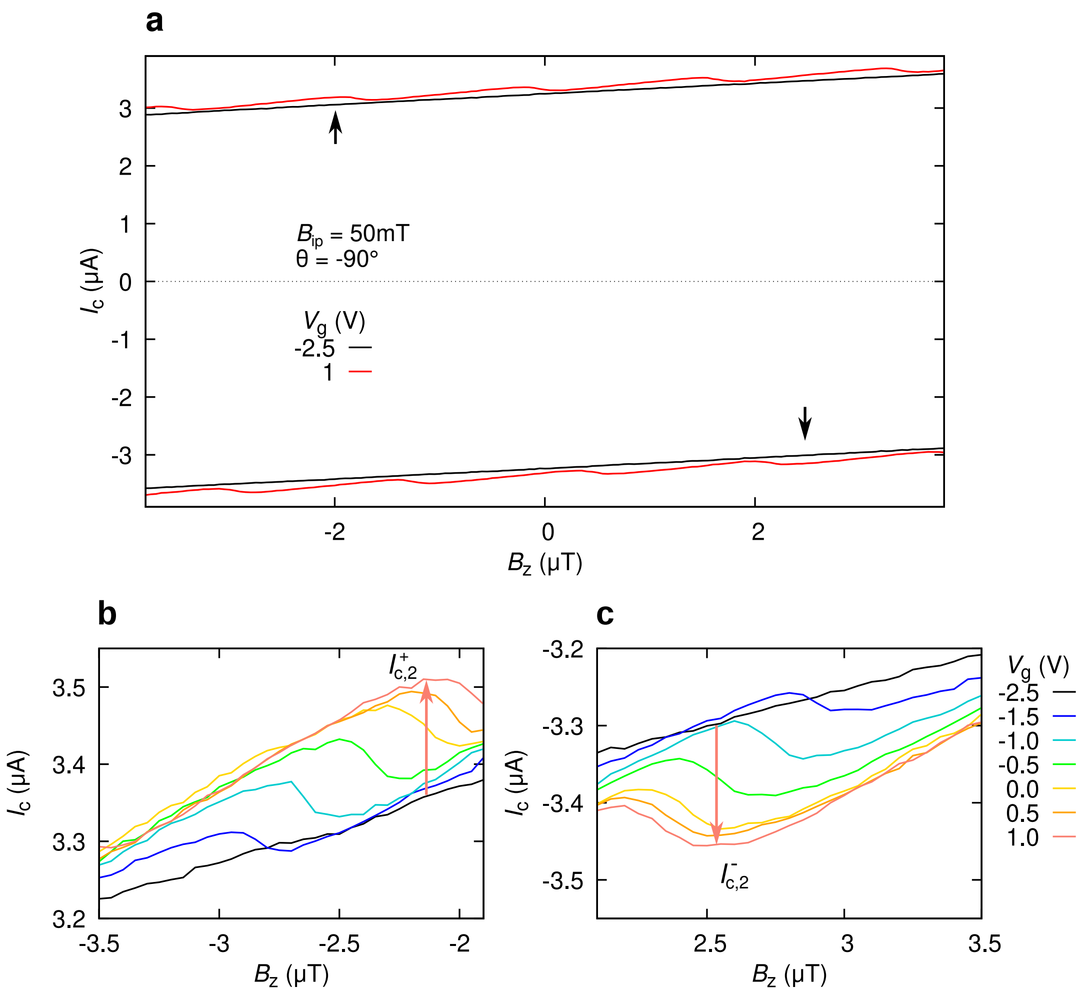

Fig. 3.8.: **a**, Positive and negative critical current of the SQUID device as a function of B_z for $B_{\text{ip}} = 50\,\text{mT}$. The black curve refers to $V_g = -2.5\,\text{V}$ and the red curve refers to $V_g = 1\,\text{V}$. The arrows indicate the SQUID oscillations featured in panels **b** and **c**. **b**, Positive critical current $I_c^+(B_z)$ of the SQUID for different values of the gate voltage. The red arrow indicates the value of $I_{c,2}^+$. **c**, Negative critical current $I_c^-(B_z)$ for different values of the gate voltage. The red arrow indicates the value of $I_{c,2}^-$.

the measurements of C. Baumgartner was a slightly different wafer structure with a indium concentration of 81% in the spacer.

Due to the large screening effects, the measurement of the diode efficiency with our SQUID device is challenging. A more direct measurement with single junctions was performed by the group of J. Shabani [36]. These measurements also show the increase of the diode efficiency with the gate voltage. The gate tunable Josephson diode effect was also observed in experiments with InSb nanowires [44]. In these experiments the nanowires are partially covered with an Al shell. The weak link is created by shadow-wall lithography and shallow-angle Al deposition. The partial superconducting shell of the nanowires allows tuning of the chemical potential in the leads. A separate gate is used to control the potential at the weak link. The diode efficiency is strongly gate tunable

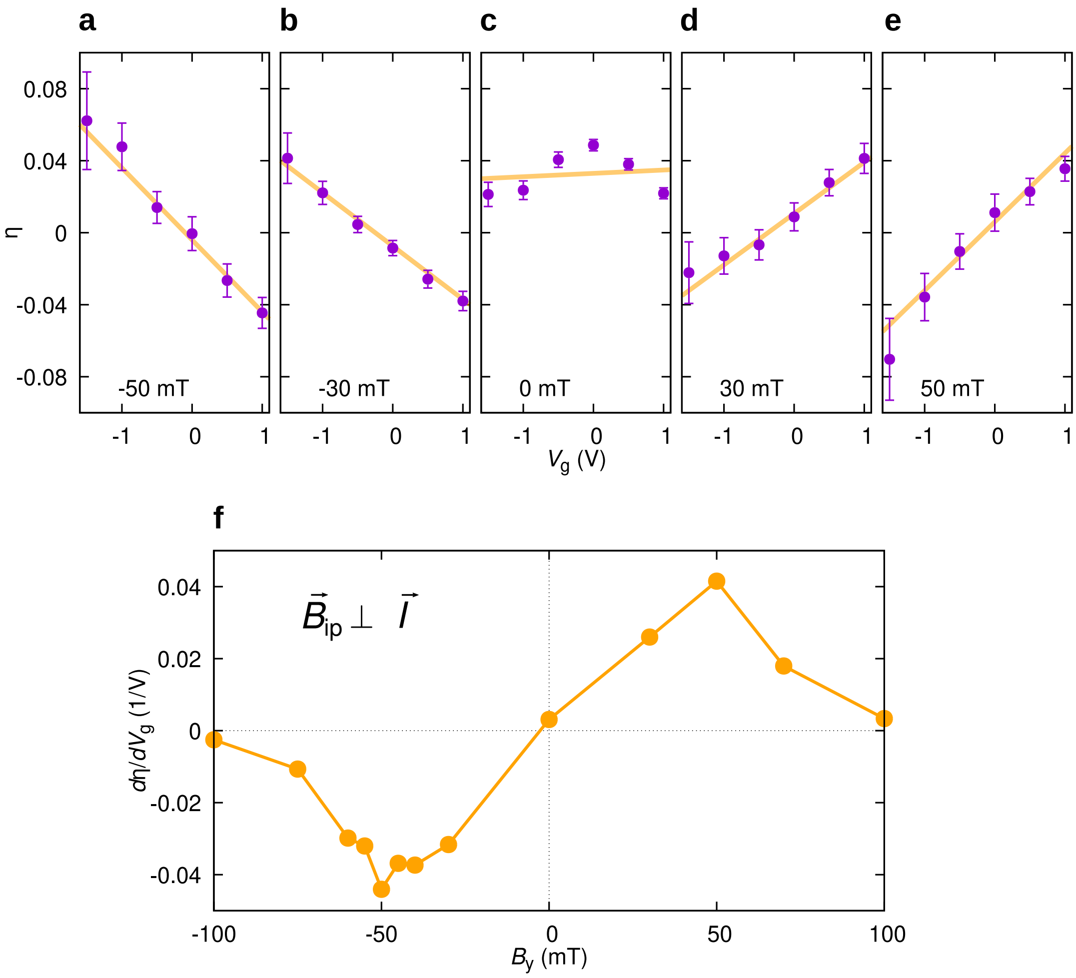

Fig. 3.9.: a-e, Measured diode efficiency $\eta = 2\frac{I^+_{c,2}+I^-_{c,2}}{(I^+_{c,2}+|I^-_{c,2}|)}$ as a function of gate voltage. The panels correspond to values of $B_{\text{ip}} = -50, -30, 0, 30, 50$ mT. The values of $\eta(V_g)$ are averaged over 40 measurements of the SQUID critical current. The error bars correspond to the standard deviation of the individual measurements. **f,** Gate slope of the diode efficiency $d\eta(V_g)/V_g$ plotted as a function of the in-plane magnetic field B_y.

and this result is interpreted as a consequence of gate-tunable SOI and g-factor in the proximitized part of the nanowire.

3.5. Temperature dependence of the anomalous phase shift and the Josephson diode effect

Unlike the anomalous phase shift, the Josephson diode effect requires higher harmonics in the current-phase relation. As was presented an Fig. 2.8 of the previous chapter, the theoretical models predict that the Josephson diode effect is strongly suppressed by increasing the temperature. On the other hand, it is expected that the anomalous phase shift has very little temperature dependence. In order to check these predictions we now use the SQUID device to perform measurements of $\Delta\varphi_0$ and $d\eta/dV_g$ as a function of temperature. The results are presented in Fig. 3.10. The anomalous phase shift is mea-

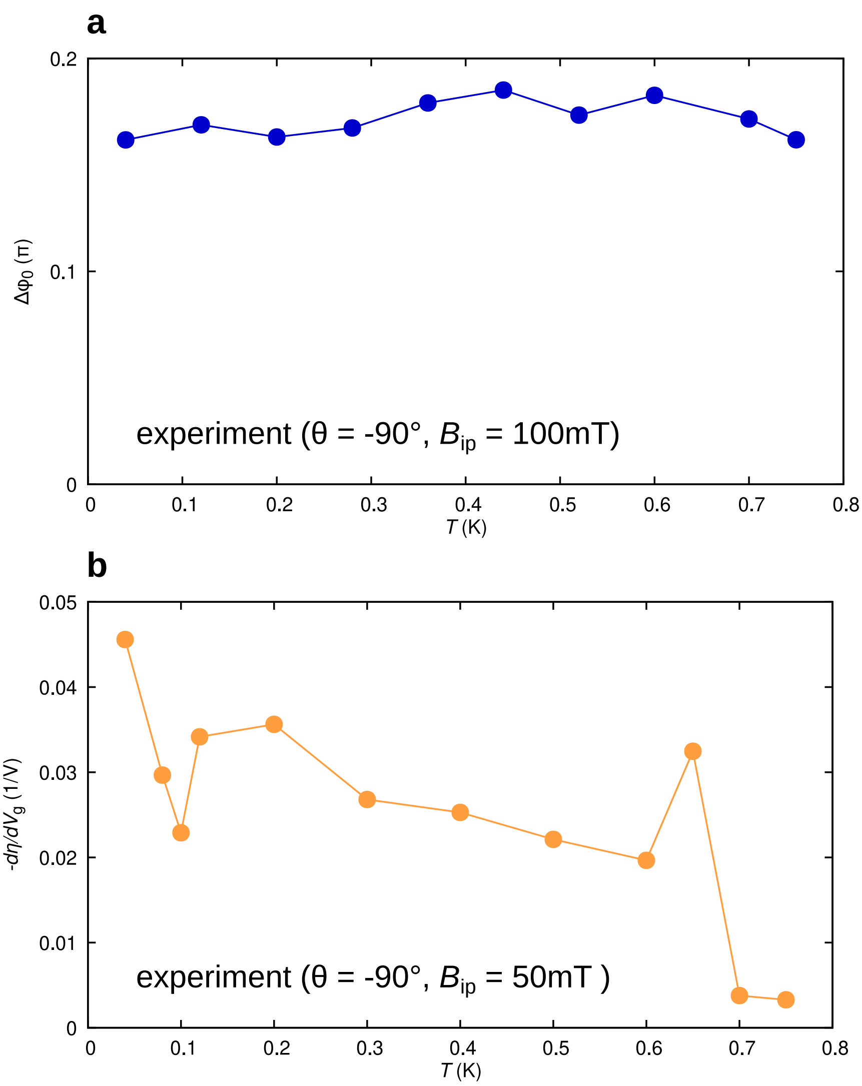

Fig. 3.10.: a, Measurement of the anomalous phase shift $\Delta\varphi_0(V_g = 1\,\mathrm{V})$ as a function of temperature. The in plane field is set to $B_y = -100\,\mathrm{mT}$. **b,** Measurement of $d\eta/dV_g$ as a function of temperature. The in-plane field is set to $B_y = -50\,\mathrm{mT}$.

sured at $B_y = -100\,\mathrm{mT}$ and shows very little temperature dependence up to $T = 700\,\mathrm{mK}$. The Josephson diode effect is measured at $B_y = -50\,\mathrm{mT}$ where $d\eta/dV_g$ is maximal. A decrease with temperature is clearly visible. The data points of $d\eta/dV_g(T)$ show a large scatter, especially at higher temperatures. This is due the reduced critical current at larger temperatures, which increases the error in the determination of the diode efficiency. Moreover, the transition between superconducting and normal state in the $dV/dI(I_{\mathrm{Bias}})$ measurements becomes less sharp at higher temperatures, resulting in a further increase of the error. Fig. 3.11 shows the measurement of $d\eta/dV_g$ for $T = 40\,\mathrm{mK}$ and $T = 750\,\mathrm{mK}$, which are the lowest and highest temperatures for which the diode effect is measured. The statistical errors in the determination of the

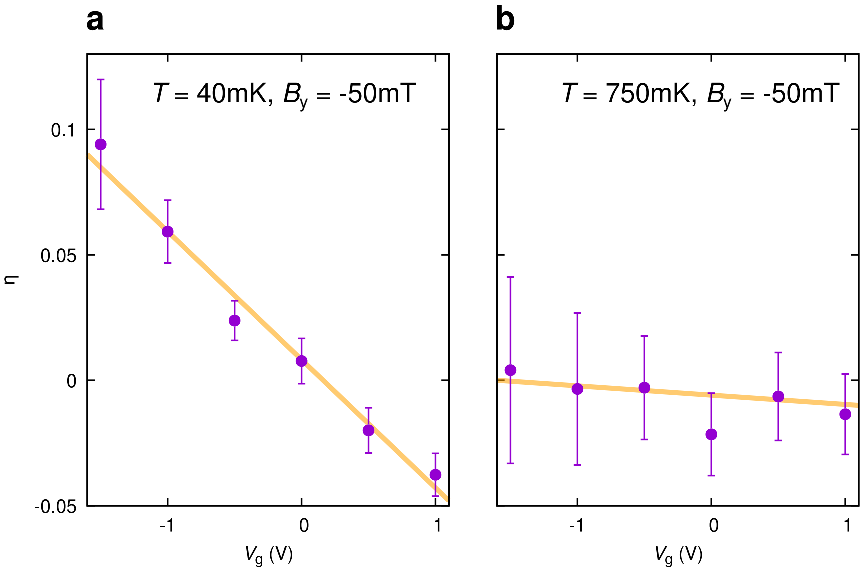

Fig. 3.11.: Measurement of $\eta(V_g)$ for $T = 40\,\mathrm{mK}$ (**a**) and $T = 750\,\mathrm{mK}$ **b**. The values are determined by averaging over 40 cycles of the gate voltage. The error bars represent the standard deviation of the data points recorder for each gate voltage.

diode efficiency are strongly increased at $T = 750\,\mathrm{mK}$. This explains why the scatter in Fig. 3.10**b** is increased at the higher temperatures.

The measured suppression of the diode efficiency is in good agreement with our earlier experiments on the non-reciprocal Josephson inductance. There, the non-reciprocity of CPR was quantified using the parameter $L_0' := dL/dI(I_{DC} = 0)$ [12]. The measurements of $L_0'(T)$, shown in Fig. S5 of [12], show an exponential decrease of $L_0'(T)$ with temperature. At $T = 300\,\mathrm{mK}$ the ratio $\gamma_L \sim L_0'/L_0$ is only 50% of the value measured at the base temperature $T \sim 50\,\mathrm{mK}$. This is explained by the suppression of the higher harmonics in the CPR with temperature.

4. Vortex ratchet effect in two-dimensional Josephson junction arrays

The properties of two-dimensional arrays of Josephson junctions (2D JJAs) were studied in depth in the 80s and 90s [13]. The JJAs serve as an important model system in condensed matter physics. The transport properties of two-dimensional JJAs are determined by vortices. Motion of vortices under the influence of a bias current results in a finite resistance. The motion is strongly affected by the pinning of vortices and the repulsive vortex-vortex interaction.

In this chapter we study the transport properties of JJAs with sub-micrometer lattice constants fabricated from Al/InAs superconductor-semiconductor heterostructures. The most striking observation is a vortex ratchet which is observed when an in-plane magnetic field is applied to the array. The key signature of the ratchet effect is a difference in vortex depinning currents for positive and negative polarity of the current bias. Vortex ratchet effects have been observed in earlier works featuring JJAs and nanopatterned superconducting films. In these works an anisotropic vortex pinning was induced by a anisotropic device geometry or anisotropic shape of the pinning sites. In contrast, here we observe a vortex ratchet effect in a highly symmetric device with fourfold rotational symmetry. The effect is explained by the anomalous phase shift in the presence of long range Josephson coupling between the islands. Our model of the JJA, developed together with the group of Felix von Oppen at FU Berlin, extends the standard XY model of square arrays with next-nearest neighbor interactions and anomalous phase shifts.

The results presented in this chapter are published in the preprint [45].

4.1. Frustration in Josephson Junction Arrays

In this chapter we study the superconducting regime of transport in JJAs where the normal state resistance of the individual junctions is far below the resistance quantum, i.e., $R_N \ll R_Q = \frac{h}{e^2} = 25.8\,\mathrm{k}\Omega$. In this case the charge on the islands is not discrete and the value of the superconducting phase on each island is a classical variable, i.e., quantum fluctuations of the phase can be neglected.

The opposite case of an array in the Coulomb blockade regime with insulating behavior is studied in Chapter 6.

The JJA is described by the frustrated XY model [13, 46, 47, 48]. We label the phases on the array islands as φ_i. The free energy is determined by the Josephson coupling energy between neighboring islands

$$F = \sum_{i,j} -E_J \cos\left(\varphi_j - \varphi_i - \frac{2\pi A_{ij}}{\Phi_0}\right). \tag{4.1}$$

The out-of-plane magnetic field is encoded in the terms A_{ij}, which are the line integrals of the vector potential between neighboring islands. Summing the vector potential terms around one plaquette gives $\sum_{\text{plaquette}} A_{ij} = \Phi = B_z a^2$, where a^2 is the area of the unit cell. The current from island i to a neighboring island j is given by

$$I_{ij} = \frac{2\pi}{\Phi_0}\frac{\partial F}{\partial(\varphi_j - \varphi_i)} = I_c \sin\left(\varphi_j - \varphi_i - \frac{2\pi A_{ij}}{\Phi_0}\right). \tag{4.2}$$

The effect of the out-of-plane field is typically quantified using the frustration parameter $f := \sum_{\text{plaquette}} A_{ij}/\Phi_0 = B_z a^2/\Phi_0$, which is the flux per unit cell given in units of the superconducting flux quantum. A gauge invariant phase difference between islands j and i is defined as $\gamma_{i\to j} = \varphi_j - \varphi_i - \frac{2\pi A_{ij}}{\Phi_0}$. Similar to the case of the SQUID studied in the previous chapter, the gauge invariant phase differences are constraint by a fluxoid quantization condition

$$\sum_{\text{plaquette}} \gamma_{i\to j} = 2\pi(f + N), \tag{4.3}$$

where the integer N gives the winding number of the gauge invariant phase around the plaquette.

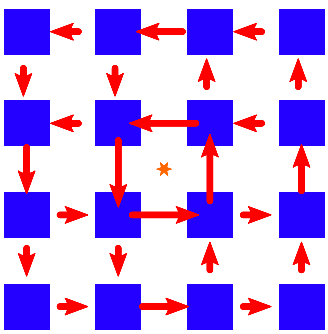

Fig. 4.1.: Current configuration around the core of a vortex. The core of the vortex is located in the center of the array. The magnitude of the Josephson currents is indicated by the length of red arrows between superconducting islands. The orange star indicates the position of the vortex, located at a minimum of the vortex pinning potential.

Similar to type-II superconductors, JJAs can host vortices. For simplicity we first consider the case without applied field, i.e. $f = 0$. Summing the gauge invariant phases in a loop around the core of a vortex gives a value of $2\pi n$ where $n = \pm 1$ is the *vorticity*. Vortices with negative vorticity are referred to as antivortices. For a vortex in the array at position (x_0, y_0), the phases can be approximated by $\varphi(x, y) = \text{arctan2}(y - y_0, x - x_0)$. Here $\text{arctan2}(y, x) = \arg(x + iy)$ is the 2-argument arctan function producing values in the interval $[0, 2\pi)$.

Using this approximation, the energy of the vortex as a function of the position of the vortex core is then found by plugging $\varphi(x, y)$ into Eq. (4.1). The resulting *vortex pinning potential*

$$U(x, y) \sim E_B(\cos(2\pi x/a) + \cos(2\pi y/a)) \tag{4.4}$$

has minima located between four adjacent islands. The configuration of Josephson currents for a vortex located at a minimum of $U(x, y)$ is shown in Fig. 4.1. The barrier energy E_B is approximately 10% of the Josephson energy E_J. When applying a transport current with density $\vec{j}$, vortices experience a Lorentz force $\vec{F}_L = \Phi_0 \vec{j} \times \vec{z}$ perpendicular to the applied current. Depinning of vortices occurs when the Lorentz force exceeds the maximal gradient of the pinning potential. For a single vortex in a square array the depinning current per junction (total current divided by the number of rows in the array) is given by $I_d = 2\pi E_B/\Phi_0$, which is approximately 10% of the Josephson critical current of the individual junctions.

An applied out-of-plane magnetic field is screened by the induced currents in the array. The magnetic penetration depth of the JJA is found from the result of Pearl, which is valid for thin superconducting films. The JJAs can be viewed as a discretized version the thin film. The penetration depth is given by [13, eqn. 6.64]

$$\lambda_\perp = \frac{\Phi_0}{2\pi\mu_0 I_c}, \tag{4.5}$$

where I_c is the critical current of a single junction. For the array studied in this chapter the upper limit of the critical current is $I_c \sim 500\,\text{nA}$, so that $\lambda_\perp > 500\,\mu\text{m}$. As this largely exceeds the dimensions of the device, we do not have to take screening effects into account.

For a large array in an out-of-plane field B_z, the equilibrium number of vortices in the array will be $N_v = B_z A/\Phi_0$, where A is the total area of the array. The average number of vortices per unit cell of the array is then given by the frustration parameter f. In the ground state the configuration of vortices minimizes the total energy given by Eq. (4.1). The ground state configurations for $f = 1/2$, $f = 1/3$, and $f = 2/5$ were found in the early work of Teitel and Jayaprakash [49]. The vortex patterns of these ground states are presented in Fig. 4.2. For these values of rational frustration $f = p/q$ the currents and phases are periodic with a $q \times q$ unit cell. This is not true in general. For examples, one of the two ground states for $f = 1/4$ is only periodic on a 8×8 cell [47]. Low energy configurations of the vortices for larger values of q can be found numerically, typically by using simulated thermal annealing algorithms [48].

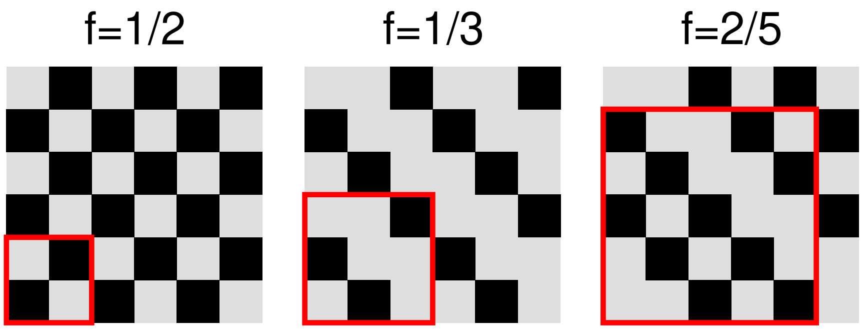

Fig. 4.2.: The known ground state configuration of vortices for frustrations $f = 1/2, 1/3$, and $f = 2/5$. Each square corresponds to a site located between four adjacent superconducting islands. The unit cell of the vortex lattices are indicated with red rectangles.

In this chapter we will study how an anomalous phase shift φ_0 in the current phase relation affects the physics of two-dimensional JJAs. The basic situation is sketched in Fig. 4.3. An in-plane field applied in the y-direction induces a φ_0 shift for all junctions in the x-direction, so that the free energy of a junction in the x-direction is given by

$$F = -E_J \cos(\varphi_j - \varphi_i - \varphi_0 - 2\pi A_{ij}/\Phi_0). \tag{4.6}$$

Adding the anomalous phase shifts to the XY model is equivalent to a gauge transformation of the magnetic vector potential, i.e., $2\pi A_{ij}/\Phi_0 \to 2\pi A_{ij}/\Phi_0 + \varphi_0$. This gauge transformation changes the phases as $\varphi \to \varphi + n_x\varphi$, where the integer n_x is the index of an islands coordinate in the x-direction. However, all Josephson energies and currents are unaffected by the transformation, as the frustration parameter f is not changed by the gauge transformation. From this we conclude that the anomalous phase shift in the x-direction has no observable consequences on the transport properties of the array. As we will see, this is not true for the nanoscale arrays studied here.In order to model the non-reciprocal effects caused by the anomalous phase shift, we will have to extend the XY model with next-nearest-neighbor couplings.

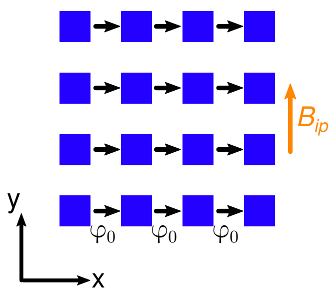

Fig. 4.3.: JJA with in-plane field applied in the y-direction. All junctions in the x-direction feature an anomalous phase shift, indicated with black arrows.

4.2. Two-dimensional Josephson junction array device

The JJA device is fabricated from the Al/InAs wafer *M01-08-22.1*, which was also used for the asymmetric SQUID experiment presented in Chapter 3. The junctions are defined by electron beam lithography followed by selective wet-etching of the Al film. The resulting array consists of 200×200 aluminum islands separated by 100 nm wide gaps where the aluminum is removed. The islands are $400 \times 400\ \mathrm{nm}^2$ in size. The lattice constant of the array is $a = 500\,\mathrm{nm}$, and the out-of-plane field corresponding to frustration $f = 1$ is $B_0 = \Phi_0/a^2 \sim 8.2\,\mathrm{mT}$. A sketch of the array geometry and the contacts is shown in Fig. 4.4**a**. Transport measurements are performed in a quasi-four-point setup. A global top gate is used to control the carrier density in the electron gas below the junctions where aluminum is removed. The resulting chip features 16 array devices, which differ by the electron beam exposure used for writing the junctions. Two of the 16 array devices, referred to as devices A and B, are contacted with bond wires. Scanning electron microscopy images of device A are shown in Fig. 4.4**b,c**. The SEM images were taken before the deposition of the AlOx gate dielectric. All measurements presented in this chapter are performed on device A, unless stated otherwise.

The temperature dependence of zero-bias differential resistance of the array is shown in Fig. 4.5**a**. Unlike the $R(T)$ curve of the superconducting film, shown in Appendix A, the resistance does not immediately drop to zero below the critical temperature of the aluminum film $T_{c,\mathrm{Al}} \sim 2.1\,\mathrm{K}$. A strong decrease of resistivity occurs when further cooling below $T \sim 1.2\,\mathrm{K}$. The strong decrease of the resistivity below 1.2 K marks the onset of strong Josephson coupling and phase coherence between the aluminum islands.

The resistance of the device measured as a function of the out-of-plane magnetic field B_z is shown in Fig. 4.5**b**. Due to the fast sweep of the magnetic field the temperature of the sample is increased to $\sim 200\,\mathrm{mK}$ in the measurement. A dip of the resistance is found at $B_{c,\mathrm{Al}} \sim 150\,\mathrm{mT}$. At this field a large number of vortices will be present in the array, as $f \gg 1$. At high vortex density the pinning is very low, causing dissipation due to vortex motion at arbitrarily low bias currents. This changes for $B_z \sim B_0 = 8.2\,\mathrm{mT}$ below which stronger vortex pinning results in zero differential resistance for sufficiently low excitation currents.

Determining the electron density in the semiconductor quantum well covered with the aluminum film is difficult for most sample geometries, as even in the normal state the aluminum has a much lower sheet resistance than the electron gas in the quantum well, making it impossible to measure the Hall effect of the semiconductor. The first measurement of the electron density in an InAs quantum well covered with aluminum was performed using the cyclotron resonance response in THz spectroscopy [50].

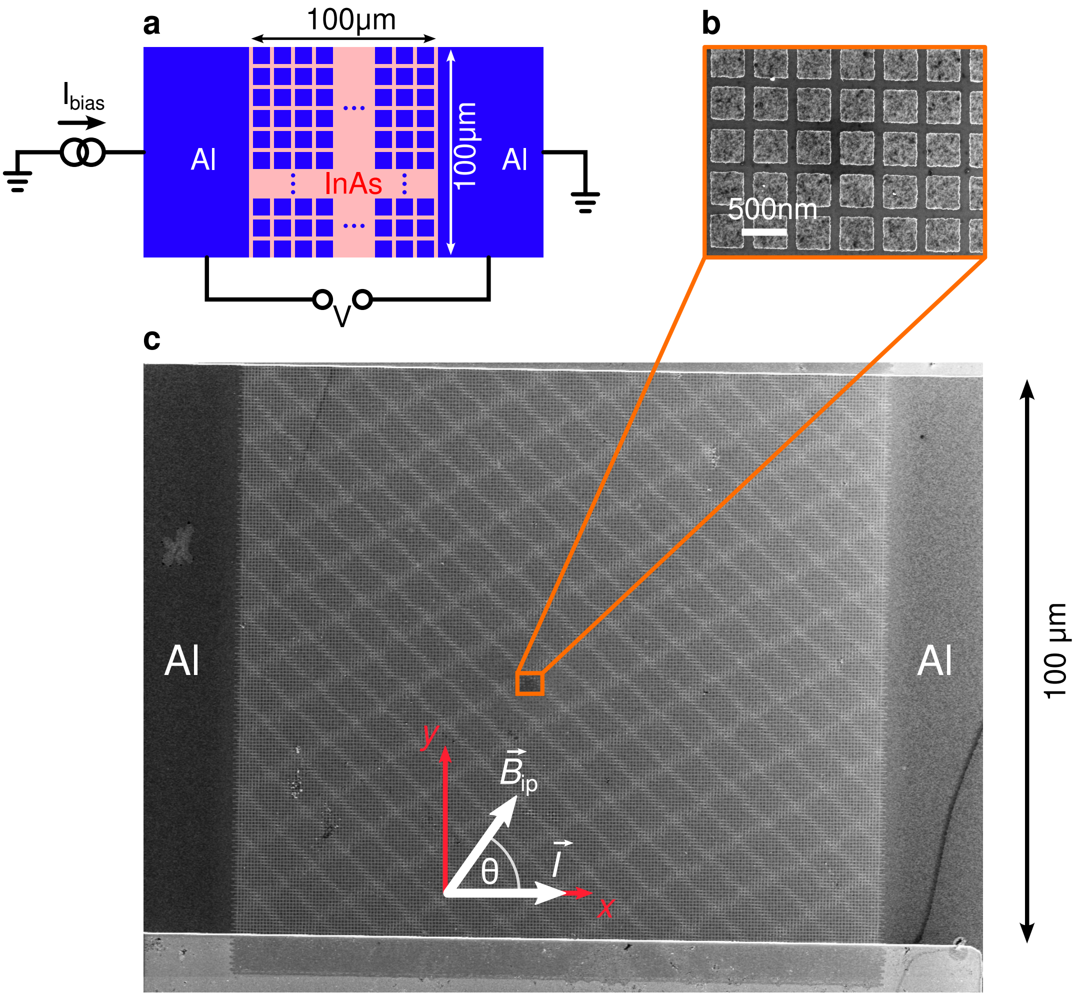

Fig. 4.4.: **a,** Sketch of devices A and B. **b,** High-resolution SEM image of the JJA. Aluminum islands with size 400 × 400 nm are separated by junctions with length ∼ 100 nm. **c,** SEM image of device A. The oscillating brightness on the array is an imaging artifact due to interference of the image pixel size and the lattice constant. SEM images in **b** and **c** were taken before the growth of the gate dielectric.

The two-dimensional JJA device enables a novel probe of the electron density in the Al-covered quantum well using standard magnetotransport techniques. Due to the low lattice constant $a = 500\,\mathrm{nm}$, the aluminum islands due not shunt the electron gas in the semiconductor and an applied transport current must flow through the quantum well. This becomes evident as the sheet resistance of the array of $\sim 500\,\Omega$ is much larger compared to the sheet resistance of the aluminum film $R_{\square,\mathrm{Al}} \sim 36\,\Omega$. Fig. 4.6**a** shows the differential resistance of the array as a function of out-of-plane magnetic field for different gate voltages. Fig. 4.6**b** shows the same data after removing a second-order polynomial background. This graph shows Shubnikov de-Hass (SdH) oscillations, which are clearly visible for $1/B_z < 0.8$. The electron density corresponding to the oscillations is $9.0 \times 10^{11}\,\mathrm{cm}^{-2}$ with no apparent dependence on gate voltage. This indicates that the SdHs probe the electron density in the semiconductor covered by Al, where the effect of the gate is screened. The obtained density is in excellent agreement with the value $n = 8.5 \times 10^{11}\,\mathrm{cm}^{-2}$ found using THz

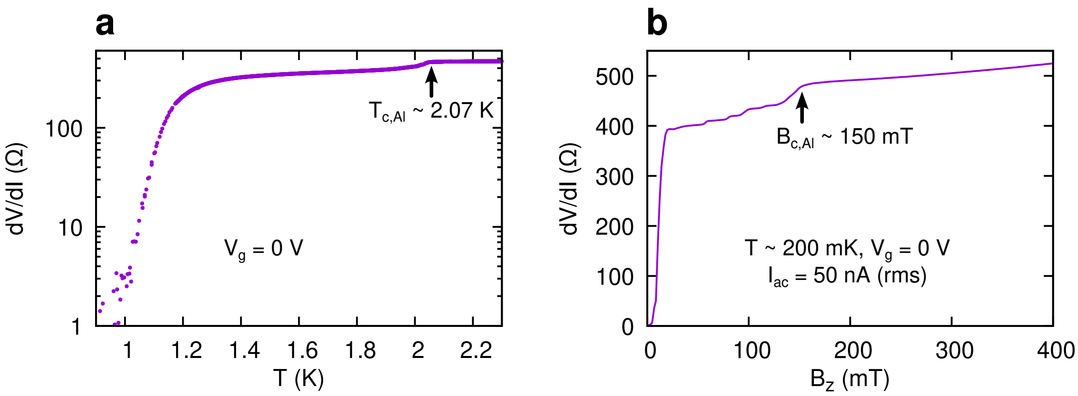

Fig. 4.5.: a, Zero-bias differential resistance of the array as a function of temperature. **b,** Zero-bias differential resistance of the array as a function of the out-of-plane magnetic field. The critical field of the aluminum film is visible as the first drop of resistance at $B_z \sim 150\,\mathrm{mT}$, marked with a black arrow.

spectroscopy on a very similar Al/InAs heterostructure [50]. The linear part of the magnetoresistance is caused by the two-terminal measurement, where voltage is probed on the terminals which are used to source the current. The two-terminal resistance probes both the longitudinal resistance and the Hall resistance [51].

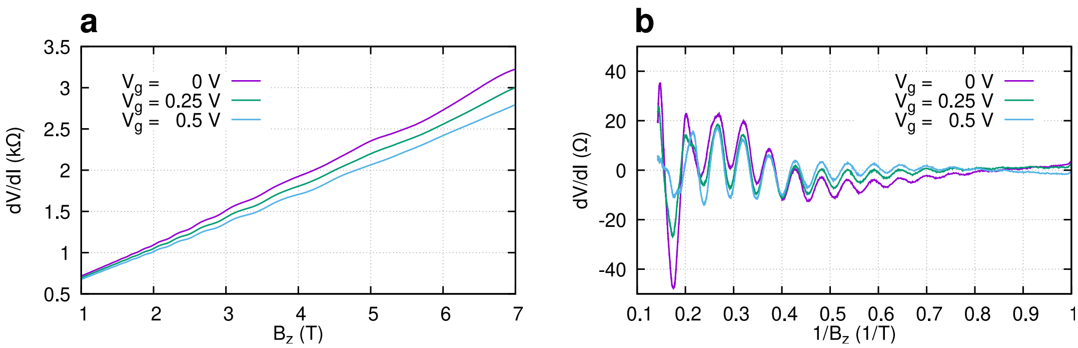

Fig. 4.6.: a, Two-point measurement of magnetoresistance in the normal state as a function of out-of-plane magnetic field. The temperature is $T \sim 200$ mK. **b,** Magnetoresistance data after substraction of a quadratic polynomial background, plotted as a function of $1/B_z$.

4.3. Characterization in an out-of-plane magnetic field

A first characterization of the superconducting transport properties of the JJA is performed by studying the non-linear transport properties as a function of the out-of-plane magnetic field which tunes the density of vortices in the array. This is performed by measuring the differential resistance using a small ac current excitation on top of a dc bias current. The field is varied in the range $-12\,\mathrm{mT}\ldots 12\,\mathrm{mT}$. The resulting map of the differential resistance is shown in Fig. 4.7. When the dc bias current is below the depinning current the differential resistance is zero (black regions). Peaks of the depinning current are observed at several commensurate values of the frustration parameter. The most pronounced peaks are found at $|f| = 0, 1, 1/3, 1/2$, and $2/3$. Smaller features can be found at $|f| = 1/6, 1/5, 1/4$, $2/5$, and $3/5$. The position of the peaks at $f = \pm 1$ fits perfectly to the calculated value of the integer matching field $B_0 = \Phi/a^2 = 8.2\,\mathrm{mT}$. The transport properties are clearly not periodic in f. In particular, the critical current at $f = 1$ much smaller compared to $f = 0$. This is because the junctions have a finite area and the magnetic field generates Fraunhofer interference in each junction. The first node of the Fraunhofer interference pattern is expected at a field corresponding to one flux quantum per junction. As the number of junctions is twice the number of islands, this occurs at $f = 2$. The range of field shown in Fig. 4.7 corresponds to the central lobe of the Fraunhofer pattern.

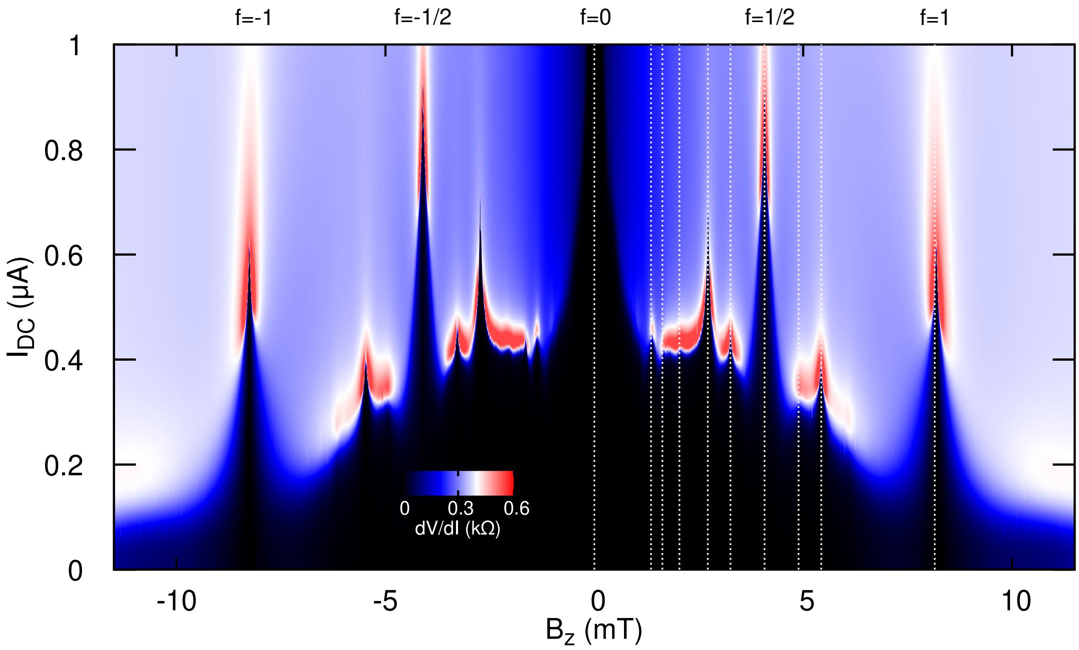

Fig. 4.7.: Differential resistance at zero in-plane magnetic field and $T \sim 40$ mK measured as a function of out-of-plane field B_z and dc bias current. Peaks of the depinning current are found at the indicated dotted lines at $f = B_z/B_0 = 0$, $1/6$, $1/5$, $1/4$, $1/3$, $2/5$, $1/2$, $3/5$, $2/3$, and 1. The measurement is performed with an ac-excitation of 10 nA at frequency 777 Hz.

The critical current in the vicinity of $B_z = 0$ is not visible in Fig. 4.7, as it largely exceeds $1\,\mu\mathrm{A}$. This regime is studied in separate $V(I)$ measurements. The strong vortex pinning at low fields results in hysteretic behavior when changing the out-of-plane field and the results of a measurement at a given field B_z depend on the history of the field. This can be overcome by thermal annealing. After each change of B_z the sample is heated above the critical temperature of the aluminum film and then field cooled until the temperature is sufficiently low. We use an on-chip heater in order to minimize the heat load on on the cold finger and the mixing chamber. Fig. 4.8**a** shows the resulting $I(V)$ curves for different values of B_z. The largest field of $B_z = 90\,\mu\mathrm{T}$ corresponds to $f \sim 0.011$. After thermal annealing the current is increased starting from zero followed by a back-sweep to zero. A zoom into the low-voltage part is shown in Fig. 4.8**b**. For $|B_z|$ close to zero we observe a discontinuous jump of the voltage from zero to a dissipative state. Starting at $|B_z| = 3\,\mu\mathrm{T}$ there is a regime of vortex creep with finite resistance and nearly constant slope of $V(I)$, which is followed by a jump in voltage to the strongly dissipative state. At $B_z = 90\,\mu\mathrm{T}$ the $I(V)$ is continuous and does not show any hysteresis. A color map of the voltage at positive sweep direction is shown in Fig. 4.8**c**. The dark blue region corresponds to the zero voltage state, while the red region corresponds to the dissipative normal state. The flux creep occurs in the white/pink regions. We expect that the critical current at nominally zero out-of-plane field is also related to vortex depinning. The observed critical currents are far below the currents where the individual junctions reach the Josephson critical current. For the present device this would be expected for a current density of $\sim 1\,\mu\mathrm{A}/\mu\mathrm{m}$, corresponding to a current of $100\,\mu\mathrm{A}$. The observed critical current is much lower by a factor of 10, which is the expected behavior in JJAs as already stated above in this chapter.

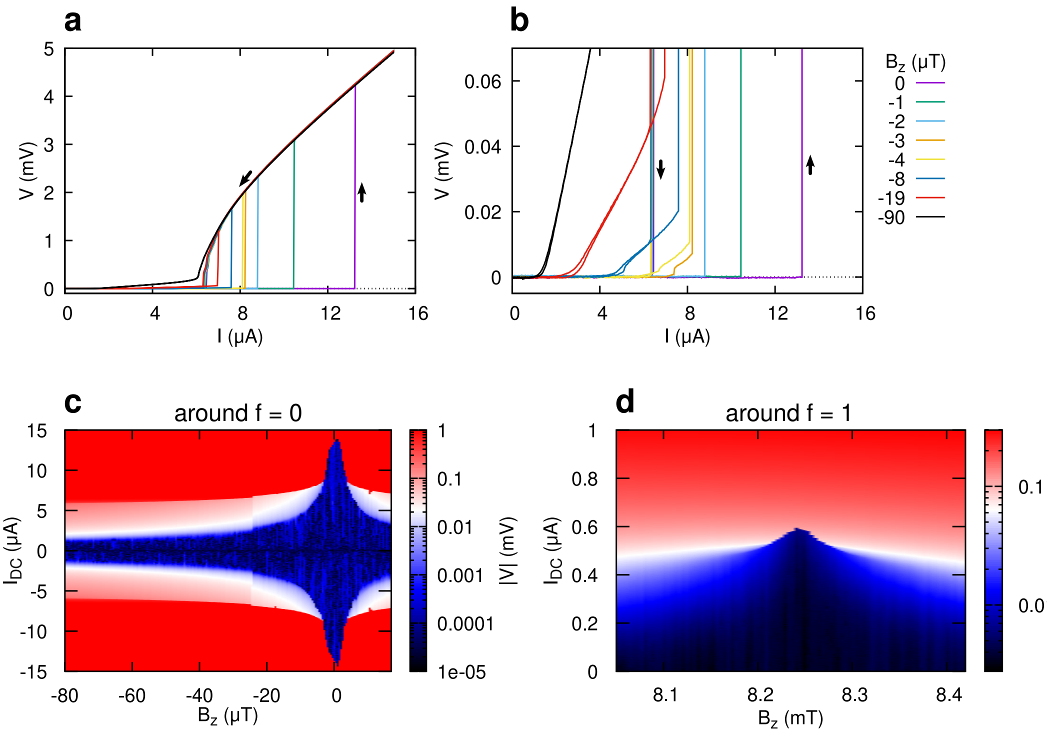

Fig. 4.8.: a, $V(I)$ curves for low out-of-plane fields. Black arrows indicate the sweep direction, showing the hysteresis between up and down sweep of the current. Field-cooling is performed for each measurement after setting B_z to the new value. A heat pulse with power $P \sim 0.5\,\mathrm{mW}$ is applied for 1 s followed by a cooling time of 2 min. The $V(I)$ measurements always start at zero bias current. **b,** Zoom into the low voltage part of panel **a**. **c,** Color map of $\log(|V|(B_z, I))$ around zero frustration. **d,** Color map of $\log(V(B_z, I))$ around integer frustration $f = 1$.

The same measurement is performed around integer frustration $f = 1$. The resulting map of the voltage is shown in Fig. 4.8**d**. While the critical currents are much lower, the qualitative behavior is the same as for $f = 0$. In particular we still observe a discontinuous jump of the voltage from zero to the normal state when the frustration is very close to 1.

4.4. Observation of the magnetochiral vortex ratchet effect

Applying an in-plane magnetic field to the array gives rise to magnetochiral effects caused by the interplay of Rashba SOC and Zeeman field. In particular we expect that all junctions perpendicular to the in-plane field will acquire an anomalous phase shift as sketched in Fig. 4.3. Our main observation when applying in-plane fields to the array is a novel type of vortex ratchet effect. In this section we give a detailed description of the experimental observations. A minimal theoretical model which captures the effect is then introduced in the following section 4.5.

Fig. 4.9**a** shows $V(I)$ characteristics of the array device with an applied in-plane magnetic field with magnitude $B_{\mathrm{ip}} = 250\,\mathrm{mT}$. The measurement is performed for both polarities of the bias current and both polarities are compared by plotting the absolute values of voltage and current. A large difference in critical currents is visible when the field is applied perpendicular to the current (purple). In the parallel configuration (green) both curves are on top of each other. The non-reciprocity of critical currents can be quantified by the rectification efficiency (also referred to as diode efficiency)

$$\eta = \frac{\Delta I_c}{I_{c,\mathrm{mean}}} = 2\frac{I_c^+ - |I_c^-|}{I_c^+ + |I_c^-|}. \tag{4.7}$$

We now study how the rectification efficiency depends on the out-of-plane field (i.e. the density of vortices/antivortices) and the gate voltage. Fig. 4.9**b-d** shows measurements of η as a function of B_z for different values of the gate voltage. The magnitude of the in-plane field is $B_{\mathrm{ip}} = 250\,\mathrm{mT}$. Each panel presents a different orientation of the in-plane field. The rectification efficiency is approximately symmetric in B_z, i.e., $\eta(B_z) \sim \eta(-B_z)$ with a maximum of η at zero out-of-plane field. The measurements shown in Fig. 4.9**b-d** are performed by sweeping the out-of-plane field at base temperature. The slight asymmetry of $\eta(B_z)$ is reduced in measurements shown below, where thermal annealing is performed for each individual value of B_z.

The dependence of η on the orientation of the in-plane field coincides with that known from the anomalous phase shift and the Josephson diode effect. In particular the rectification efficiency is strongly reduced for the parallel configuration of current and field and is anti-symmetric in B_y, i.e., $\eta(B_y) = -\eta(-B_y)$.

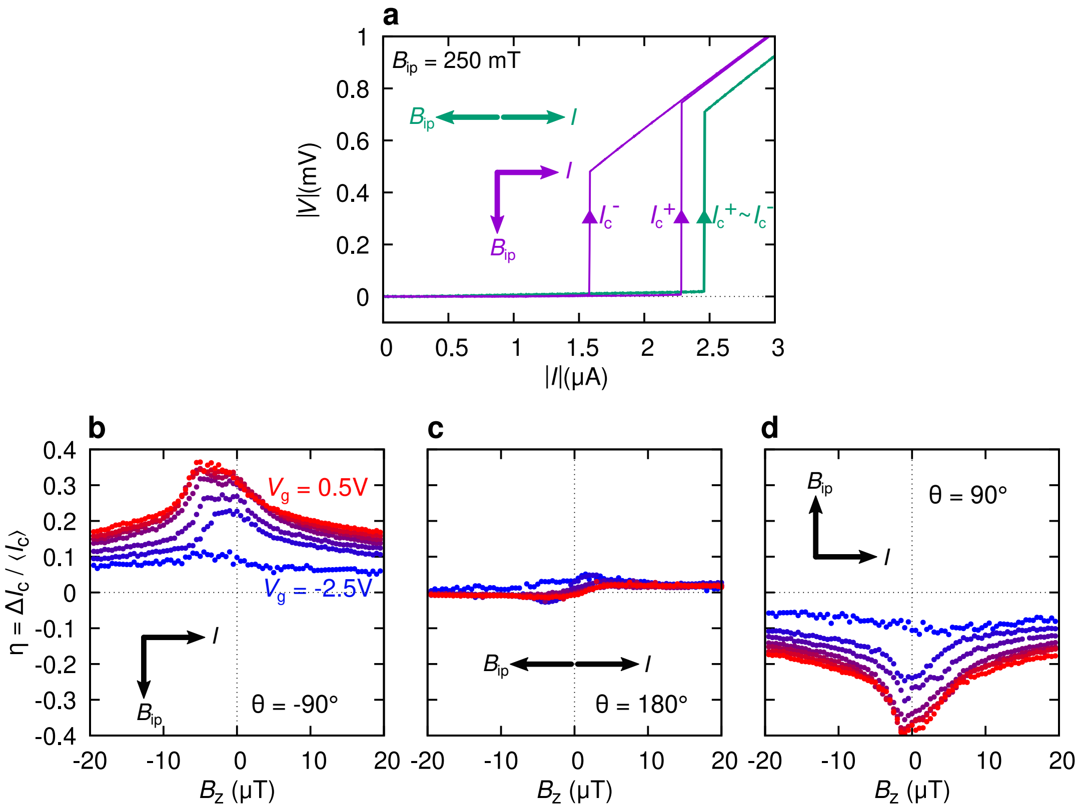

Fig. 4.9.: a, Current-voltage characteristics of the 2D JJA device for different orientations of the in-plane field, with $B_{\text{ip}} = 250$ mT. **b-d,** Rectification efficiency $\eta = \Delta I_c/I_{\text{c,mean}}$ for different orientations (black arrows) of the in-plane field, measured at $B_{\text{ip}} = 250$ mT and temperature $T \sim 40\,\text{mK}$. The color corresponds to different values of the gate voltage V_g, varied in steps of 0.5 V from −2.5 V to 0.5 V. The temperature is kept constant at $T = 40\,\text{mK}$. The out-of-plane field B_z is always swept from $-20\,\mu\text{T}$ to $20\,\mu\text{T}$.

The gate dependence of η is presented in Fig. 4.10**a** where the average of η over the interval $B_z = -20\,\mu\text{T} \ldots 20\,\mu\text{T}$, labeled $\bar{\eta}$, is plotted versus gate voltage. The effect depends monotonically on gate voltage and is suppressed for negative gate voltages. The dependence on the magnitude of the in-plane field is shown in Fig. 4.10**b,c**. Plotting the value of $\bar{\eta}$ versus B_{ip} shows a monotonic increased of $\bar{\eta}$ up to the largest applied field of 250 mT and a nearly linear behavior for fields up to 125 mT. A small non-reciprocal effect remains for zero in-plane field. Diode effects in the absence of an in-plane field have been observed in thin films [52, 53]. There, the rectification was linked unequal vortex barriers at the film edges due to asymmetric defect configurations on the film edges. In our case, a similar geometric mechanism is likely responsible for the rectification at zero in-plane field.

Detailed measurements of the critical current and $\bar{\eta}$ as a function of the angle θ between current and in-plane field are presented in Fig. 4.11. The averaged depinning current shows pronounced maxima when the field is parallel to the current ($\theta = 0, \pi$) and minima when the field is perpendicular to the current ($\theta = \pi/2, 3\pi/2$). The angle dependence of the averaged diode efficiency shows

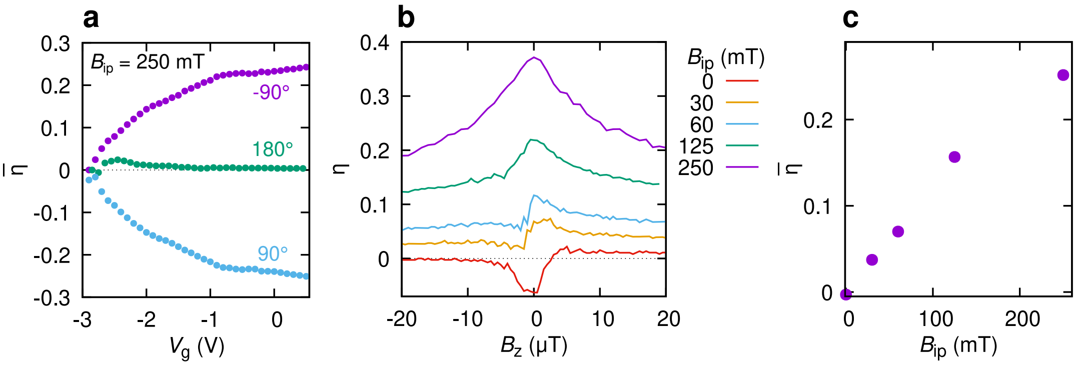

Fig. 4.10.: a, Average of η (labeled as $\bar{\eta}$) in the range $|B_z| < 20\,\mu\text{T}$ at $B_{\text{ip}} = 250\,\text{mT}$ as a function of gate voltage for different orientations of the in-plane magnetic field. **b,** Rectification efficiency $\eta(B_z)$ for $\theta = -90°$ and gate voltage $V_g = 0.5\,\text{V}$, for different values of B_{ip}. Thermal annealing is performed after each data point, eliminating any field-sweep dependence. **c,** $\bar{\eta}$ as a function of B_{ip}, extracted from the data shown in panel **b**.

the sinusoidal behavior $\bar{\eta} \sim -\sin(\theta)$. The temperature dependence of the

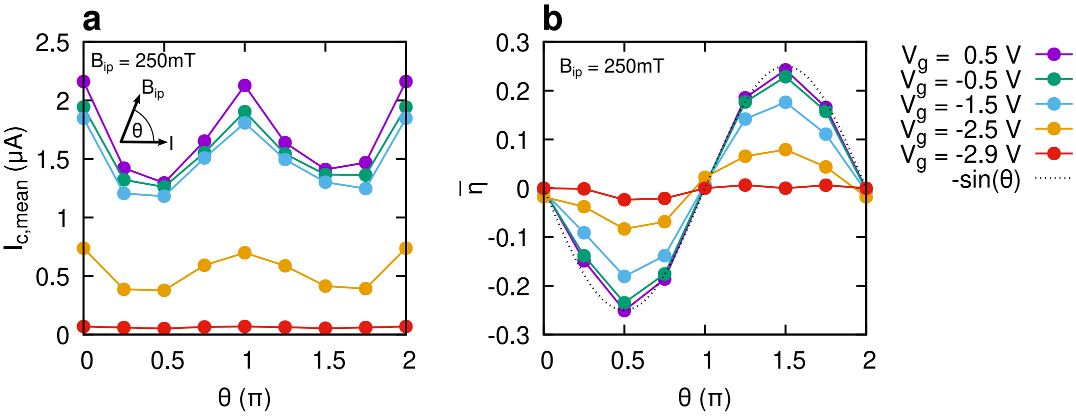

Fig. 4.11.: a, Angle dependence of the mean depinning current $1/2(I_c^+ + I_c^-)$ for $|B_{\text{ip}}| = 250\,\text{mT}$. The depinning current is averaged over the range $|B_z| < 20\,\mu\text{T}$. **b,** Angle dependence of the averaged diode efficiency $\bar{\eta}$.

critical current and the rectification efficiency is shown in Fig. 4.12 for the case of $B_{\text{ip}} = 250\,\text{mT}$. We find that the diode efficiency is nearly constant for temperatures up to 400 mK. A decrease of η is only observed at temperatures where the critical current is reduced to a small fraction of the value at zero temperature.

Changing the out-of-plane magnetic field B_z while keeping $T \ll T_c$ will result in a non-equilibrium configuration of vortices. When sweeping the out-of-plane field around zero, we expect that the depinning currents will display a hysteretic dependence on the out-of-plane magnetic field. Fig. 4.13 shows measurements of I_c, for both positive and negative sweep direction of B_z, performed around $B_z = 0\,\mu\text{T}$. The shape of $\eta(B_z)$ clearly depends on the sweep direction for B_z close to zero, while at a larger magnitude of B_z, the critical currents and diode efficiency become independent of the sweep direction. The observed dependence

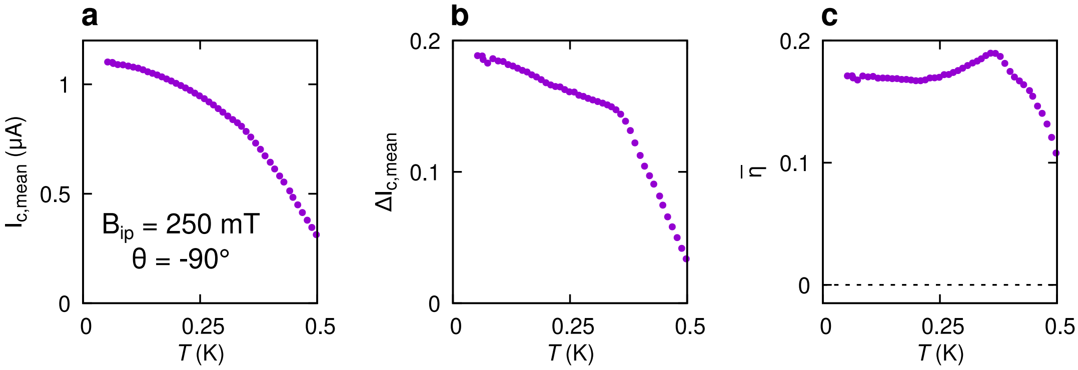

Fig. 4.12.: a, Temperature dependence of the mean critical current $(I_c^+ + |I_c^-|)/2$ for an in-plane field $B_{\text{ip}} = 250\,\text{mT}$ applied perpendicular to the bias current. **b**, Difference of critical currents $\Delta I_c = I_c^+ - |I_c^-|$ versus temperature. **c**, Rectification efficiency as a function of temperature. In this figure all quantities on the y-axis are averaged over the range $|B_z| < 20\,\mu\text{T}$).

on the sweep direction of B_z is actually not hysteretic but anti-hysteretic. One possible explanation for the anti-hysteresis is that it does not originate from vortex pinning in the array but from flux pinning in the aluminum electrodes. Trapped flux in the aluminum electrodes will generate stray fields with opposite direction of magnetic flux in the array. The result would be that hysteretic flux trapping in the electrodes leads to anti-hysteretic flux in the array.

Importantly, the effect of (anti-)hysteresis can be removed by thermal annealing after changing the value of B_z as is performed for the measurements shown in Fig. 4.10**b**. The annealing procedure results in much more symmetric $\eta(B_z)$ curves.

Measurements of the ratchet effect are also performed with device B in order to check the device-to-device reproducibility. The comparison of devices A and B, shown in Fig. 4.14, shows that both arrays have similar critical current and the rectification efficiency of both devices at $B_{\text{ip}} = 250\,\text{mT}$ is nearly identical.

4.5. A minimal model of the ratchet effect

The model and numerical simulations presented in this chapter were developed together with A. G. Penner, L. I. Glazman, and F. von Oppen (FU Berlin / Yale University). The basic model of the vortex ratchet effect is presented in Fig. 4.15. For a XY model with nearest-neighbor interactions only, a φ_0-shift is has no effect on the properties of vortices, as already discussed in the introduction of this chapter. This changes when adding next-nearest (diagonal) neighbor interactions. In general, the φ_0-shift induced by an in-plane field will be different for the nearest-neighbor and next-nearest-neighbor couplings. This results in a frustrated ground state with spontaneous persistent currents.

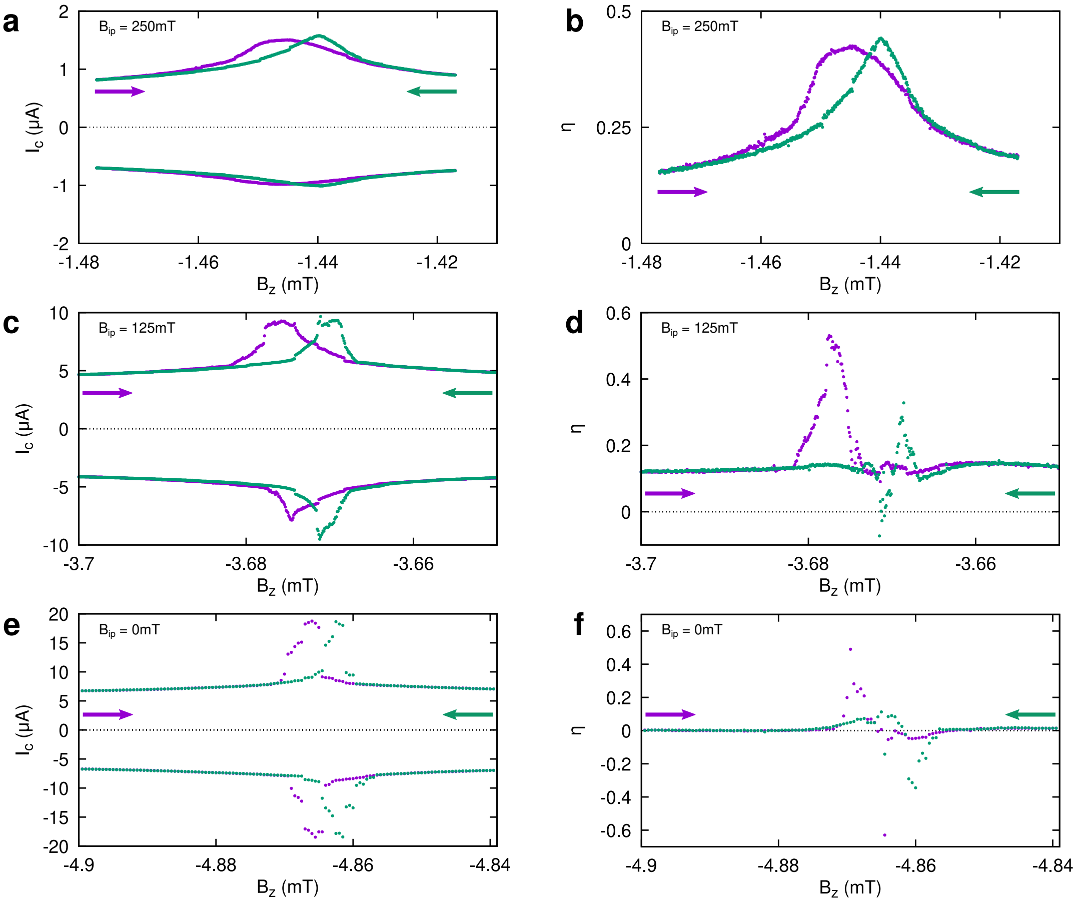

Fig. 4.13.: a, Out-of-plane field dependence of the depinning current I_c for $B_{\text{ip}} = 250\,\text{mT}$. **b,** Rectification efficiency corresponds to the depinning currents shown in panel **a**. **c,d,** Same measurement performed at $B_{\text{ip}} = 125\,\text{mT}$. **e,f,** Same measurement performed at $B_{\text{ip}} = 0\,\text{mT}$. The sweep direction of the out-of-plane field is indicated with purple/green arrows. In all measurements the in-plane magnetic field is applied in negative y-direction ($\theta = -\pi/2$) and the temperature is below 50 mK. No offsets are subtracted from B_z. The offset fields are caused by misalignment of the in-plane fields and flux-pinning in the superconducting magnet coils. In all other figures in this chapter an offset is subtracted from B_z. The offset field is determined as the field with maximum critical current.

When a vortex is added to the array, the current configuration is no longer four-fold symmetric around the vortex center. A sizable coupling between diagonal neighbors is realistic in the studied array. The range of the Josephson coupling in the proximitized electron gas is determined by the spatial extend of the Andreev bound states. The relevant length scale is given by the coherence length $\xi \sim \sqrt{\xi_0 l}$ with the BCS coherence length $\xi_0 = \frac{\hbar v_F}{\pi \Delta^*} > 800\,\text{nm}$ and the mean free path $l_e > 250\,\text{nm}$. The values of l_e and v_F in the electron gas strongly depend on the electron density (see Appendix A). For a large range of densities the order of magnitude of ξ is the same as the lattice constant $a = 500\,\text{nm}$ of the JJA. Unlike the Josephson diode effect, the vortex ratchet effect persists to large fields and temperatures. We conclude that higher harmonics in the CPR of the junctions are not required for the vortex ratchet effect. Therefore, the model only uses sinusoidal CPR with anomalous phase shifts.

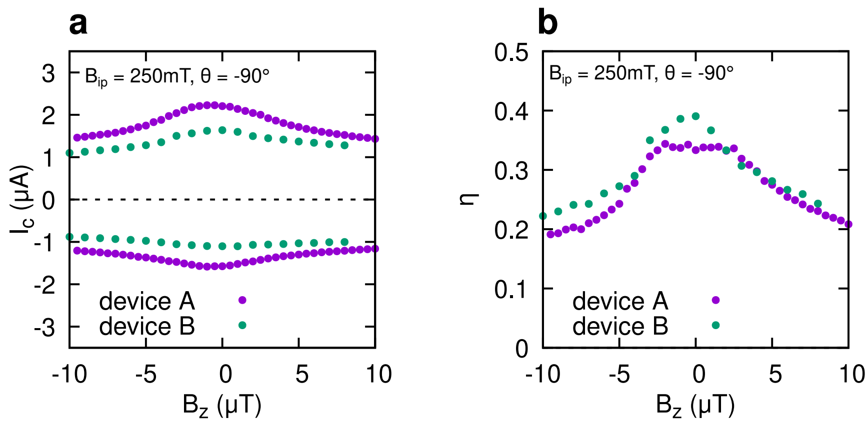

Fig. 4.14.: Comparison of depinning current (panel **a**) and diode efficiency (panel **b**) for the nominally identical devices A and B.

The free energy of an array with shape $N \times N$ is written as a function of the phases φ_{ij}, where $i = 1, \ldots, N$ and $j = 1, \ldots, N$ are the indices in x- and y-direction, respectively. The Josephson coupling between nearest neighbors is labeled E_J and the coupling between next-nearest (diagonal) neighbors is labeled E_D. We consider the case where the in-plane field is aligned in the y-direction and the out-of-plane field B_z is zero. All junctions in x-direction have the anomalous phase shift φ_0^x and the diagonal junctions have the phase shift φ_0^{diag}. The free energy at zero temperature reads

$$F_{\text{JJA}} = \sum_{ij} -E_J \cos(\varphi_{i+1,j} - \varphi_{i,j} - \varphi_0^x) + \sum_{ij} -E_J \cos(\varphi_{i,j+1} - \varphi_{i,j}) + \sum_{ij} -E_D \cos(\varphi_{i+1,j+1} - \varphi_{i,j} - \varphi_0^{\text{diag}}) + \sum_{ij} -E_D \cos(\varphi_{i+1,j-1} - \varphi_{i,j} - \varphi_0^{\text{diag}}). \tag{4.8}$$

A minimizer of the free energy is a configuration of phases φ_{ij} for which F_{JJA} has a minimum. A minimizer satisfies $\partial F_{\text{JJA}}/\partial \varphi_{ij} = 0$, which is equivalent to Kirchhoff's current law. In order to study the effect of a bias current, the following term is added to the free energy

$$F_{\text{bias}} = \frac{2e}{\hbar} I \sum_j (\varphi_{1,j} - \varphi_{N,j}). \tag{4.9}$$

Minimizing the free energy then results in a constant current density at the left and right edges of the array. The current density, i.e., the current per row will be given by I, so that the total bias current through the array will be NI.

For the case with zero bias current a minimizer of Eq. (4.8) is found from an ansatz with a helical modulation of the phase in x-direction: $\varphi_{ij}^{\text{GS}} = i\Delta\varphi_x$. Inserting this ansatz leads to the equation

$$\tan(\Delta\varphi_x) = \frac{E_J \sin(\Delta\varphi_0)}{E_J \cos(\Delta\varphi_0) + 2E_D} \tag{4.10}$$

$$\Delta\varphi_x = \text{arctan2}(E_J \sin(\Delta\varphi_0), E_J \cos(\Delta\varphi_0) + 2E_D) \tag{4.11}$$

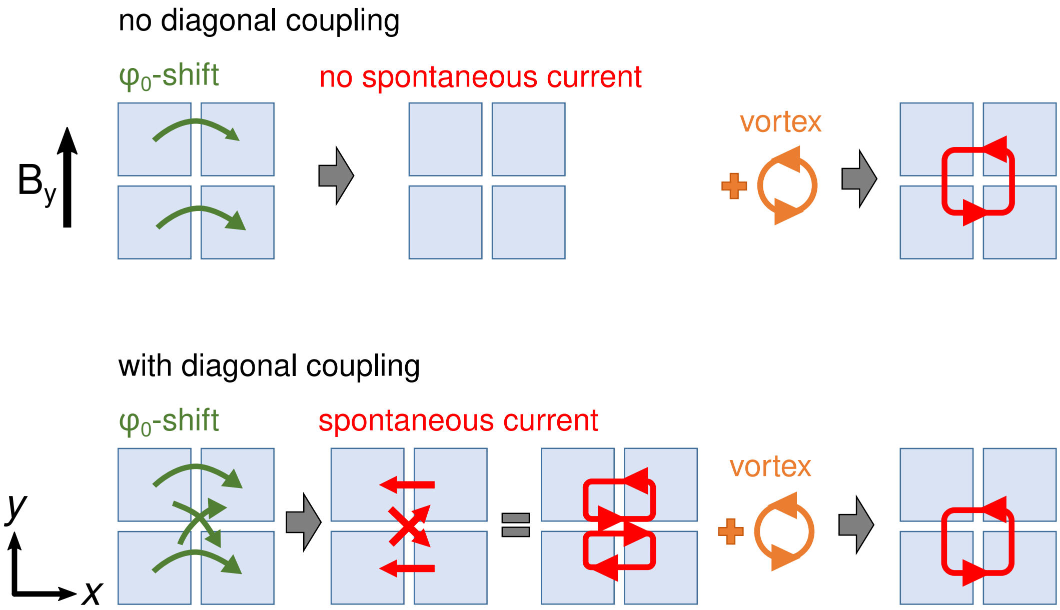

Fig. 4.15.: Top row: JJA with nearest neighbor coupling only, with no spontaneous supercurrent in the ground state. The Josephson current distribution around a vortex remains four-fold symmetric. **Bottom row:** Anomalous phase shifts $\varphi_0^x > \varphi_0^{\text{diag}}$ and persistent currents for the case with diagonal coupling. The Josephson current distribution generated by a vortex is no longer four-fold symmetric.

where $\Delta\varphi_0 := \varphi_0^x - \varphi_0^{\text{diag}}$ is the difference of anomalous phase shifts in the horizontal and the diagonal direction. This helical ground state features persistent currents. The current configuration for the parameters $E_D/E_J = 0.5$ and $\Delta\varphi_0 = \pi/2$ is shown in Fig. 4.16**a**.

We now study vortex depinning in the described model of the JJA. We set the frustration parameter f to zero and consider a single vortex in a large array. This corresponds to the experimental situation of the lowest possible vortex density at nominally zero out-of-plane field. Starting from the ground state φ_{ij}^{GS} an approximate ground state of the array which contains a single vortex at position (x, y) (measured in units of the lattice constant) is constructed using the "arctan" approximation

$$\varphi_{ij} = \varphi_{ij}^{\text{GS}} + \text{arctan2}(y - l, x - i). \tag{4.12}$$

The real ground state of the vortex, which is a local minimizer of the free energy, is then found by gradient descent of the free energy. The current configuration for the ground state of a single vortex with parameters $E_D/E_J = 0.5$ and $\Delta\varphi_0 = \pi/2$ is shown in Fig. 4.16**b**. The four-fold rotational symmetry of the Josephson currents around the center of the vortex is clearly broken.

The depinning current and rectification efficiency are determined as follows. We start with the ground state of a large $N \times N$ array with a single vortex located in the center. The bias current I is then increased in small steps. For each new value of I the free energy is minimized by gradient descent until the phase of each island converges. For a value of I below the depinning current the

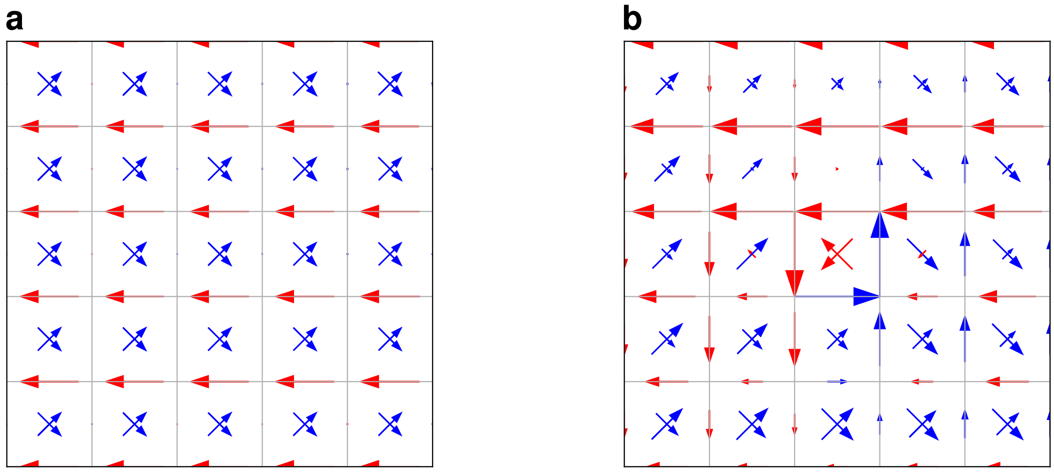

Fig. 4.16.: a, Josephson currents in the ground state of a JJA for $E_D/E_J = 0.5$ and $\Delta\varphi_0 = \pi/2$. **b,** Josephson currents around the center of a vortex for $E_D/E_J = 0.5$ and $\Delta\varphi_0 = \pi/2$. Figures provided by A. G. Penner.

vortex will remain pinned inside the array. This can be checked by evaluating the winding number of the phase around the center of the array. If the value of I exceeds the depinning current, the vortex will start to move towards the edge of the array. This procedure to find the depinning current is performed for both positive and negative polarity of the bias current for different values of the couplings E_D/E_J and the anomalous phase shift difference $\Delta\varphi_0 = \varphi_0^x - \varphi_0^{\text{diag}}$. The convergence of the critical currents with respect to the size N of the array is checked. An array size of 100×100 is found to be sufficiently large and the simulations presented here are performed with arrays of this size. Results of the simulations are presented in Fig. 4.17. For $E_D = 0$ no rectification is observed and the depinning current does not depend on $\Delta\varphi_0$. For $E_D/E_J > 0$ the rectification efficiency η shows a monotonic increase with $\Delta\varphi_0$ which is approximately linear for small values of $\Delta\varphi_0$. The rectification efficiency increases monotonically with the ratio E_D/E_J, reaching 20 % for the parameters $E_D/E_J = 0.8$, $\Delta\varphi_0 = \pi/2$.

The rectification efficiency observed in the experiment is symmetric with respect to the out-of-plane field, i.e., $\eta(B_z) = \eta(-B_z)$. This means that the depinning current is the same for vortices and antivortices. This observation can be explained in our model of the ratchet effect. A comparison of the Josephson current configurations for vortices and antivortices is sketched in Fig. 4.18. For B_{ip} applied in the y-direction, the shape of an antivortex is found from the shape of a vortex by the reflection $y \to -y$. In addition, the Lorentz force has opposite sign for vortice and antivortices. The depinning current for a given polarity of the bias is therefore the same for both vortices and antivortices.

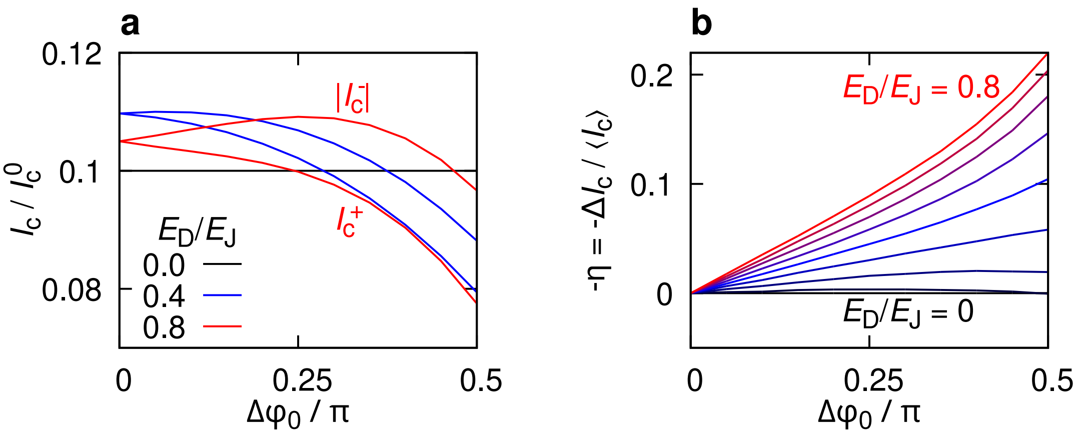

Fig. 4.17.: a, Simulated vortex depinning currents for positive and negative polarity of the bias current as a function of $\Delta\varphi_0 := \varphi_0^x - \varphi_0^{\mathrm{diag}}$. Different colors correspond to different values of the ratio E_D/E_J. **b,** Resulting rectification efficiency $\eta = \Delta I_c / I_{c,\mathrm{mean}}$ as a function of $\Delta\varphi_0$ for different values of the diagonal coupling strength. The ration E_D/E_J is changed in steps of 0.1 from 0 to 0.8. Simulation results provided by A. G. Penner.

4.6. The role of diagonal coupling for the vortex ratchet effect: A control experiment

In the used square array geometry the ratio of next-nearest and nearest-neighbor coupling depends on the length scales of the Andreev bound states and the array lattice constant.

The spatial extend of the ABS can be reduced by using a material with a low mean-free path l in the quantum well. For $l \ll \xi_0$ the effective GL-coherence length will scale as $\xi_{\mathrm{GL}} \sim \sqrt{l\xi_0}$. We now perform a control experiment with an array device with strongly reduced diagonal coupling. The device geometry is presented in Fig. 4.19**a,b**. This JJA, which will be further explored in Chapter 5, is fabricated using the Al/InAs heterostructure M10-08-18.2, also grown by the group of Prof. M. Manfra. The maximum mean free path in this structure is $l_{\mathrm{max}} \sim 270\,\mathrm{nm}$, observed at an electron density of $n = 0.5 \times 10^{12}\,\mathrm{cm}^{-2}$. The array with a shape of 16×2000 islands has a lattice constant of $a = 1.1\,\mu\mathrm{m}$. For comparison, the material used for devices A and B has $l_{\mathrm{max}} > 700\,\mathrm{nm}$. From the sample geometry and material parameters we conclude that device C has a very low ratio of diagonal coupling to nearest-neighbor coupling. From this we expect that the magnetochiral ratchet effect is strongly reduced in device C.

We perform $V(I)$ measurements on device C. The in-plane magnetic field with magnitude $B_{\mathrm{ip}} = 250\,\mathrm{mT}$ is applied perpendicular to the direction of the bias current. Fig. 4.19**c** shows a $V(I)$ measurement performed close to zero out-of-plane magnetic field. For both polarities the bias current is swept starting at $I = 0$. The curve is apparently symmetric, i.e. $V(I) = -V(-I)$. The curve does not show the pronounced step at the critical current, which is visible

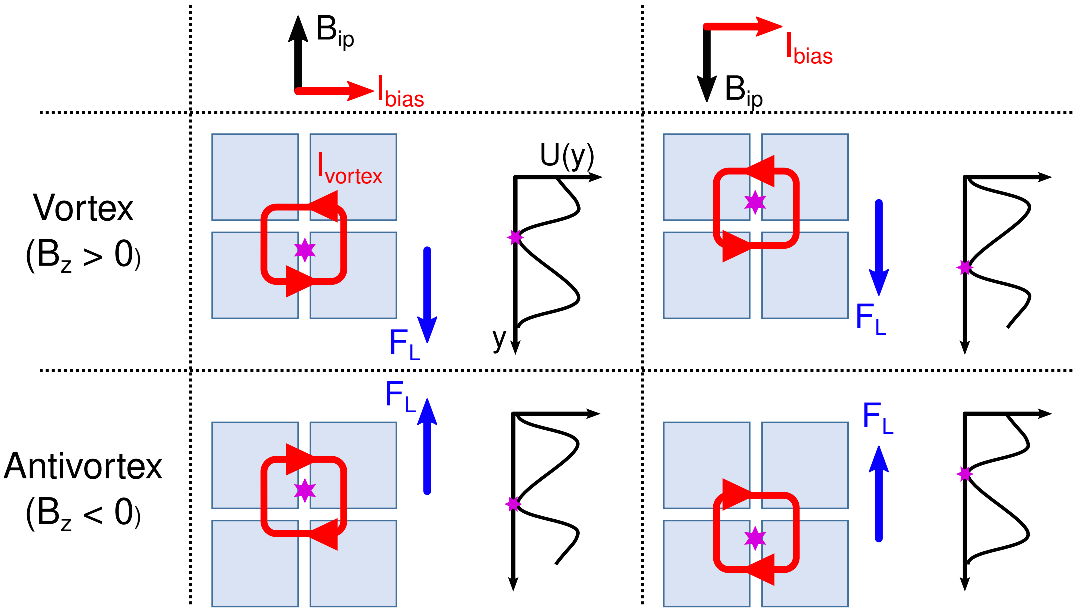

Fig. 4.18.: Qualitative shape of the currents and Lorenz forces for vortices (upper row) vs. antivortices (lower row). A linetrace of the skewed pinning potential $U(y)$ is sketched for each situation. The pink dots mark the minima of the pinning potentials. The columns differ by the polarity of the in-plane field ($\theta = -90°$ in the left column vs. $\theta = 90°$ in the right column), while the current bias direction is the same. For a given polarity of B_{ip} the sign of rectification efficiency is the same for vortices and antivortices, while changing the polarity of B_{ip} flips the sign of the rectification efficiency. The left column corresponds to the situation of lower depinning current, the right column that for higher depinning current.

in measurements of devices A and B. Instead, there is a continuous onset of voltage. Still it is possible to define a critical current as the current where the voltage exceeds a threshold value. The resulting $I_c(B_z)$ curves for different values of the threshold voltage V_c are shown in Fig. 4.19**d**. Similar to devices A and B a maximum of I_c is found around zero out-of-plane field. The rectification is shown Fig. 4.19**d**. For low values of V_c the value of η is affected by large noise, while at the larger value $V_c = 5\,\text{mV}$ the rectification efficiency is less noisy and always below 0.01. Compared to devices A and B where $\eta \gtrsim 0.35$ for the same parameters this clearly shows that the ratchet effect is strongly suppressed in device C.

The same measurement is also performed at $B_{\text{ip}} = 150\,\text{mT}$. The resulting data is presented in Fig. 4.20. For low values of V_c we again observe a low rectification efficiency with large noise. At higher voltage $V_c = 10\,\text{mV}$ we find a more sizable rectification $\eta \sim 0.07$. The rectification is observed in a resistive regime where a power of $P = I \cdot V \sim 40\,\text{nW}$ is dissipated in the long array device. A power of this magnitude will typically increase the electron temperature in the device by several hundred mK. In this case the observed non-reciprocal resistance could be related to non-reciprocal paraconductivity. This type of magnetochiral effect was observed in gated MoS_2 [54]. While the effect exists also in the normal state, it is strongly enhanced in a regime of temperature slightly above the critical

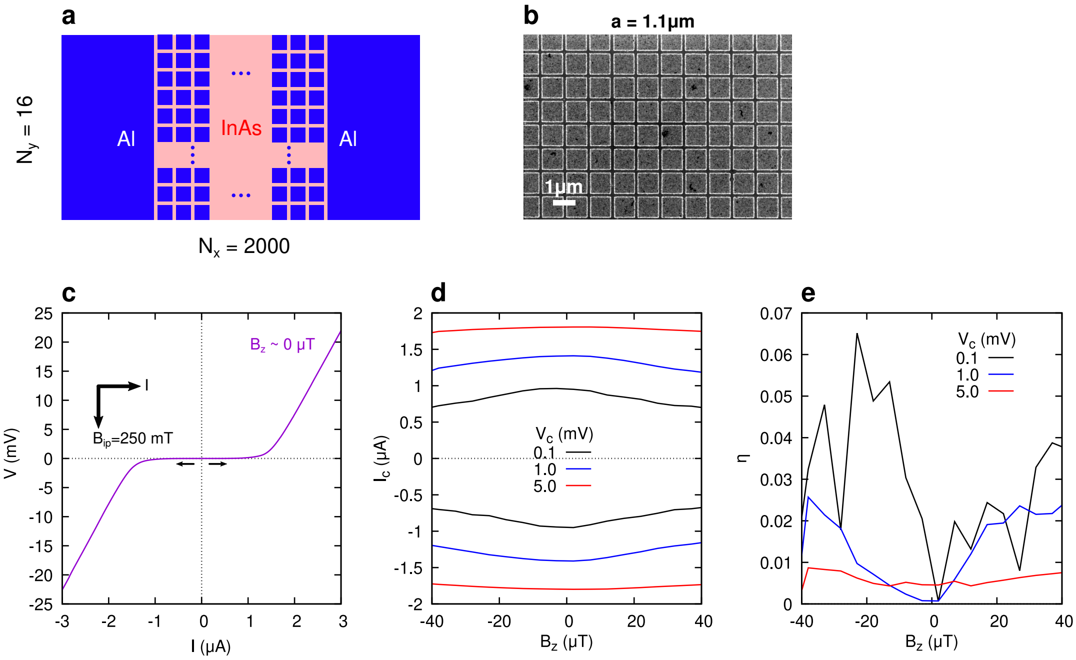

Fig. 4.19.: a, Geometry of The JJA device C. Fabrication of this device and SEM imaging was performed by Christian Baumgartner. The Array consists of 16 $\times$ 2000 islands with two superconducting aluminum contacts. Transport experiments are performed using a quasi four-point configuration. Due to manufacturing reasons the array is actually formed by 20 shorter arrays of size 16 $\times$ 100. The individual arrays are connected by superconducting Al electrodes. **b,** SEM image of device C. The aluminum islands of size 1 $\times$ 1µm^2 are separated by junctions of length $\sim$ 100 nm. The lattice constant is $a = 1.1\,\mu\text{m}$. **c,** $V(I)$ characteristic of device C obtained at $B_{\text{ip}} = 250\,\text{mT}$. The out-of-plane field is close to $0\,\mu\text{T}$ and the gate voltage is set to $V_g = 0\,\text{V}$. The sweep direction for positive and negative polarity of the bias current is indicated with black arrows. **d,** Critical current as a function of B_z for different values of the voltage V_c (see text). **e,** Rectification efficiency corresponding to the critical currents shown in panel **d**.

temperature where the resistance is influenced by superconducting fluctuations [55].

4.7. The ratchet effect at commensurate frustration

So far we have studied the vortex ratchet effect at small values of the out-of-plane field $|B_z| < 20\,\mu\text{T}$, corresponding to a frustration $|f| < 0.0024$. At higher vortex densities the interaction of vortices will start to play a larger role. We now study the role of frustration on the vortex ratchet effect. The rectification properties are measured in a larger range of frustration up to the first integer matching field.

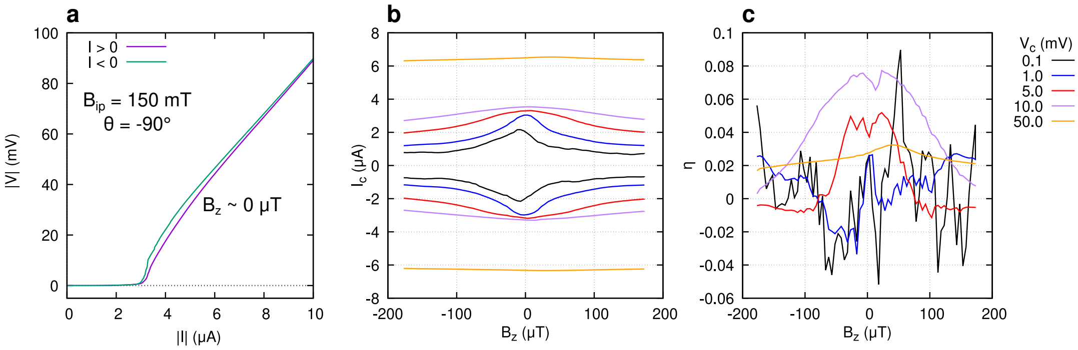

Fig. 4.20.: a, Measurement of $V(I)$ for device C at $B_{\text{ip}} = 150\,\text{mT}$ at zero out-of-plane field. The in-plane field is applied perpendicular to the bias current. **b,** Critical current as a function of out-of-plane field. Different colors relate to different values of the voltage V_c which is used for the definition of the critical current. **c,** Diode efficiency corresponding to the $I_c(B_z)$ data shown in panel **b**. The gate voltage is set to $V_g = 0\,\text{V}$ and the temperature is below 100 mK.

The non-reciprocal behavior is detected using a low-frequency measurement of the second-harmonic of resistance. Using a digital lock-in amplifier we apply an ac current bias with frequency ω and amplitude I_{ac}. The dc component of the bias current is zero. The measurement technique is illustrated in Fig. 4.21. A non-reciprocal $V(I)$ characteristic results an a second-harmonic component of the voltage when the amplitude of the ac bias is between the positive and negative critical currents. This can also be shown by expanding $V(I)$ in a Taylor series. For a non-reciprocal $V(I)$ curve the expansion contains even powers of I. In the most simple case, the expansion is given by $V(I) = \alpha I + \beta I^2$. For an ac-drive $I(t) = I_{\text{ac}} \sin(\omega t)$, the resulting voltage over the sample is

$$V(t) = \alpha I_{\text{ac}} \sin(\omega t) + \beta I_{\text{ac}}^2 \frac{1}{2}(1 - \cos(2\omega t)). \tag{4.13}$$

The second order term in $V(I)$ results in a dc and a second harmonic component. Both components are proportional to the second power of the excitation current I_{ac}. The non-reciprocal response can be detected by measuring the dc component and/or the second harmonic component of the voltage. The lock-in detection at frequency $2\omega/(2\pi) = 2 \times 777.77\,\text{Hz}$ can be performed with much better signal to noise ratio, when compared to a measurement of dc voltage. Therefore, we use the second harmonic of resistance to study non-reciprocal $V(I)$ characteristics.

A color map of the first harmonic of resistance $R_\omega = V_\omega / I_{\text{ac}}$ as a function of frustration f and amplitude I_{ac} is shown in Fig. 4.22. The in-plane field with orientation perpendicular to the bias current is set to $B_{\text{ip}} = 125\,\text{mT}$. The resistance is zero for a amplitude below the critical current (black regions). Similar to the differential resistance measurement presented in Fig. 4.7, maxima of the depinning current are visible at the commensurate values of frustration $f = \pm 1/3, \pm 1/2, \pm 2/3, \pm 1$. The in-plane field leads to a reduction of critical current and compared to Fig. 4.7, fewer peaks of the critical current are visible.

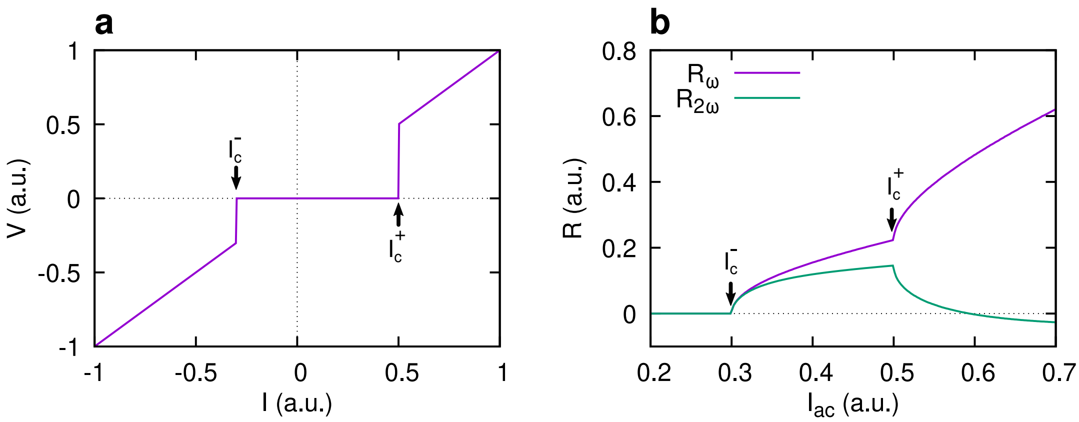

Fig. 4.21.: **a**, Non-reciprocal $I(V)$ characteristic with $\eta = \Delta I_\mathrm{c}/I_\mathrm{c,mean} = 0.5$. **b**, Numerically calculated first and second harmonic of resistance for an ac current bias with amplitude I_ac.

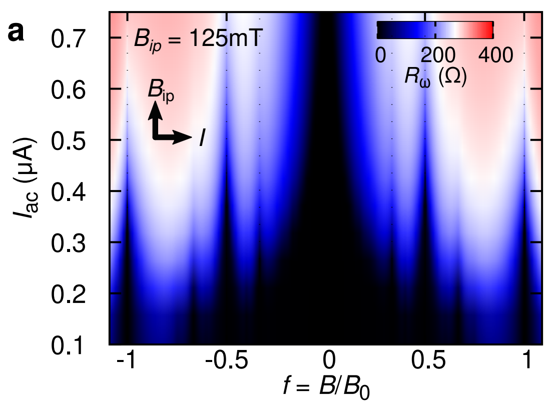

Fig. 4.22.: Map of the first harmonic of resistance $R_\omega = V_\omega/I_{ac}$ measured as a function of frustration for $B_\mathrm{ip} = 125\,\mathrm{mT}$. The y-axis corresponds to the rms-amplitude of the ac current bias. The measurement is performed using the SR830 digital lock-in amplifier with the SR552 voltage preamplifier. The frequency is set to $\omega/2\pi = 777.77\,\mathrm{Hz}$.

Color maps of the second harmonic of resistance $R_{2\omega} = V_{2\omega}/I_\mathrm{ac}$ are shown in Fig. 4.23 for different orientations of the in-plane field. Peaks of $R_{2\omega}$ with the same sign are visible at integer values of f, as well as at $f = 1/2$ (blue color in panel **a** and red color in panel **b**). Close to $f = 0$ the bias amplitude is always below the critical current so that $R_{2\omega}$ is zero (white region). A reversed sign of $R_{2\omega}$ is found in the region $0.2 < f < 0.5$ with a pronounced peak at $f = 1/3$ (red color in panel **a** and blue color in panel **b**). Line-traces of $R_\omega(f)$ and $R_{2\omega}(f)$ are shown in Fig. 4.24**a-c**. The sign reversal of $R_{2\omega}$ around $f = 1/3$ is reproduced in a measurement at lower in plane field $B_\mathrm{ip} = 60\,\mathrm{mT}$, shown in Fig. 4.24**d,e**.

We now compare the observed vortex ratchet effect to that reported in previous experiments, where the ratchet effect was always engineered by fabrication of a pinning potential with asymmetric geometry. For example in [56] the pinning sites were created using ferromagnetic dots below a layer of aluminum. The

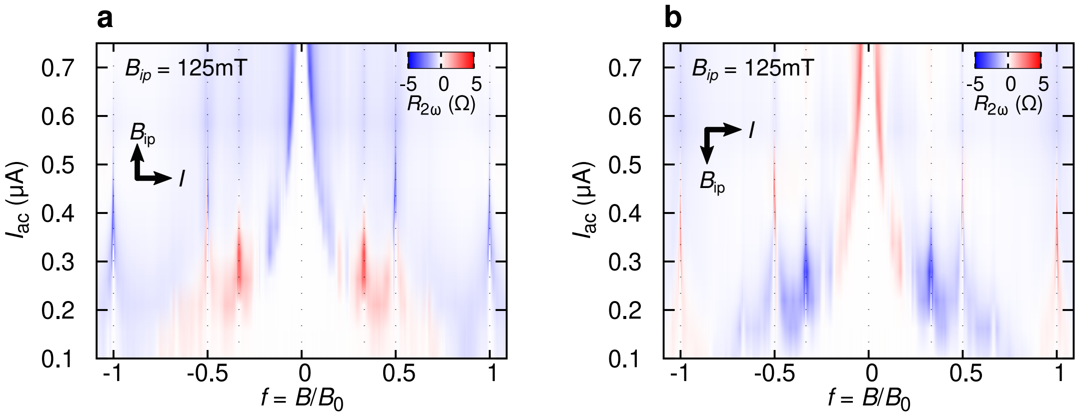

Fig. 4.23.: Second harmonic of resistance $R_{2\omega} = V_{2\omega}/I_{ac}$ measured as a function of frustration and ac bias current. The in-plane field $B_{\mathrm{ip}} = 125$ mT is applied perpendicular to the direction of current. The angle between current and in-plane field is $\theta = 90°$ for panel **a** and $-90°$ for panel **b**.

non-reciprocal pinning was created by sawtooth-like modulation of the ferromagnetic dot size. A similar approach was used in [57] were pinning was studied in an array of superconducting Pb islands fabricated on a Cu film. The ratchet effect was created by a sawtooth-like modulation of the junction lengths. In contrast, the array studied in the present work has four-fold rotational symmetry and an in-plane magnetic field is used to control the non-reciprocal vortex pinning which is a *magnetochiral effect*. Another qualitative difference is the dependence on the out-of-plane field. In the previous works the rectification has an anti-symmetric dependence on the out-of-plane field, i.e, $\eta(B_z) = -\eta(-B_z)$. This is because the geometrically engineered pinning potential is the same for vortices and antivortices, while the Lorentz force has different sign for vortices and antivortices. In contrast, for the magnetochiral effect the pinning is different for vortices and antivortices, resulting in a rectification efficiency which is symmetric as a function of the out-of-plane field.

The sign reversal of the vortex ratchet as a function of frustration was also observed in several previous works with geometrically engineered ratchet potentials [57, 58, 59, 60, 56, 61]. In [56] it was shown that the sign reversal is linked to vortex-vortex interaction. It occurs when the effective magnetic penetration depth, which sets the length scale of vortex-vortex interaction, exceeds the period of the sawtooth modulation. However, in our case the physics is clearly different as the sign reversal occurs in a symmetric and periodic array. The observation of an enhanced ratchet effect at commensurate values of the frustration parameter is a novel effect. The exact microscopic mechanism leading to the sign reversal in our measurements is so far not clear. Likely, the critical currents close to commensurate values of frustration is determined by the pinning of defects in the vortex patterns such as missing (or excess) vortices.

More insights in the motion of vortices could be gained by also measuring the Hall voltage, providing the full vortex resistivity tensor, as proposed by

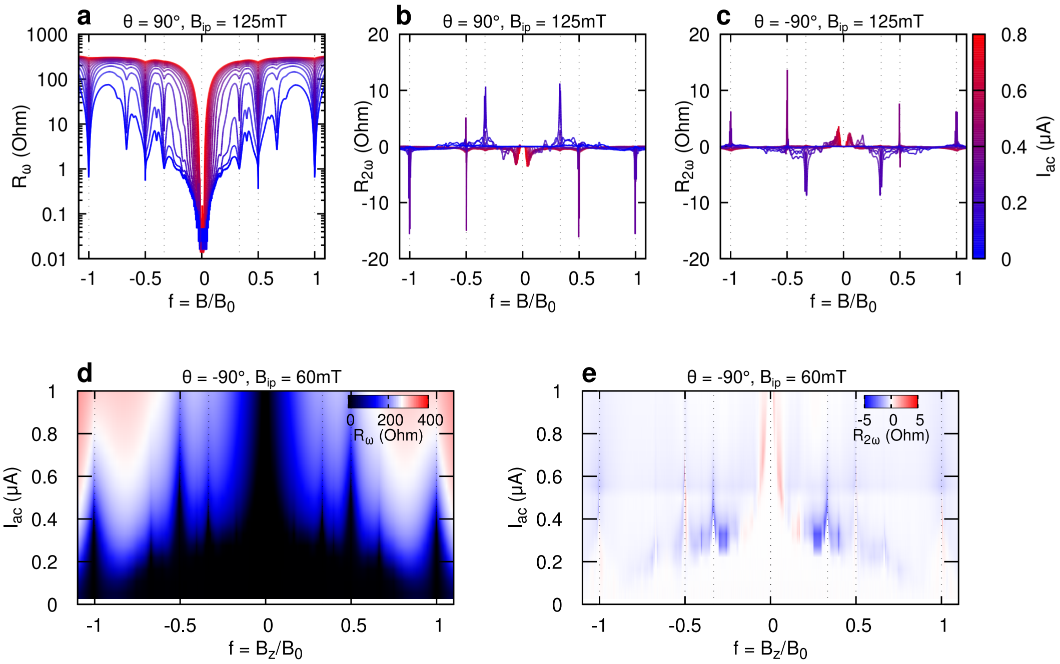

Fig. 4.24.: a-c, Line traces of $R_\omega(f)$ and $R_{2\omega}(f)$ corresponding to the color maps shown in Fig. 4.22 and Fig. 4.23. **d,e,** Measurement of R_ω and $R_{2\omega}$ performed at $B_{\text{ip}} = 60\,\text{mT}$.

Penner *et al.* [62]. The longitudinal voltage measured in the present device is proportional to the rate of vortices moving in the direction transverse to the applied bias current. Using additional Hall probes, located at the top and bottom edges of the array, it would be possible to detect vortex motion in the longitudinal direction, which is predicted to occur for frustrations around $f = 1/3$ where the vortices form stripe-like patterns [62].

5. Measurement of Josephson vortex inductance in two-dimensional Josephson junction arrays

In this chapter we study the inductive response of pinned vortices in two-dimensional Josephson junction arrays (JJAs). The inductance is measured using a MHz-frequency LC resonator circuit. Compared to the measurement of the vortex depinning current, this technique provides a complementary probe of vortex pinning far below the depinning current, deeply in the dissipation-free superconducting regime. Another motivation for the measurement of Josephson vortex inductance comes from our earlier experiment on vortex inductance in Al/InAs films [63]. There it was found that the in-plane magnetic field induces an anisotropic pinning potential, which was detected using vortex inductance measurements.

5.1. Inductance of Josephson vortices

For a sufficiently low density of vortices the pinning potential of a vortex is given by

$$U(x, y) = E_B(2 - \cos(2\pi x/a) - \cos(2\pi y/a))$$

where a is the lattice constant of the array and E_B is the energy barrier. For square arrays E_B is 10 % of the Josephson energy E_J [64]. For small deflection from the minimum, the pinning potential is parabolic with the spring constant given by $k = \frac{4\pi^2 E_B}{a^2}$. When applying a dc bias current to the JJA, the vortex experiences the Lorentz force

$$F = j\Phi_0,$$

where j is the applied current density. As a function of j the pinning energy is given by

$$U(j) = \frac{F^2}{2k} = \frac{\Phi_0^2 j^2}{2k}.$$

The two-dimensional density of vortices in an out-of-plane magnetic field B_z is $n_v = B_z/\Phi_0$. The vortex pinning energy per area is then given by

$$e(j) = U(j) \cdot n_v = \frac{\Phi_0 B_z j^2}{2k} = \frac{1}{2} L_\square j^2$$

with the sheet inductance

$$L_\square(B_z) = \frac{\Phi_0 B_z}{k} = \frac{\Phi_0^2}{4\pi^2 E_B} f.$$

The frustration parameter $f = \frac{B_z a^2}{\Phi_0}$ gives the flux per plaquette in units of the superconducting flux quantum. Expressing the Josephson energy using the Josephson inductance L_0, we find

$$L_\square(B_z) = \frac{\Phi_0^2}{4\pi^2 E_B} f = L_0 \frac{E_J}{E_B} f$$

At zero frustration without vortices in the array, the inductance is given by the Josephson inductance L_0 of the junctions. The total inductance close to zero field is the sum of the Josephson inductance and the vortex inductance

$$L_{\text{total}\square}(f) = L_0 \left(1 + \frac{E_J}{E_B} f\right). \tag{5.1}$$

The above formulas are only valid as long as the out-of-plane field B_z is sufficiently low, so that the distance between vortices is large and vortex-vortex interaction plays no role. Moreover, we have assumed that B_z is low enough so that it does not influence the Josephson energy E_J and the barrier energy E_B.

5.2. Device layout and basic characterization

The sample is fabricated from the wafer M10-08-18.2 grown by the Manfra group. The active layer of the heterostructure is shown in Fig. 5.1**a**. The structure is slightly different compared to more recently grown wafer stack used for the experiments described in previous chapters. A detailed characterization of this wafer is performed in [37]. The peak mobility is $\mu = 22\,000\,\mathrm{cm^2/Vs}$ at a density $n = 5 \times 10^{11}\,\mathrm{cm^{-2}}$ and the maximum mean free path at this density is $l_e = 270\,\mathrm{nm}$. The 2D array device used for measurements of vortex inductance was fabricated by C. Baumgartner. In order to generate a large inductance, the device features a chain of 20 blocks connected in series, as shown in Fig. 5.1**b**. Each block is 16 islands wide and 100 islands long. The effective number of sheets in the array is given by $N_\square = 20 \times 100/16 = 125$. The lattice constant is $a = 1.1\,\mathrm{\mu m}$ and the expected matching field is $B_0 = \Phi_0/a^2 = 1.71\,\mathrm{mT}$.

Fig. 5.2**a** shows a measurement of the differential resistance as a function of out-of-plane magnetic field and dc bias current. The observed behavior is similar

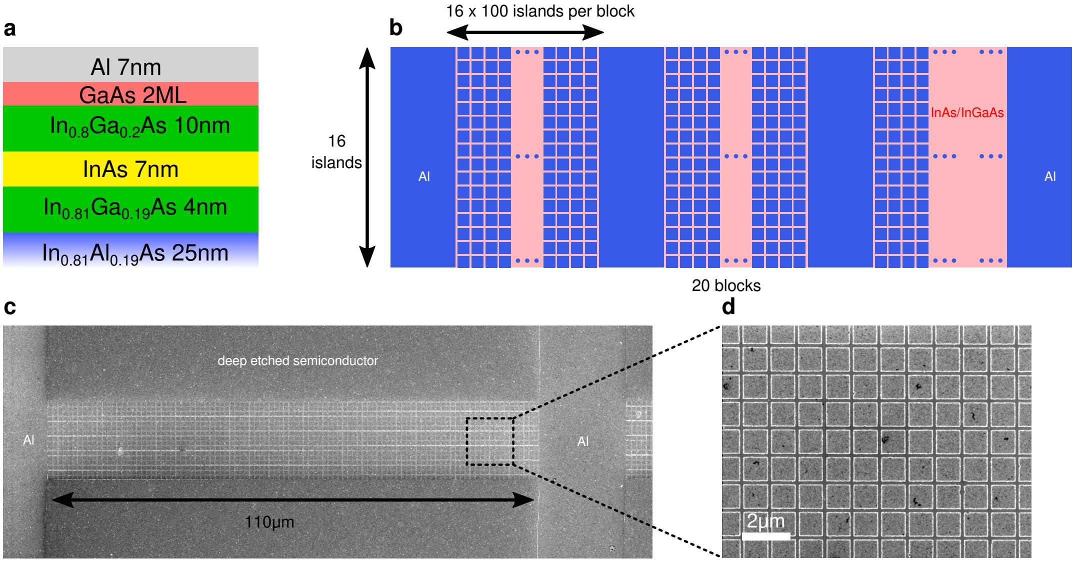

Fig. 5.1.: **a**, schematic of the 2D JJA device used for inductance measurements. The array consists of 20 blocks, which are 16 islands wide and 100 islands long. The lattice constant of the array is 1.1 µm and the junctions have a length of $\sim 100\,\mathrm{nm}$. **b**, SEM image of a single block with 100×16 islands. **c**, Zoom into panel **b** showing SEM image of individual islands. Fabrication and SEM imaging of the device was performed by C. Baumgartner.

to the device with $a = 500\,\mathrm{nm}$ studied in the previous chapter. Fig. 5.2**b** shows multiple maxima of the critical current at various integer and fractional values of the frustration parameter $f = B_z/B_0$. Compared to the 200×200 array with $a = 500\,\mathrm{nm}$ we observe fewer peaks at commensurate values of the frustration parameter. The sheet resistance in the normal state, observed at high bias current, is given by $R_N/N_\square \sim 80\,\Omega$. Close to zero out-of-plane field we observe a discontinuous $V(I)$ curve, as shown in Fig. 5.3. Unlike the device studied in the previous chapter we observe multiple jumps in the voltage. We count ~ 20 jumps, matching with the number of blocks in the device. We conclude that the vortex depinning current differs between the blocks in the device. Even before the first step at $I \sim 5.5\,\mu\mathrm{A}$ there is a onset of voltage, which becomes visible in the log scale plot Fig. 5.3. In nominally zero field we observe non-zero voltage for $I \gtrsim 1.5\,\mu\mathrm{A}$. This differs from the device studied in the previous chapter where no voltage could be found before the voltage jump. A possible reason for the early onset of voltage are weak spots in the long array. At a weak spot the vortex pinning could be strongly reduced and vortex creep would be possible before the depinning current is reached in the other parts of the array.

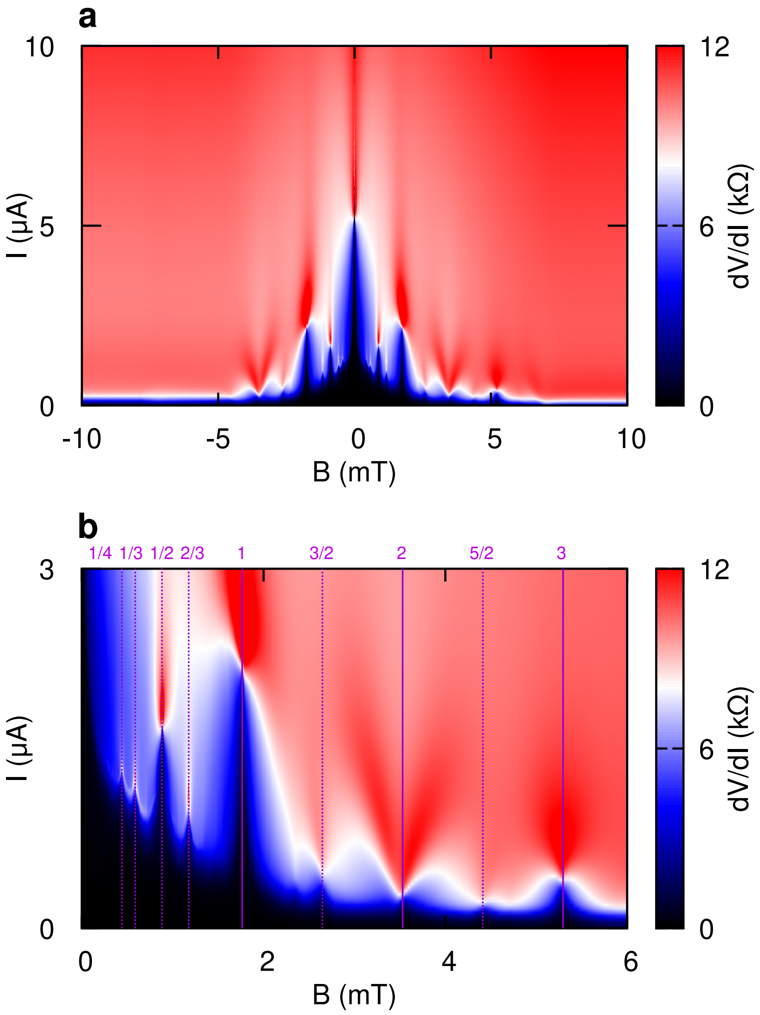

Fig. 5.2.: **a** dV/dI is obtained by numerical differentiation of $V(I)$ curves. **b** Vertical lines are drawn at multiples and fractions of the matching field $B_0 = 1.765\,\mathrm{mT}$.

5.3. Measurement of Josephson and vortex inductance

As shown above, the inductance of the sample at zero applied bias current is directly related to the vortex density and the strength of the vortex pinning. Therefore, the measurement of inductance as a function of out-of-plane field is a direct probe of the vortex pinning in the array. Inductance measurements are performed by embedding the device in a cold LC resonator as shown in Fig. 5.4. A detailed description of the implementation of this technique is given in Appendix B.2. Fig. 5.4**b** shows the transmission spectrum measured at base temperature and zero out-of-plane magnetic field. The curves are fitted using

$$|S_{21}(\omega)| = \left| \frac{A}{1 + iQ_L(\frac{\omega^2-\omega_0^2}{\omega\omega_0})} \right| \tag{5.2}$$

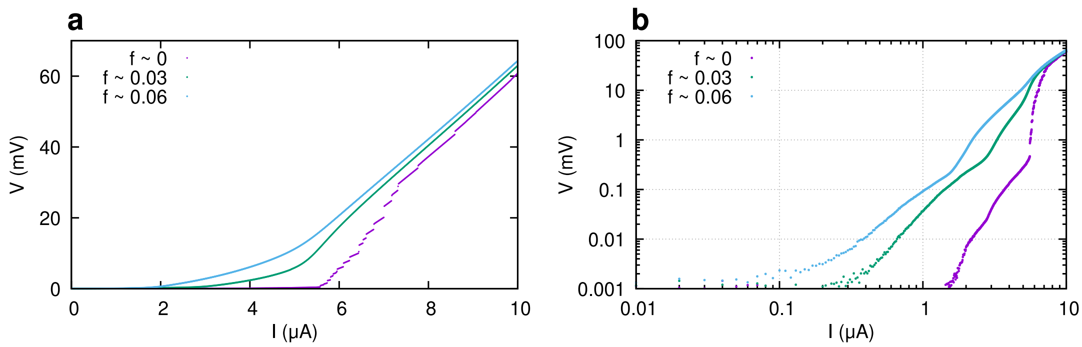

Fig. 5.3.: **a** $V(I)$ curves at low out-of-plane magnetic field. **b** Same data as **a** shown in double logarithmic scale.

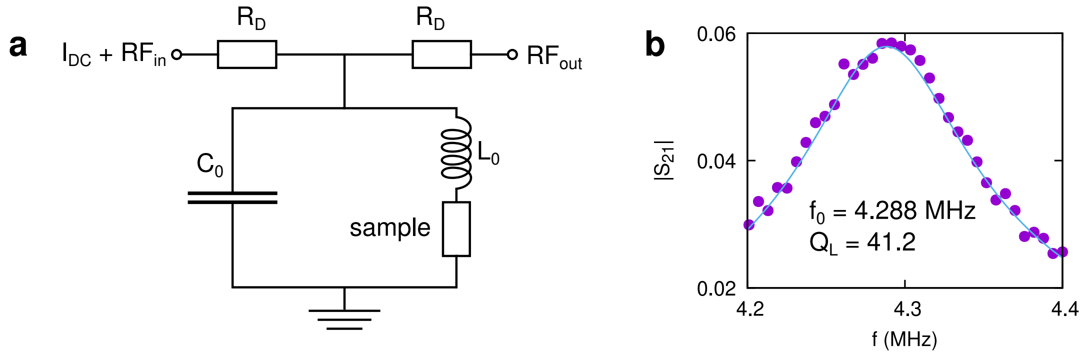

Fig. 5.4.: **a** Schematic of the resonator circuit. **b** Measurement of the S_{21} transmission parameter at zero magnetic field and base temperature. The fit is done with Eq. (5.2).

with the loaded quality factor Q_L, and the resonance frequency ω_0. The network analysis of the circuit is given in Appendix C. The inductance of the sample is directly related to the resonance frequency by

$$\omega_0 = \frac{1}{\sqrt{C_0(L_0 + L_{\text{sample}})}}$$

The loaded quality factor Q_L is related to the internal quality factor Q_I and the external quality factor Q_E

$$\frac{1}{Q_L} = \frac{1}{Q_I} + \frac{1}{Q_E}. \tag{5.3}$$

For the resonator circuit shown in Fig. 5.4**a** the external and internal quality factors are given by

$$Q_E = \frac{R_D + Z_0}{2}\sqrt{\frac{C}{L}} \sim 50 \tag{5.4}$$

$$Q_I = \frac{1}{R}\sqrt{\frac{L}{C}}. \tag{5.5}$$

The value of the coil inductance L_0 is determined in a separate cooldown where the sample is replaced by bond wires.

The resistance R which determines the internal quality factor is due to the series resistance of the capacitor, the copper coil, and the sample. At base temperature and zero magnetic field where the sample is deeply in the superconducting state we measure $Q_L = 41.2$. Using Eq. (5.3) we find Q_I from Q_L and Q_E, which gives $Q_I \sim 200$ corresponding to a resistance $R \sim 40\,\mathrm{m}\Omega$. This residual resistance is likely caused by the normal conducting parts of the circuit, such as the copper coil, the capacitor, and the pogo pins.

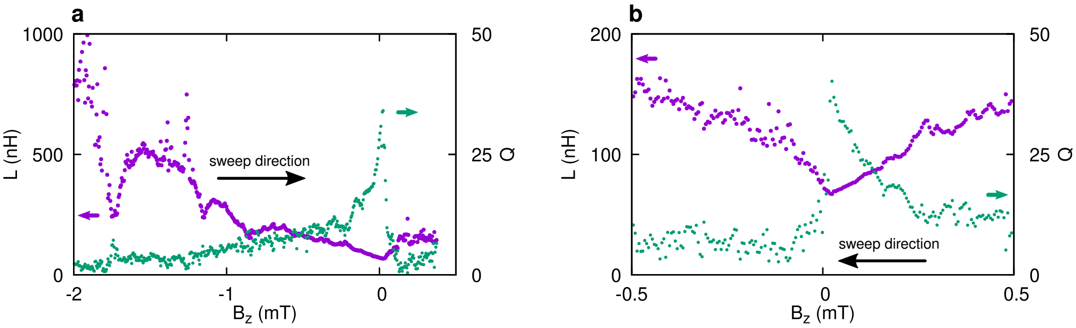

Fig. 5.5.: a b

We now study the behavior of the sample inductance L and the quality factor Q_L as a function of the out-of-plane magnetic field. The field is swept while the temperature is close to the base temperature of the cryostat. Fig. 5.5 shows the resulting $L(B_z)$ and $Q_l(B_z)$ curves. The results are very sensitive to the sweep direction of the field. As the field is swept towards zero, the quality factor increases with a sharp maximum around zero field. After the the magnetic field changes sign the quality factor is strongly reduced, leading to strong noise in the obtained inductance data. Apparently, the history of the magnetic field strongly influences the obtained measurements. By ramping the field we induce energetically unfavorable configurations of vortices in the JJA device and the superconducting leads. This problem is solved by thermal annealing of the vortex configuration for each value of B_z. After each change of B_z we use the heater located on the PCB of the resonator to apply a 1 mW heat pulse for 5 s. By measuring the resistance of the device we find that this heat pulse is sufficient to heat the JJA above the critical temperature of the aluminum film. The heat pulse is followed by a cooling time of 3 min. After the cooling time the temperature at the sample thermometer is below 200 mK and the transmission measurement is performed. The resulting data is shown in Fig. 5.6. The inductance and quality factor in Fig. 5.6**a** are clearly symmetric with respect to B_z, showing that the hysteresis problem is solved by the thermal annealing procedure. Around zero field we find a nearly constant increase of $L(B_z)$ with a sharp maximum of the quality factor at zero field. Apart from the V-shaped minimum of $L(B_z)$ at zero field we find additional minima of $L(B_z)$ at the values $f = 1/6$, $1/4$, $1/2$, $1/3$, and 1. With the most pronounced features at $f = 2/3$ and $f = 1$. For each of these commensurate values of frustration we find a pronounced peak in the measured quality factor. Around zero field we perform a fit of $L(B_z)$ as shown in Fig. 5.6**a** using

$$L(B_z) = L(B_z = 0)(1 + \alpha|f|). \tag{5.6}$$

The fit yields $\alpha \sim 6$, showing that vortex pinning is stronger than expected for a square array of junctions with sinusoidal CPR, for which one would expect $\alpha = E_J/E_B = 10$, as shown above. Similar to $f = 0$ one can extract the pinning of excess vortices around a commensurate value f_c of the frustration where $L(f)$ shows a dip

$$L(f - f_c) = L(f_c)(1 + \alpha_{f=f_c}|f - f_c|). \tag{5.7}$$

Fig. 5.6**b** shows the fits for $f = 2/3$ and $f = 1$. We find $\alpha_{f=2/3} \sim 21$ and $\alpha_{f=1} = 27$. From the larger values of α at the fractional frustration we conclude that pinning of the excess vortices and antivortices is much weaker compared to the pinning of vortices close to zero frustration.

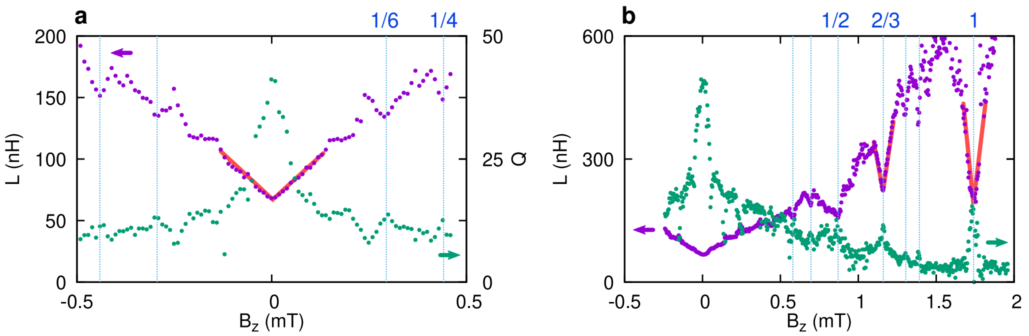

Fig. 5.6.: a Measured sample inductance (purple) and quality factor (green). Vertical lines are draws at $f = \pm 1/6$ and $f = \pm 1/4$. **b** vertical lines are drawn at $f = 1/3$, $2/5$, $1/2$, $2/3$, $3/4$, $4/5$, and 1.

5.4. Non-reciprocal Vortex inductance for in-plane magnetic fields

Applying a bias current density j will tilt the vortex pinning potential $U(y)$ to $\tilde{U}(y) = U(y) - \Phi_0\, j\, y$. Measuring the vortex inductance will probe the curvature of the pinning potential around the new energy minimum y_0 which is determined from the equation $U'(y_0) = \Phi_0 j$. A measurement of $L(I_{DC})$ will therefore probe the shape of the pinning potential. The vortex inductance will diverge as the bias current approaches the depinning current. For a ratchet-like pinning potential we expect to find a non-reciprocal behavior of $L(I_{DC})$. Applying an in-plane field of 150 mT we observe non-reciprocal $V(I)$ curves as shown in Fig. 5.7**b**. The sign of the effect is the same as for the device shown in the previous chapter, while the magnitude is much smaller. A more detailed discussion was given in the previous chapter in Section 4.6.

As a reference for the non-reciprocal $L(I_{DC})$ behavior, we first perform a measurement of $L(I_{DC})$ at zero in-plane magnetic field. In order to tune the out-plane field to zero we use the following procedure. The sample is heated close

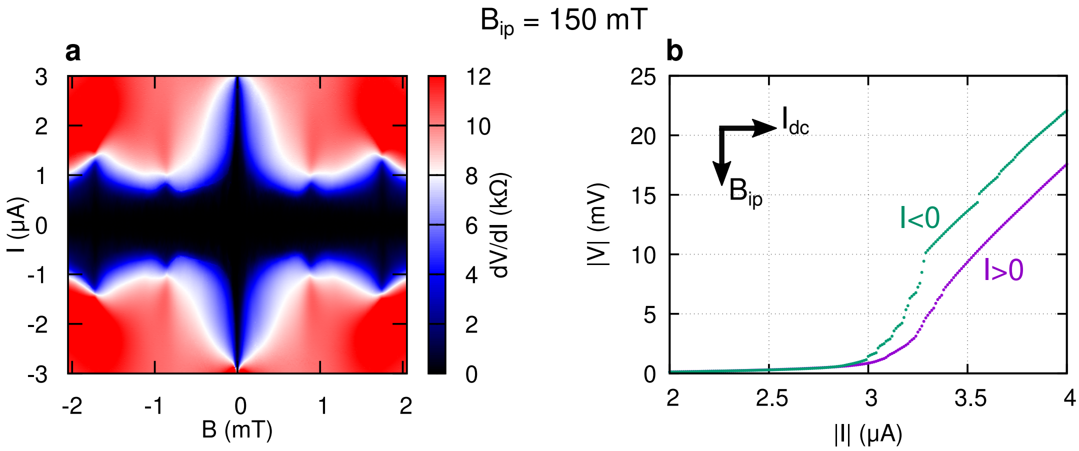

Fig. 5.7.: a Differential resistance $dV/dI(I_{DC}, B_z)$ measured at $B_{ip} = 150\,\mathrm{mT}$ applied perpendicular to the direction of the bias current. **b** $I(V)$ characteristic for positive and negative polarity of bias current at zero out-of-plane magnetic field. In both measurements the temperature is below 100 mK.

to the transition temperature and we measure $R(B_z)$ in a small range of field, which has a minimum at zero out-of-plane field. We then increase the temperature above the transition temperature of the aluminum film and cool at zero field. This procedure is repeated a few times in order to assert that the minimum of $R(B_z)$ is stable over time.

Fig. 5.8 shows the resulting data for $L(I_{DC})$ and $Q(I_{DC})$. The quality factor is nearly constant for $|I_{DC}| < 1.5\,\mu\mathrm{A}$ and shows a rapid decrease for larger magnitude of the current. The inductance shows a slight increase with applied bias current until the noise of the inductance measurement becomes large as the quality factor of the resonance is suppressed at $I_{DC} \sim \pm 2\,\mu\mathrm{A}$. We note that the quality factor is suppressed at currents much below the vortex depinning current $I_c \sim 5.5\,\mu\mathrm{A}$ found from the $V(I)$ measurements presented above. This can be linked to the spurious onset of voltage at low biases, which was also observed in the dc measurements.

We now study $L(I_{DC})$ with an in-plane magnetic field which is applied in the y-direction (perpendicular to the direction of the bias current). Before each measurement the sample is field-cooled in zero out-of-plane field as described above. In Fig. 5.9 we show the resulting $L(I)$ and $Q(I)$ curves for $B_{\mathrm{ip}} = 150\,\mathrm{mT}$ and $B_{\mathrm{ip}} = 250\,\mathrm{mT}$. The $L(I)$ and $Q(I)$ curves measured at $B_{\mathrm{ip}} = 150\,\mathrm{mT}$ is highly asymmetric in the bias current. Both $L(I)$ and $Q(I)$ are approximately symmetric around a positive bias $I_{\mathrm{offset}} > 0$. For positive polarity of the bias current we can apply up to $1.2\,\mu\mathrm{A}$ before the resonance vanishes, while in the negative direction we can apply only $0.5\,\mu\mathrm{A}$. Compared to zero in-plane field the maximum quality factor is reduced from 40 to 25, which shows an increase of dissipation due to weakly pinned vortices. At $B_{\mathrm{ip}} = 250\,\mathrm{mT}$ the asymmetry of $L(I)$ and $Q(I)$ is visible but less pronounced. The maximum possible bias current is reduced to $\sim 400\,\mathrm{nA}$ and the quality factor is always below 20 and is immediately reduced by the bias current. In Fig. D.1 we show further measurements at in-plane fields of 275 mT, 300 mT, and 350 mT showing a further decrease of quality factor and maximum possible bias current for which a resonance can be measured. At 350 mT the quality factor is always below 10 and the maximum possible bias current is below 100 nA. Decreasing the excitation power of the transmission measurement does not improve these numbers.

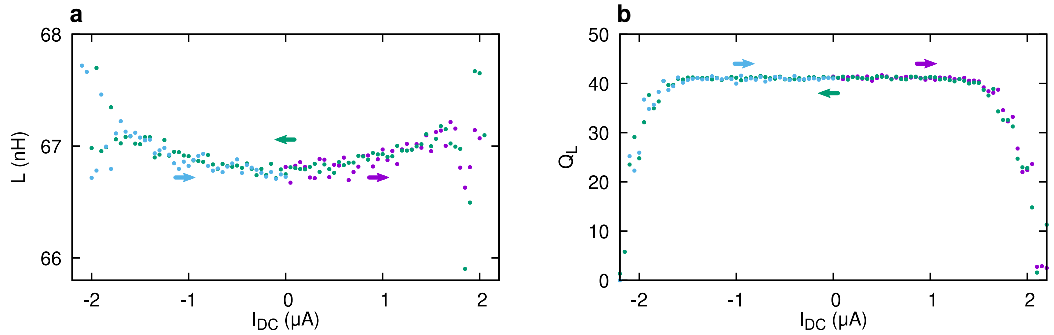

Fig. 5.8.: inductance and quality factor a function of dc bias current for zero in-plane magnetic field. The excitation power is −95 dBm and the temperature is below 120 mK.

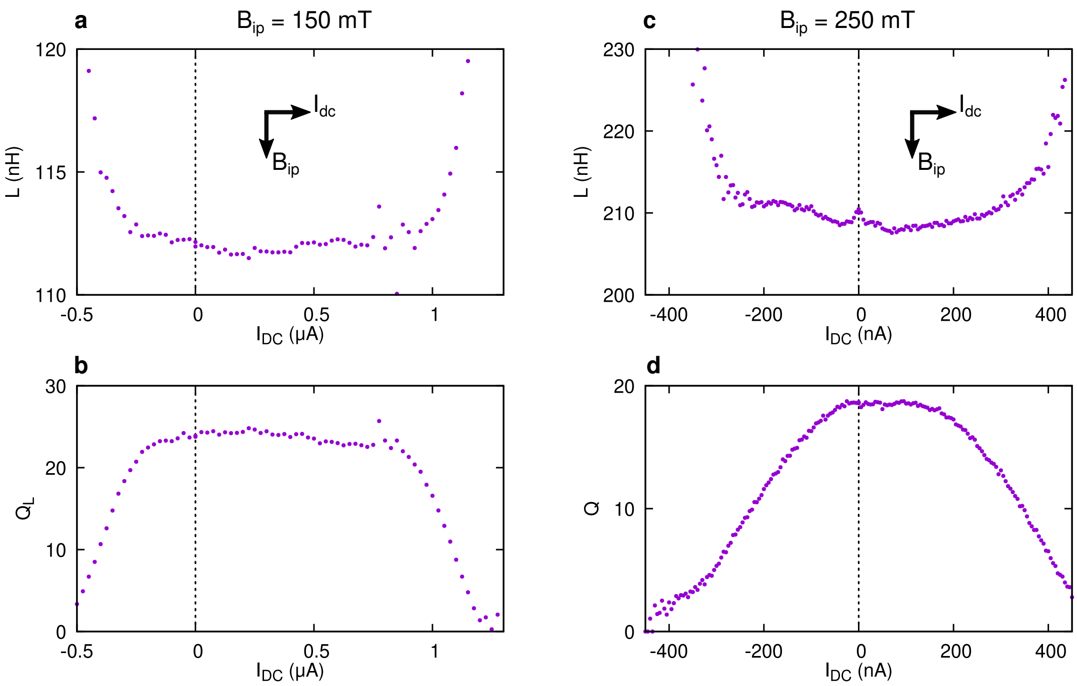

Fig. 5.9.: inductance and quality factor a function of dc bias current for $B_{\mathrm{ip}} = 150\,\mathrm{mT}$ and 250 mT. The in-plane field is applied perpendicular to the dc bias current at an angle $\theta = -90°$ as indicated. The excitation power is −95 dBm and the temperature is below 120 mK.

5.5. Discussion and Outlook

In this chapter we have demonstrated the first measurements of vortex inductance as a function of out-of-plane field B_z and bias current. Thermal annealing of the vortex configurations was found to be critical for the quality of the measurements. With an in-plane magnetic field we found non-reciprocal $L(I)$ curves, which is in good agreement with a ratchet-like vortex pinning potential and the observation of non-reciprocal depinning currents in the previous chapter. Another interesting measurement would be the dependence of $L(I)$ on the angle of the in-plane magnetic field with respect to the direction of the ac/dc bias currents. The theory in the previous paper predicts an increase of pinning strength for parallel orientation of field and current. According to the results found in the previous chapter the non-reciprocal behavior of $L(I)$ should monotonously increase with the magnitude of the applied in-plane field, as the effect is caused by the anomalous phase shift φ_0 in the junctions. We were not able to observe this here, which is likely due to the limitations of the device, as we will discuss next.

One issue with the studied device is the early onset of dissipation under current bias. Therefore only a small range of bias current is available before the Q factor of the transmission resonances is depressed. Better results could be possible by measuring the inductance of an array with only a single or a few squares. The inductance of a single square JJA would be about 100 times lower compared to the device studied in this chapter. However, it would be possible to boost the sensitivity of the measurement by
i) Use of a higher frequency resonator with lower L_0. As shown in Appendix C, the sensitivity of the inductance measurement is inversely proportional to the total inductance $L_0 + L_{\mathrm{sample}}$. We have already demonstrated resonators where the total inductance is a factor of 10 lower compared to the LC Resonator used here.
ii) Use of a cryogenic low noise amplifier. The cold amplifier which is now installed in the system (it was not available at the time of these measurements) has at least 10 times lower input voltage noise compared to a room temperature amplifier.

iii) Use of hanger-type resonators. As shown in Appendix C these resonators can have better sensitivity for inductance measurements for large quality factors compared to the resistively coupled resonators used here.

6. Coulomb blockade effects and superconductor-insulator transition in 2D JJAs

We now use the top gate on the two-dimensional Josephson junction array to tune it across the superconductor insulator transition (SIT). First we show the transition from the superconducting to the insulating state by studying the non-linear resistance $dV/dI(I_{bias})$. Tuning deeper into the insulating state, transport is blocked by the Coulomb gap. In the Coulomb blockade regime charge transport is suppressed when the bias voltage is below the *threshold voltage*, which is strongly tunable with the gate voltage. Finally we study thermal activation of transport in the deeply insulating regime, from which we find a novel technique of extracting the induced superconducting gap in the proximitized semiconductor quantum well.

6.1. Introduction to insulating behavior in JJAs

For a metallic island coupled by a capacitance C to its environment the single electron charging energy is given by $E_C = \frac{e^2}{2C}$. For simplicity we first consider the case of normal conducting islands. The discharging time for an electron on the island is given by $\tau = RC$. The lifetime broadening of the single electron energy levels is therefore given by $\Delta E \sim \hbar/\tau = \hbar/RC$. The single electron charging effects become relevant when the charging energy is larger than the lifetime broadening. From this condition we find that the resistance R must exceed the resistance quantum

$$R_Q = \frac{h}{e^2} = 25.8\,\mathrm{k}\Omega.$$

For an array of superconducting islands coupled by Josephson junctions, the most basic Hamiltonian is given by

$$\hat{H} = \frac{1}{2}\sum_{i,j}(\hat{Q}_i - q_i)C_{ij}^{-1}(\hat{Q}_j - q_j) - E_J\sum_{i,j}\cos(\hat{\varphi}_i - \hat{\varphi}_j - A_{ij}). \tag{6.1}$$

C_{ij}^{-1} are the entries of the inverse capacitance matrix. Rhe potential on each island is determined by the charge configuration: $V_i = \sum_j C_{ij}^{-1}Q_j$. The offset charges q_i are caused by gate voltages or charge defects. The charge and phase operators are canonically conjugated operators and satisfy the Heisenberg relation $[\hat{\varphi}_i, \hat{Q}_j] = 2ie\delta_{ij}$.

For $E_J \gg E_C$ the array is in the superconducting state with a well defined phase on each island and delocalized charges. In the other limit, $E_J \ll E_C$, the charges are localized, meaning that there is a well defined number of Cooper pairs on each island. The phase operators have large fluctuations around their expectation values and there is no global phase coherence. As the charges are localized, charge transport is blocked and the array is in the insulating state. At $E_J \sim E_C$ this model predicts a sharp superconductor-insulator transition (SIT) at zero temperature, which is an example of a continuous quantum phase transition. For a detailed discussion of the SIT in JJAs see e.g. [65, 66].

The model discussed above only considers the case where all charges are bound into Cooper pairs, meaning that there is an even number of electrons on each island. Adding a single electron to an island generates an excited quasi-particle state with energy Δ. As we will discuss below, the quasi-particle states are fundamental for the understanding of our experiments. Another feature of the junction physics, which is not captured by Eq. (6.1), is dissipation in the junctions due to shunt resistance and quasi-particle tunneling. The influence of the dissipation on the properties of single Josephson junctions is discussed in many recent works. The original theoretical predictions of Schmid and Bulgadaev predict a crossover in junction behavior for a shunt resistance $R = R_Q/4 = h/4e^2 = 6.5\,\mathrm{k\Omega}$, separating superconducting behavior for $R < R_Q/4$ and a regime with a resistance peak near zero bias current and low dissipation at larger bias currents for $R > R_Q/4$ [67, 68]. This model is controversially discussed in multiple recent experimental and theoretical works, e.g. [69, 70, 71, 72], and no consensus on the nature of the dissipative transition seems to be found so far. The Schmid-Bulgadaev transition is very difficult to measure in single Josephson junctions as the resistance of the junction is shunted by the lead impedance which is typically much smaller than $R_Q/4$ at the relevant frequency regime of the junction dynamics. For the case of two-dimensional arrays of Josephson junctions the role of dissipation is even less clear.

In the measured JJA device each aluminum island is coupled to the gate with the geometric capacitance C_g and to each neighboring island with capacitance C, see Fig. 6.1**c**. The electric field created by a single charge on an island decreases exponentially for a separation larger than the screening length $\lambda = \sqrt{C/C_g}$ (in units of the lattice constant) [73]. Therefore, the screening length sets the range for charge-charge interactions. A schematic of the 2D JJAs device is shown in Fig. 6.1**a**. The global top gate is used to deplete the electron gas in the junctions. Each island is capacitively coupled to the environment as shown in Fig. 6.1**c**. The geometric capacitance C_g between an island and the top gate can be estimated as

$$C_g = \epsilon\epsilon_0 A/d = 0.16 \text{ fF} \tag{6.2}$$

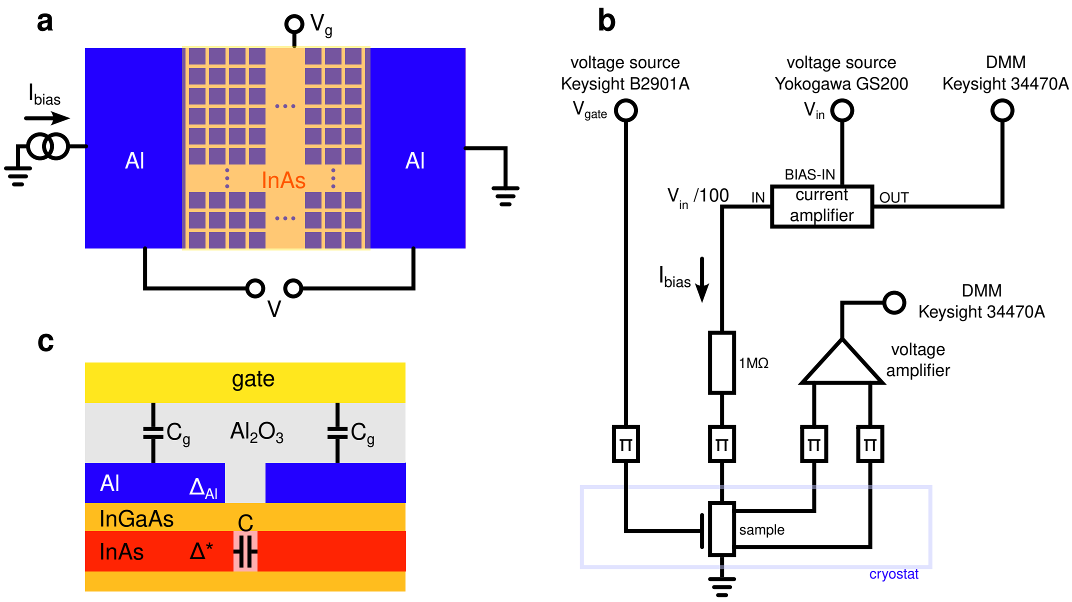

Fig. 6.1.: **a**, 2D JJA device of 200 × 200 aluminum islands. The size of the islands is 400 × 400 nm and the lattice constant is $a = 500$ nm. The same device was used for the measurements presented in Chapter 4. **b**, Measurement setup used to study insulating behavior of the JJA. The current amplifier Femto DDPCA-S is used to bias the device. The voltage is measured using the Femto DLPVA-100-F differential voltage amplifier. **c**, Side-view of the JJA device. C_g is the geometric capacitance between the aluminum islands and the top gate electrode. C is the inter-island junction capacitance.

where $A = (400\text{ nm})^2$ is the area of the islands, $d = 70$ nm is the thickness of the dielectric, and $\epsilon = 8$ is the dielectric constant of the ALD grown aluminum oxide [74]. The capacitance C between neighboring aluminum islands is difficult to estimate and will in general depend on the applied gate voltage, which tunes the potential in the tunneling barrier between neighboring islands.

6.2. Nonlinear resistance and threshold voltage

Fig. 6.2**a** shows differential resistance $dV/dI(I)$ for gate voltages between -3.1 V and -3.3 V. We find a transition from superconducting to insulating behavior with a sharp crossover at the critical gate voltage $V_c = -3.17$ V, indicated with a star in Fig. 6.2**b**. For $V_g > V_c$ we find superconducting behavior with a dip in differential resistance at zero bias current, which evolves into the zero resistance state for $V_g \sim -3.1$ V. For $V_g < V_c$ the $dV/dI(I)$ curves feature a bump at zero bias current. Up to $V_g = -3.22$ V the dip is surrounded by a region of decreased resistance, i.e. as the bias current approaches zero, the resistance first decreases before increasing close to zero bias current. We note that the behavior is never ohmic, i.e. none of the measured curves shows a constant value of $dV/dI(I)$.

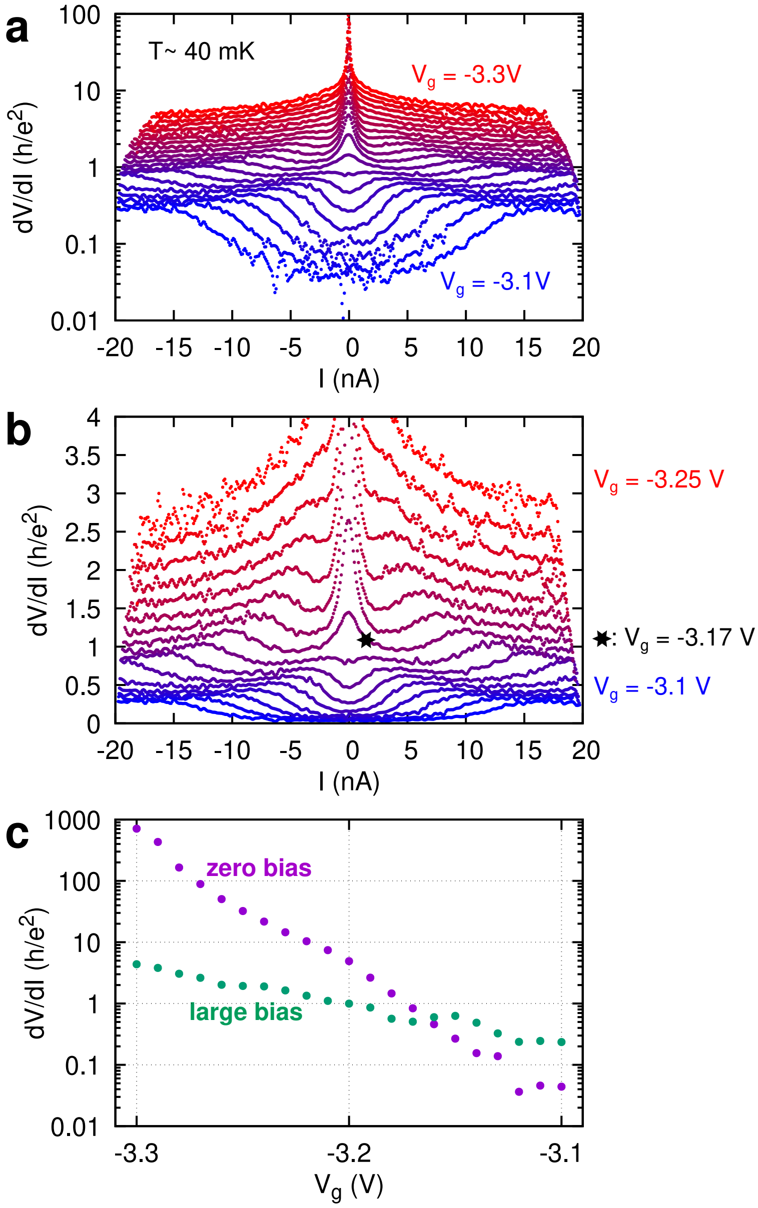

Fig. 6.2.: a, Differential resistance $dV/dI(I)$ for $-3.4\,\mathrm{V} < V_g < -3.1\,\mathrm{V}$ in steps of 0.01 V. The data is obtained by numerical differentiation of $V(I)$ curves. Measurements are performed at $T \approx 40$ mK in zero magnetic field. **b,** same $dV/dI(I)$ data as in **a**, with differential resistance plotted in linear scale. The sharp crossover at $V_g = -3.17\,\mathrm{V}$ (indicated with a black star) from a dip to a bump at zero bias current is clearly visible. **c,** Differential resistance as a function of gate voltage extracted from the data shown in panels **a,b**. Differential resistance at zero current bias is shown in purple, while the resistance at high current bias $I > 15\,\mathrm{nA}$ is plotted in green.

The resistance as a function of gate voltage is shown in Fig. 6.2**c** for zero bias current (purple) and the highest measured bias current $I \sim 15\,\mathrm{nA}$ (green). Both quantities show an exponential dependence on the gate voltage.

We now study $I(V)$ curves in the insulating regime for gate voltages $V_g < -3.4$ V. In Fig. 6.3**a,b** we compare the cases of superconducting and normal islands. The islands are driven to the normal state by an out-of-plane magnetic field of 200 mT. In both cases we observe that no current is detected for bias voltages smaller than a threshold voltage V_T. The peak-to-peak noise of the measured current in this insulating regime is ~ 300 fA. The threshold voltages are slightly different for positive and negative bias. This is not surprising, as the bias is applied asymmetrically, as sketched in Fig. 6.3**d**. One terminal of the array is at ground potential, so that the bias voltage affects the effective gate voltage.

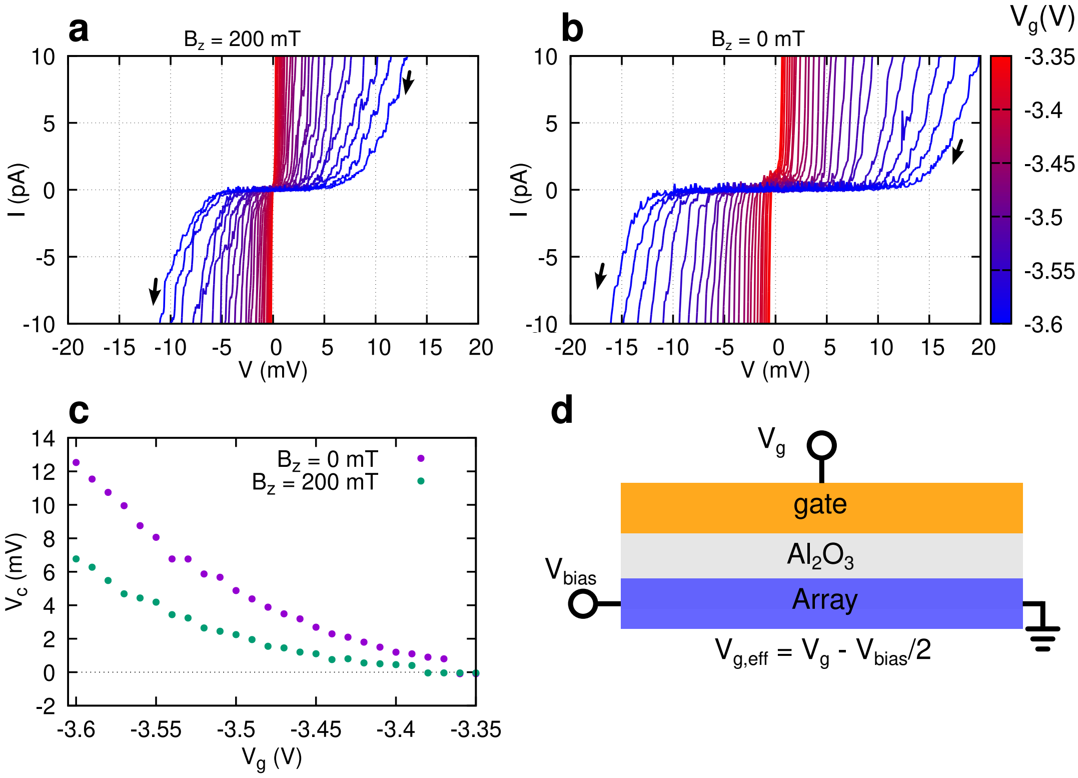

Fig. 6.3.: a,b, $I(V)$ in the insulating regime for normal islands at $B_z = 200$ mT (panel **a**) and superconducting islands at $B_z = 0$ mT (panel **b**). The gate voltage is changed from $V_g = -3.6$ V (blue) to $V_g = -3.35$ V (red). The temperature is $T \approx 40mK$. The sweep direction of the current bias is indicated with black arrows. **c,** Threshold voltage V_T as a function of gate voltage extracted from the measurements shown in panels **a** and **b**. The critical voltage is defined by $|I(V_c)| < 1$ pA. **d,** Schematic of measurement setup with asymmetric biasing. The bias voltage V_{bias} is applied at the left terminal of the array and the right terminal is connected to ground. In this configuration the effective gate voltage depends on the applied bias voltage.

For the non-superconducting case there are analytical expressions for V_T which depend on the ratio of C/C_g [73, 75]. In our system we expect to have a random offset charge on each island due to charge defects in the semiconductor and dielectric. In the limit $C_g \gg C$ the expected threshold voltage is [73]

$$V_T = 0.338 \frac{eN}{C_g}. \tag{6.3}$$

Inserting $C_g = 0.16\,\mathrm{fF}$ and $N = 200$ gives $V_T = 67\,\mathrm{mV}$. Experimentally we observe a much smaller value $V_T \leq 7\,\mathrm{mV}$, showing that the device cannot be in the limit where $C_g \gg C$.

For the other limit $C \gg C_g$ the threshold voltage was computed numerically in [75] for the case of random background charges. For the largest simulated array with size 20×20 the numerical results was $V_T(N = 20) \sim 1.0e/C$. Assuming that V_T scales linearly with the size of the array we can extrapolate this result and find $V_T(N = 200) \sim 10e/C$.

We can estimate the capacitance C from the measured threshold voltage

$$C = \frac{10e}{V_T} = 1.6\ \mathrm{fF}\ \frac{1}{V_T/\mathrm{mV}}. \tag{6.4}$$

Inserting $V_T = 7$ mV, which we measure at $V_g = -3.6$ V, we find $C = 0.23$ fF. This suggests that in our system C/C_g is of order 1. The threshold voltage increases for decreasing gate voltage with no apparent saturation at $V_g = -3.6\,\mathrm{V}$. A possible explanation is that the gate voltage tunes not only the tunneling resistance between neighboring islands but also the capacitance C of the barrier.

For the data shown in Fig. 6.3**a** the islands are in the normal state. Superconductivity of the aluminum islands is destroyed by applying an out-of-plane magnetic field of $B_z = 200\,\mathrm{mT}$, which exceeds the critical magnetic field of the film. At zero out-of-plane magnetic field the islands are in the superconducting state. In this case the we observe a pronounced increase of the threshold voltage, when compared to the normal state, as is visible in Fig. 6.3**b**. The threshold voltages for the normal and the superconducting case are compared in Fig. 6.3**c**. Compared to the case with normal conducting islands the threshold voltage in the superconducting state is roughly increased by a factor of two. This is in agreement with tunneling of Cooper pairs with charge $2e$ between the superconducting islands.

6.3. Thermal activation of transport in the deep-insulating state

We now study the temperature dependence of zero-bias conductivity in the insulating state. For $V_g < 3.3$ V, the normal state conductivity of the junctions is far below e^2/h. For a two dimensional array in the Coulomb blockade regime the expected temperature dependence of the zero-bias conductivity is given by the Arrhenius law [76, 75]

$$G(T) = G_0 e^{-E_A/k_B T}. \tag{6.5}$$

For semiconductor-superconductor arrays in the insulating regime the temperature dependence of the resistance was first studied in the supplemental information of [77]. This work explored the behavior close to the SIT using zero-bias differential resistance measurements. The authors found variable range hopping behavior for higher gate voltages and activated behavior in a small range of parameters at lower gate voltages.

In the following we give a detailed analysis of the activation energies found in our device. We study the case of the deep-insulating state where the temperature dependence is always described by activated behavior. Analyzing $I(V)$ measurements we are sensitive to conductivities as low as $10^{-6}e^2/h$.

For the non-superconducting case the excitations of the system which determine the activation energy are charge-anticharge dipoles. The excitation energies were obtained numerically in [75] for the case $C \gg C_g$. For a 2D array with random background charges the numerically computed activation energy is

$$E_A = 0.1e^2/C. \tag{6.6}$$

Fig. 6.4 shows Arrhenius plots of the conductivity for $V_g = -3.4$ V and $V_g = -3.6$ V. The conductivity is obtained by fitting $I(V)$ curves around zero voltage bias. The state with normal conducting islands is again studied by applying $B_z = 200$ mT (curves labeled NC in Fig. 6.4). For the normal state and the gate voltage $V_g = -3.6$ V we find the activation energy $E_A/k_B = 1.1$ K. Using Eq. (6.6) we find the capacitance $C \sim 0.16$ fF. The corresponding charging energy is $E_C = e^2/2C = 0.5$ meV. At $V_g = -3.4$ V we obtain $C = 0.27$ fF and $E_C = 0.3$ meV. The values of C extracted from the thermal activation of transport are in good agreement with the values found from the threshold voltage.

In the superconducting case, the aluminum islands will proximitze the electron gas in the InAs quantum well, resulting in an induced gap $\Delta^* < \Delta_{\mathrm{Al}} = 1.76k_BT_{c,\mathrm{Al}} \approx 300$ µeV. For JJAs with $\Delta \leq E_C$, previous studies on two-dimensional SIS arrays have found activation laws for the conductivity with activation energy [78, 79, 80]

$$E_A = \Delta + E_{A,N}. \tag{6.7}$$

The gap energy Δ is the activation energy for the creation of single-charge quasiparticles, while $E_{A,N}$ is the binding energy of a single-electron charge/anti-charge dipole [81]. Thermal activation of Cooper-pair dipoles becomes relevant if E_C is far below Δ and the temperature is below the partity-effect temperature T^*, where the number of thermally excited quasiparticles on each island becomes of order 1. The number N_{qp} of thermally excited quasiparticles is given by [82, 83, 84]

$$N_{\rm qp}(T) = N_{\rm eff}\exp(-\Delta/k_BT) \tag{6.8}$$
$$\text{with } N_{\rm eff} = 2\sqrt{2}V\rho(0)\sqrt{\Delta k_BT}, \tag{6.9}$$

where V is the volume of superconducting islands and $\rho(0)$ is the density of states. The parity-effect temperature is then

$$k_BT^* = \Delta/\log(N_{\rm eff}), \tag{6.10}$$

which is of the order $T^* \approx 0.2\,\mathrm{K}$ for nanoscale aluminum islands. In our system we always have $E_C \gtrsim \Delta$ and activation energies for the case of superconducting islands are obtained at temperatures $T \gtrsim T^* = 0.2$ K. We conclude that our experiments are in the parameter regime where the activation energy is given by Eq. (6.7).

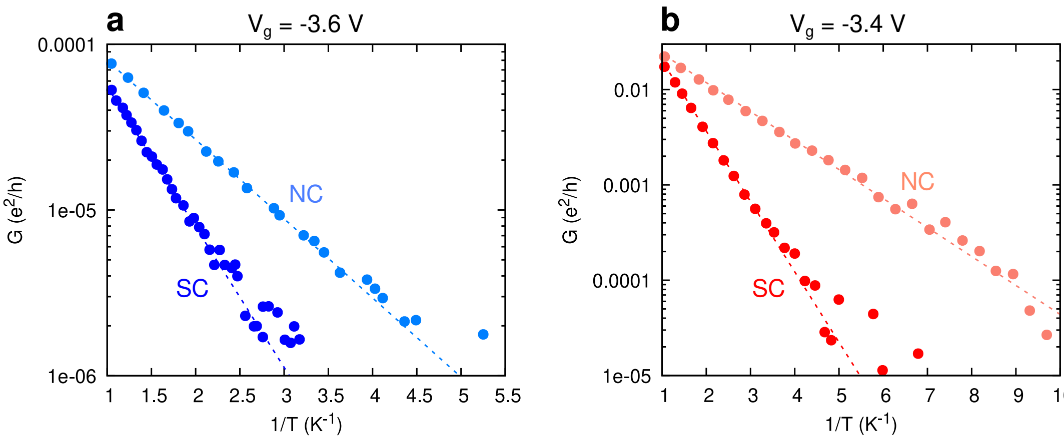

Fig. 6.4.: a, Thermal activation of transport for $V_g = -3.6\,\mathrm{V}$. Zero bias conductivity is obtained by fitting $I(V)$ curves for $|V| < 1\,\mathrm{mV}$. The extracted activation temperatures are $T_{A,S} = 1.95\,\mathrm{K}$ and $T_{A,N} = 1.10\,\mathrm{K}$. **b,** Thermal activation of transport for $V_g = -3.4\,\mathrm{V}$. $I(V)$ curves are fitted for $|V| < 25\,\mu\mathrm{V}$. The extracted activation temperatures are $T_{A,S} = 1.70\,\mathrm{K}$ and $T_{A,N} = 0.70\,\mathrm{K}$.

In the superconductor-semiconductor array the relevant superconducting gap for quasiparticle creation is the induced gap Δ^* in the semiconductor, as it is the smallest gap in the electronic system of the islands. This is unlike the previously studied arrays of SIS junctions, where the required energy to create quasiparticles is the gap energy of the aluminum superconductor. In our case, the thermal activation energy is therefore given by

$$E_A = \Delta^* + E_{A,N}. \tag{6.11}$$

By comparing the activation energies in the normal and the superconducting state we have a method to determine Δ^*. Using $\Delta^* = E_{A,S} - E_{A,N}$, we find

$$\Delta^*(V_g = -3.4\text{ V}) = 1.0\text{ K}\cdot k_B = 86\ \mu\text{eV} \tag{6.12}$$
$$\text{and } \Delta^*(V_g = -3.6\text{ V}) = 0.85\text{ K}\cdot k_B = 73\ \mu\text{eV}. \tag{6.13}$$

6.3.1. Discussion

In previous works the induced gap in semiconductor-superconductor heterostructures was measured using quantum point contact spectroscopy. A value of $\Delta^* \sim 190\,\mu\text{eV}$ was found in [85]. Another measurement of Δ^* is possible using the temperature dependence of the Josephson inductance, from which $\Delta^* = 130\,\mu\text{eV}$ was found [86]. The values obtained using the technique described here are slightly smaller. We note that we use a different layer stack which is optimized for high mobility in the near-surface quantum well. The lower coupling between superconductor and quantum well could explain the smaller induced gap. We find that the obtained value of the induced gap depends on the gate voltage. It is an interesting question how the depletion of the electron gas in the junctions affects the induced gap below the aluminum islands. Possibly, the gate voltage tunes the effective size of the proximitized region in the semiconductor, which could affect the induced superconducting gap. This could be analyzed by studying arrays with different lattice constants.

The measurement of activation energies could also be used to study the influence of the in-plane magnetic field on the induced gap. Thereby one could study the closing of the induced gap and would obtain the effective g-factor g^*, similar to recent tunneling spectroscopy measurements on InSbAs/Al structures [87]. Rotating the in-plane field could reveal crystallographic anisotropies of the g-factor.

7. Summary

This thesis studies effects in Josephson junctions which arise in the presence of spin-orbit coupling and Zeeman fields. The experimental platform is a hybrid superconductor-semiconductor heterostructure. A near-surface InAs quantum well is proximitized by an epitaxial film of superconducting aluminum. Josephson junctions are fabricated by selective etching of the superconductor. Measurements are performed at sub-Kelvin temperatures in a specialized dilution refrigerator setup.

Chapter 2 gives an introduction to the physics of SNS Josephson junctions. The most simple model of a superconducting weak link is found from the Ginzburg-Landau theory which is valid close to the critical temperature of the superconductor. We then introduce the more recent models of short SNS junctions which also include the case of ballistic junctions with high transparency. The electronic structure of materials involving heavy elements is strongly influenced by spin-orbit coupling. Broken structure inversion symmetry gives rise to spin-orbit coupling of the Rashba type. The application of magnetic fields leads to a Zeeman interaction which breaks time-reversal symmetry. In Josephson junctions the spin-orbit coupling and Zeeman interaction give rise to new effects. We present a model of Josephson junctions developed by our theory colleagues which provides a good qualitative understanding of the current phase relation in ballistic junctions in the presence of Rashba-type spin-orbit coupling and Zeeman fields.

The experiment described in Chapter 3 enables the measurement of both anomalous Josephson effect and superconducting diode effect using an asymmetric superconducting quantum interference (SQUID) device. The SQUID device is studied by measuring critical current as a function of applied flux. The resulting interference patterns deviate strongly from the case of a "textbook"-SQUID device. The reason is the large kinetic inductance of the thin aluminum film which leads to screening of the applied flux. This behavior can be described by numerical simulations using a circuit model which includes the effects of kinetic inductance. Using the SQUID device, the gate dependence of the anomalous phase shift can be measured with very high accuracy. Measurement of the anomalous phase shift φ_0 for different orientations of the in-plane field shows the behavior which is expected for a magnetochiral quantity

$$\varphi_0 \sim (\vec{B}_{\mathrm{ip}} \times \vec{I}) \cdot \sin(\theta). \tag{7.1}$$

In addition to the measurement of the anomalous phase shift, the SQUID device also allows the determination of the Josephson diode effect (JDE) for the same junction. Like the anomalous phase shift, the JDE is tunable with the top gate voltage, and shows the characteristic dependence on the magnitude of the in-plane field that was first observed in the previous works of our group. The temperature dependence of the JDE and the anomalous phase shift is strikingly different: The JDE is rapidly suppressed by increasing the temperature, while the anomalous phase shift shows very little dependence on temperature.

The following three chapters study the physics of two-dimensional Josephson junction arrays fabricated from the hybrid superconductor-semiconductor material platform. Chapter 4 studies the influence of magnetochiral effects on vortex pinning. We observe a *magnetochiral vortex ratchet effect* which is controlled by the Zeeman field. This new effect is explained by introducing a XY model of the JJA with anomalous phase shifts and next-nearest neighbor interaction. In this model the anomalous phase shift generates persistent currents and the current configuration of vortices breaks four-fold rotational symmetry. The depinning currents resulting from the model are found using detailed numerical simulations. We present a control experiment with another JJA device where the coupling between next-nearest neighboring islands is strongly reduced. As expected, the vortex ratchet effect is much smaller in this device.

The vortex density in the JJAs can be tuned with the out-of-plane magnetic field. For commensurate values of the frustration parameter the vortices form ordered patterns. The ordered configurations of vortices result in maxima of the depinning current and are observed for for both integer and fractional values of frustration. The ratchet effect is studied for higher out-of-plane fields up to the first matching field, which corresponds to a density of one vortex per unit cell. We find an enhancement of the ratchet effect at both integer and fractional values of the frustration parameter. In addition, we observe a sign-reversal of the ratchet effect for values of frustration around $f = 1/3$.

Pinning of vortices in two-dimensional Josephson junction arrays results in a inductive response, similar to the well-known kinetic inductance of superconductors. This vortex inductance is studied in Chapter 5. Inductance is measured using a MHz-frequency LC resonator which is part of the sample holder. We measure inductance as a function of vortex density and observe characteristic dips of inductance at commensurate values of the frustration parameter. The ordered vortex patterns result in stronger pinning, which leads to the decreased inductance. We highlight the importance of thermal annealing procedures, which are required to bring vortices into equilibrium configurations.

In addition we probe vortex inductance as a function of an applied dc current in the presence of in-plane magnetic fields. These measurements indicate a asymmetric shape of the vortex pinning potential which is an additonal signature of the magnetochiral vortex ratchet effect. We discuss possible improvements which could be implemented in future measurements of vortex inductance in two-dimensional JJAs.

Chapter 6 studies the insulating behavior of a two-dimensional JJA device. The top gate is used to tune the normal state sheet resistance above the resistance quantum $R_Q = h/e^2 = 25.8\,\mathrm{k\Omega}$. Tuning the gate voltage we study the transition from superconducting to insulating behavior. In the insulating regime we observe critical threshold voltages caused by Coulomb blockade effects. This critical voltage depends on the gate voltage, showing an effect of gate voltage on the junction capacitance.

In order to study the activation of conductance with temperature we perform $I(V)$ measurements in the insulating regime. The extracted zero-bias conductance can be fitted with the Arrhenius law $G(T) \sim \exp(-E_A/k_BT)$. We measure the activation energy E_A for the case of both normal conducting and superconducting islands. It is found that for superconducting islands the thermal activation of conductance is due to single-electron effects caused by thermally activated quasiparticles. Because of this, the measurement of activation energies allows the extraction of the induced superconducting gap Δ^* in the proximitized semiconductor quantum well.

A. Characterization of the near-surface InAs/InGaAs quantum well

This appendix presents the characterization of the Al/InGaAs/InAs wafer *M01-08-22.1*, which was grown by the group of Prof. M. Manfra in early 2022. The layer structure of this wafer is shown in Fig. A.1. Most of the measurements presented in this thesis were performed with this wafer, with the exception of the data on vortex inductance in Chapter 5, and the control experiment in Section 4.6, which were measured with devices fabricated from wafer *M10-08-18.2*. A detailed characterization of wafer *M10-08-18.2* can be found in the thesis of C. Baumgartner [37].

Basic transport properties of the semiconductor quantum well are performed with a standard Hall bar device. The mesa of the Hall bar device is wet etched to a depth of 250 nm using a solution of phosphoric acid, citric acid, hydrogen peroxide, and deionized water. The composition of the solution is H_3PO_4:$C_6H_8O_7$:H_2O_2:H_2O 1.2:14:2:88. Selective etching of aluminum is then performed with aluminum etchant type D from Transene at 50 °C for 5 s. The Hall bar is covered with 60 nm aluminum oxide grown by atomic layer deposition at 80 °C. Before the first pulse (trimethylaluminum), the sample is dried in the ALD chamber under nitrogen flow for 2 hours. Finally, a Ti/Au (5 nm / 100 nm) top-gate is deposited onto the channel of the Hall bar.

In Fig. A.2**a-d** we show Hall mobility, mean free path, Fermi wavelength, and Fermi velocity as a function of carrier density at $T = 1.5$ K. The peak mobility $\mu > 60000$ cm^2/Vs is obtained at the density $n \sim 5 \times 10^{11}$ cm^{-2}.

The electron effective mass is determined from the temperature dependence of Shubnikov-de Haas (SdH) oscillations, following [88]. Fig. A.2**e** shows SdH oscillations in the resistance with a second-order polynomial background removed in order to obtain the amplitude of each oscillation as a function of temperature. The carrier density obtained from the oscillations is $\sim 7 \times 10^{11}$ cm^{-2}. For each maximum and minimum of the oscillations we obtain an effective mass by fitting the temperature dependence of the amplitude with the formula

$$A_{\mathrm{SdH}}(T) \sim \frac{2\pi^2 k_B T/\hbar\omega_c}{\sinh(2\pi^2 k_B T/\hbar\omega_c)} \tag{A.1}$$

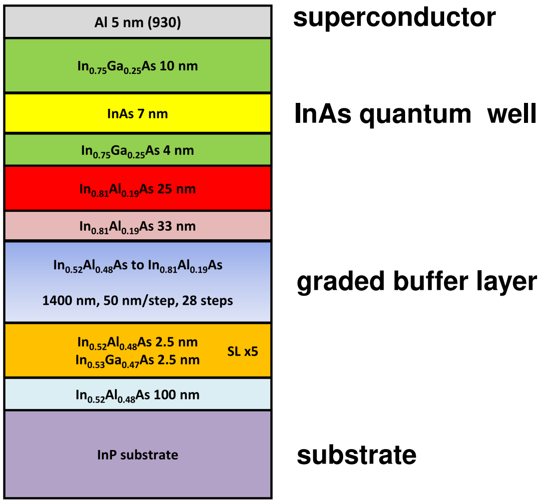

Fig. A.1.: Layer stack of the wafer *M01-08-221*. Provided by group of M. Manfra

The obtained mass $m^*/m_e = 0.036 \pm 0.005$ is slightly lower compared to the value $m^*/m_e = 0.04$ found in [88].

Fig. A.2**f** shows the resistance of the heterostructure, including the aluminum film, as a function of temperature, measured in a Hall bar geometry. Due to the low thickness of the film, the critical temperature is enhanced to 2.07 K with a normal state sheet resistance of 36 Ω.

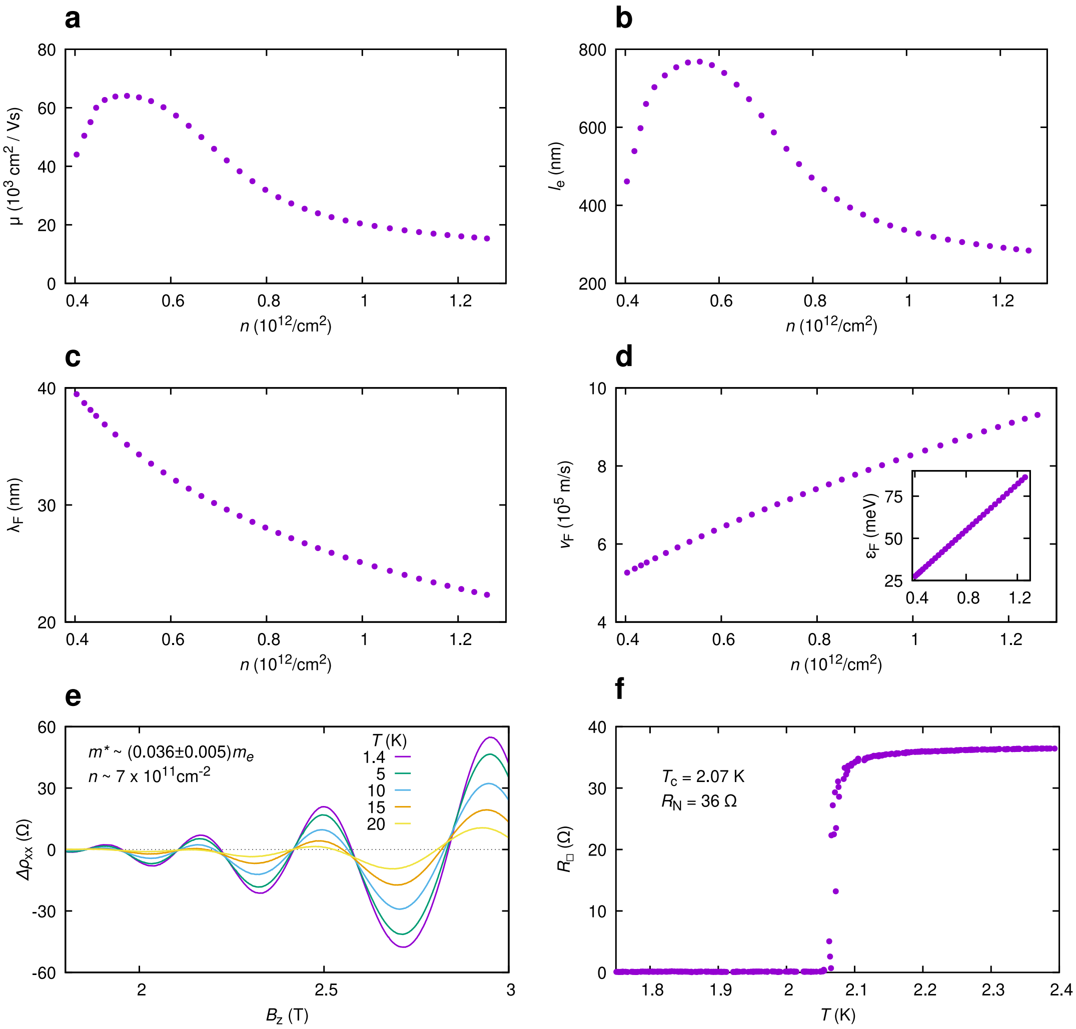

Fig. A.2.: a-d, Transport properties of the quantum well measured with a top gated Hall bar at temperature $T = 1.5$ K. The inset of panel **e** shows the Fermi level ε_F versus n. The range in gate voltage corresponding to the n-range displayed in panels **b-e** is [-3.5 V,-0.2 V]. **e,** Amplitude of Shubnikov-de Haas oscillations for temperatures between 1.4 K and 20 K. **f,** $R(T)$ Characteristic of a Hall bar device with the pristine aluminum film.

B. The dilution refrigerator system

The Cryoconcept dilution refrigerator is operated in an Oxford Instruments liquid helium dewar with a liquid nitrogen shield. The dewar is equipped with a 2D vector magnet. A solenoid coil provides up to 7 T in z-direction, while a split pair provides up to 3 T in the x-direction. Both X and Z magnet are provided with persistent mode switches.

B.1. Cabling and filtering

Resistive coaxial cabling is used for both inductance measurements in the MHz regime and for low-pass filtering of DC lines. The cables of type GVLZ185 have a CuNi (70%, 30%) center wire with room temperature resistance of $32\,\Omega$ or $60\,\Omega$, depending on the batch. The braided shielding consists of CuNi (55% Cu, 44% Ni, 1% Mn). An advantage of this cable over stainless steel coax is that it can be soldered without highly corrosive acid flux. For the RF lines we connectorize the cables with commercial SMA connectors (Amphenol 132249). The coaxial lines are thermalized at each cooling stage of the dilution fridge by soldering the shield to a copper braid. Between stages the cables are wrapped around plastic rods to gain extra length to increase attenuation, as shown in Fig. B.1**a**. Fig. B.2 shows a room temperature measurement of the cable attenuation. At 3 GHz the attenuation exceeds 50 dB/m. The attenuation is similar to the often used semi-rigid stainless steel coax cables from COAX CO. such as SC-033/50-SS-SS. The cryogenic low noise amplifier (Cosmic Microwave CITLF1S) is thermalized to the 4K stage. The gain of the amplifier at low temperature is above 20 dB for $f < 2$ GHz, and the input noise temperature is below 7 K.

DC lines use manganin wires between the breakout box at room temperature and the mixing chamber plate. Below the mixing chamber we use resistive coax for low pass filtering. The coaxial lines with a length of ~ 1 m are wrapped around the coldfinger. At room temperature we typically use Pi-type LC filters (Tusonix 4201-053) with a cutoff frequency of 10 MHz.

The lines used to drive the piezo rotator (Attocube ANRv220) require a very low resistance, below $3\,\Omega$ for the two lines in series. Between room temperature and the 4K stage we use copper wires, while between 4K and the mixing chamber we use superconducting NbTi/CuNi (GVLZ018) in parallel to phosphor bronze

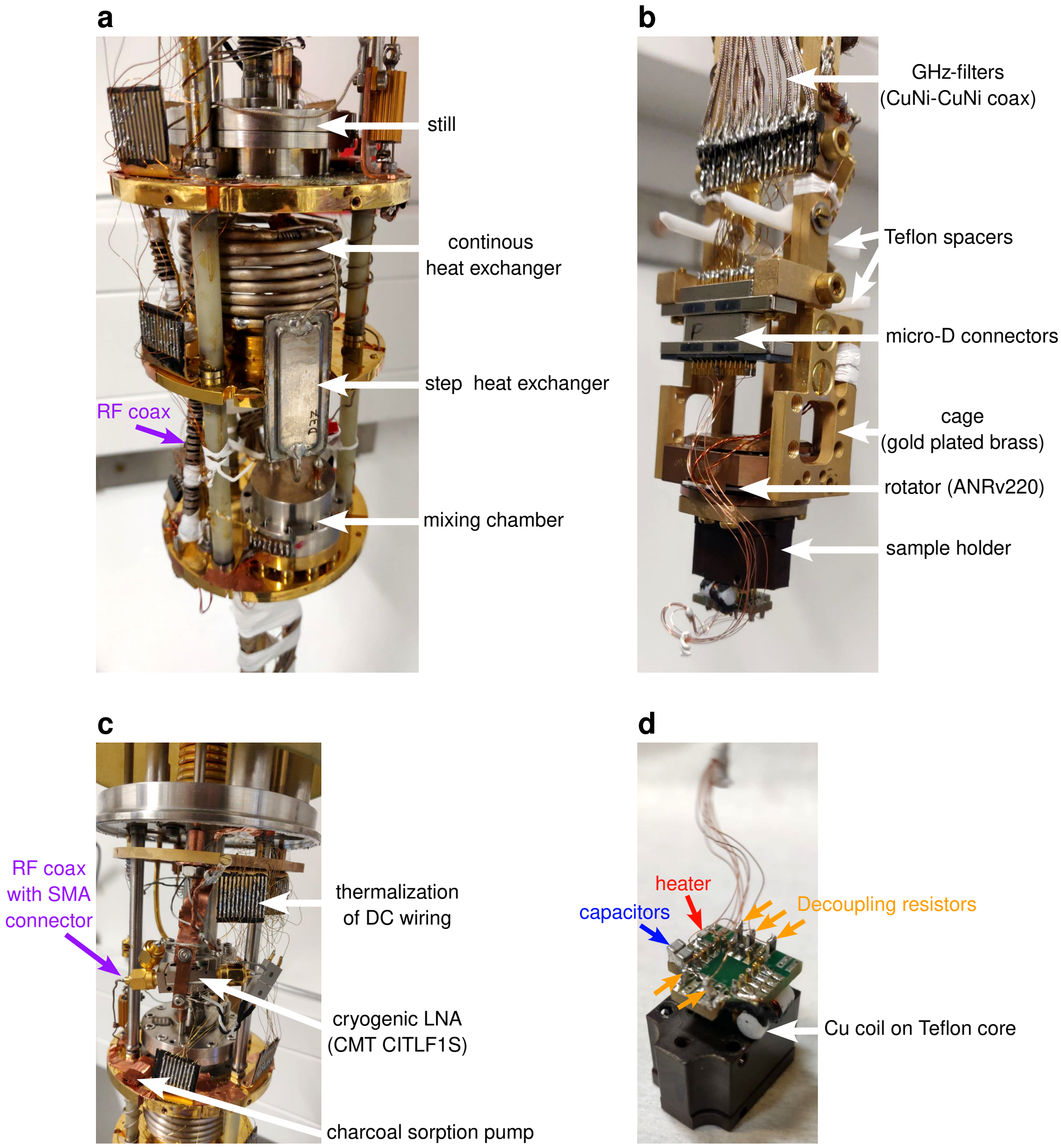

Fig. B.1.: Cryostat wiring. **a**, Cooling stages and heat exchangers of the dilution cryostat. **b**, End of the coldfinger with mounted rotator and sample holder. **c**, Still and 4K stages with cryogenic LNA mounted to the 4K stage. **d**, Sample holder with integrated LC resonator.

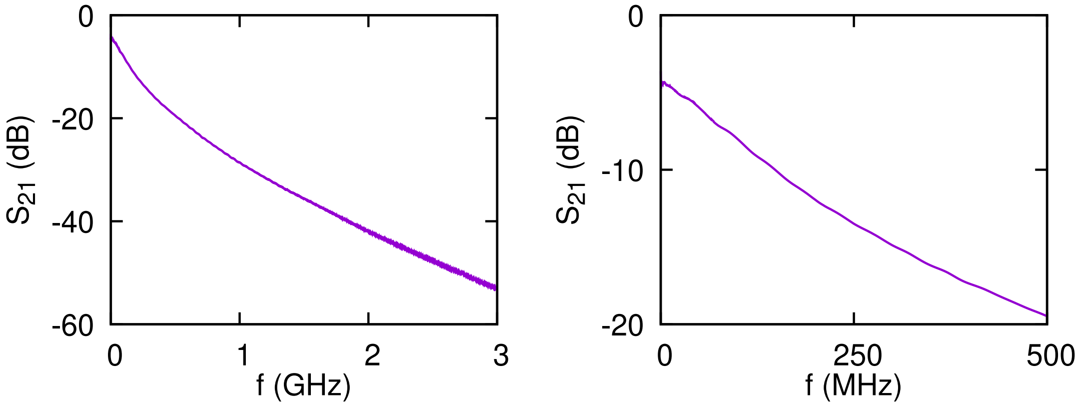

Fig. B.2.: Attenuation measurement of CuNi-CuNi coax cable (GVLZ-185). The length of the cable is 1 m. Right panel: Zoom into low frequency range.

wires. This way the rotator can be operated at arbitrary temperature of the system. For the three read-out lines of the piezo rotator we use manganin wires.

B.2. Cryogenic LC resonator design

A photo of the sample holder with integrated LC resonator is shown in Fig. B.1**d**. A schematic of the circuit and the read-out electronics are shown in Fig. B.3.

For the decoupling resistance $R_D = 1\,\mathrm{k}\Omega$ we use metal thin-film resistors from the Susumu RR-series which are known to have little change in resistance when cooled to cryogenic temperatures [89]. This resistor is also used for the $1\,\mathrm{k}\Omega$ heater on the sample PCB.

The capacitance $C_0 = 4\,\mathrm{nF}$ is implemented using four 1 nF SMD capacitors connected in parallel. We use SMD capacitors with the NP0/C0G dielectric (e.g. Würth Elektronik WCAP-CSGP MLCC). The temperature stability is checked by submerging the capacitors in liquid nitrogen while measuring the capacitance with a LCR meter. Typically the capacitance will only change by a few percent from the room temperature value.

The coil with inductance L_0 consists of few turns of 200 µm copper wire wrapped around a Teflon core. The number of turns is changed until the resonance frequency is in the desired range. The coil is then fixed in place with Stycast.

Transmission measurements of the resonator are done using a vector network analyzer (R&S ZNL3). The output power range of the VNA is $-40\,\mathrm{dBm}$ to $0\,\mathrm{dBm}$. The output signal is attenuated by $-90\,\mathrm{dB}$ using SMA attenuators (e.g. CRYSTEK CATTEN-0200). A dc bias current is added using a bias tee. The bias current is generated using a voltage source (Yokogawa GS200) with

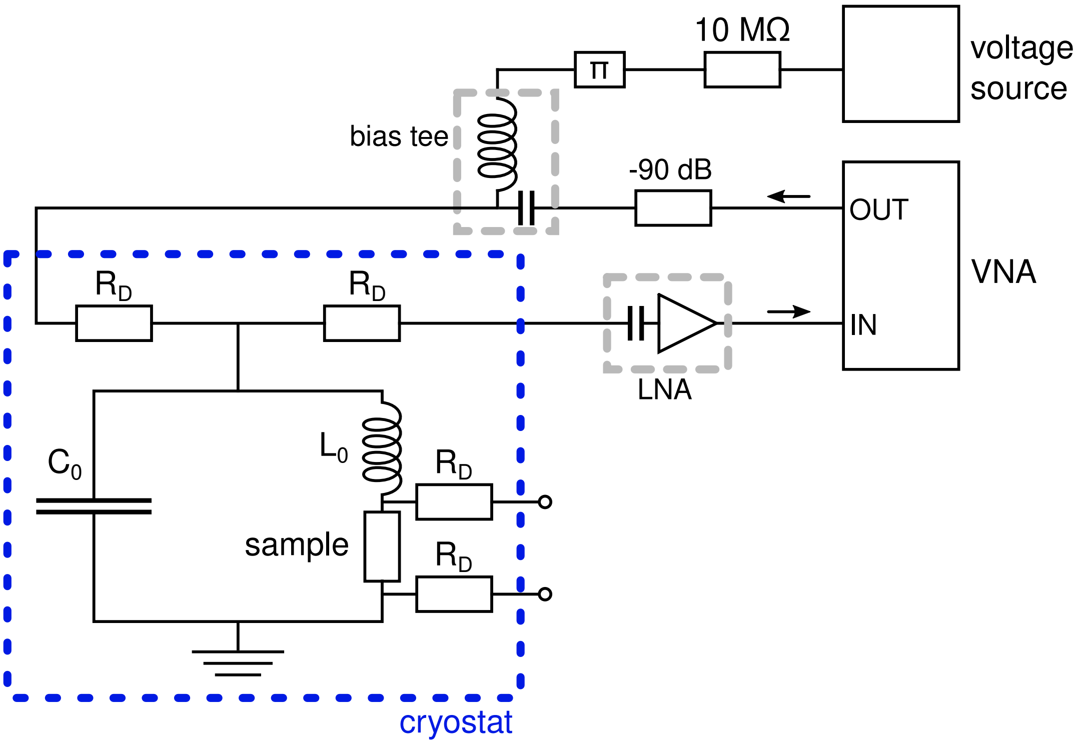

Fig. B.3.: Schematic of setup used for transmission measurements.

a 10 MΩ resistor. The output signal is amplified by 60 dB using a room temperature low noise amplifier (Wenteq Microwave ABL0040-00-6010, 100 kHz to 400 MHz). The latest version of the measurement setup additionally uses a cryogenic low noise amplifier mounted on the 4 K-stage. The amplifier (CITLF1S, Cosmic Microwave Technology) uses a single silicon-germanium transistor and provides a gain of 20 dB up to 2 GHz. In the MHz frequency range the effective input noise temperature is $T_N \sim 4\,\mathrm{K}$.

All measurements performed for this thesis are controlled using the Lab::Moose software stack [90].

B.3. Thermometers and heaters

The following thermometers are used in the system

- A Cernox CX-1010 resistance thermometer with generic calibration between 300K and 0.1K is mounted on the still plate.

- A calibrated germanium thermometer from Lakeshore is mounted on the bottom side of the mixing chamber. The calibration is provided between 6.5 K and 44 mK. For lower temperatures we extend the calibration, by fitting the existing calibration below 200 mK with [91]

$$\log(R) = A_0 + A_1 \log(T) + A_2 \log(T)^2$$

- The sample thermometer is a commercial thick-film resistor mounted at the end of the coldfinger, close to the final thermalization of the DC lines. The callibration was generated using the variable-range hopping law [91]

$$R = R_0 \exp(T_0/T)^{1/4},$$

  which well describes the $R(T)$ behavior for $T < 1\,\mathrm{K}$.

The main heater is a $1\,\mathrm{k}\Omega$ metal thin-film resistor mounted on the mixing chamber plate. The available temperature range with the full mixture in the system is $35\,\mathrm{mK} < T < 1.1\,\mathrm{K}$.

The still heater mounted on the still plate is currently only used when recovering the mixture from the dilution unit.

C. Network analysis of LC resonators

In this section we derive analytical formulas for the transmission parameter $S_{21}(\omega)$ of the LC resonators used for inductance measurements. The resulting expressions are used to fit the measurement data and extract inductance and sample resistance.

C.1. LC resonators with resistive decoupling

Fig. C.1**a** shows our circuit model of a resistively decoupled LC resonator. Similar to the case of planar resonators the analysis of the circuit is simplified by studying the Norton equivalent [92]. The resulting parallel LCR circuit is shown in Fig. C.1**b**. The parameters R and L of the parallel circuit are found by solving the equation

$$R_S + i\omega(L_0 + L_S) = R \| i\omega L = \frac{iR\omega L}{R + i\omega L}. \tag{C.1}$$

This gives

$$\begin{aligned} L &= (L_0 + L_S)\left(1 + \frac{R_S^2}{\omega^2 (L_0 + L_S)^2}\right) \\ R &= \frac{R_S^2 + \omega^2 (L_0 + L_S)^2}{R_S}. \end{aligned}$$

L and R are assumed to be constant for $\omega \sim \omega_0$. For $R_S \ll \omega_0 L = \sqrt{L/C}$ we have $R \sim L/(CR_S)$ and $L \sim L_0 + L_S$.

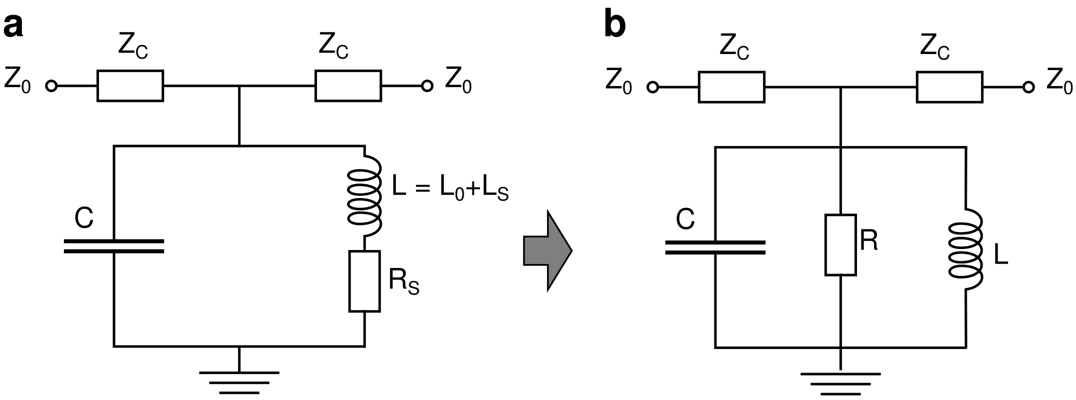

Fig. C.1.: **a**, Circuit diagram of the LC resonator. The sample is modeled by an inductor and a resistor connected in series. Z_0 is the impedance of the transmission lines and can be set to $50\,\Omega$. **b**, Norton equivalent of the circuit used for network analysis.

The transmission parameter S_{21} can be found starting from the impedance matrix $[Z]$ [93, Chap. 4]

$$[Z] = \begin{pmatrix} Z_C + Z_{RLC} & Z_{RLC} \\ Z_{RLC} & Z_C + Z_{RLC} \end{pmatrix}$$

with $Z_{RLC} = R \parallel i\omega L \parallel 1/(i\omega C)$. For the transmission parameter we obtain

$$S_{21} = \frac{2Z_{21}Z_0}{det([Z]+Z_0)} = \frac{2Z_{RLC}Z_0}{(Z_C+Z_{RLC}+Z_0)^2 - Z_{RLC}^2} = \tag{C.2}$$

$$\frac{2Z_{RLC}Z_0}{(Z_C+Z_0)^2 + 2(Z_C+Z_0)Z_{RLC}} = \frac{Z_0}{Z_C+Z_0}\frac{1}{1+\frac{Z_C+Z_0}{2Z_{RLC}}}. \tag{C.3}$$

For the denominator we get using $\omega_0 = 1/\sqrt{LC}$

$$\begin{aligned} 1 + \frac{Z_C+Z_0}{2Z_{RLC}} &= 1 + (Z_C+Z_0)/2 \times (1/R + i(\omega C - \frac{1}{\omega L})) \\ &= \frac{2R+Z_C+Z_0}{2R}\left(1 + \frac{R(Z_C+Z_0)}{2R+Z_C+Z_0} i(\omega C - \frac{1}{\omega L})\right). \end{aligned}$$

We can rewrite this using

$$i(\omega C - \frac{1}{\omega L}) = iC\omega_0 \frac{\omega^2 - \omega_0^2}{\omega\omega_0} = i\sqrt{C/L}\frac{\omega^2-\omega_0^2}{\omega\omega_0}.$$

The resulting formula for the transmission is

$$S_{21}(\omega) = S_{21}(\omega_0)\frac{1}{1 + iQ_L(\frac{\omega^2-\omega_0^2}{\omega\omega_0})} \tag{C.4}$$

with the *loaded quality factor*

$$Q_L := \frac{R(Z_C+Z_0)}{2R+Z_C+Z_0}\sqrt{\frac{C}{L}}.$$

Close to the resonance frequency the expression for $S_{21}(\omega)$ is simplified to

$$S_{21}(\omega) \sim \frac{S_{21}(\omega_0)}{1 + 2iQ_L\frac{\omega-\omega_0}{\omega_0}}. \tag{C.5}$$

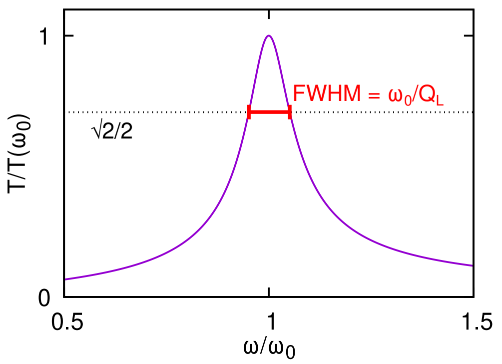

Fig. C.2.: Resonance curve plotted using Eq. (C.4). The loaded quality factor is set to $Q_L = 10$. Normalized transmission $|S_{21}(\omega)/S_{21}(\omega_0)|$ is plotted versus normalized frequency ω/ω_0. The FWHM is the bandwidth of the resonance where the transmission is above $\sqrt{2}/2$, i.e., where the transmitted power is reduced by 3 dB relative to the maximum.

The loaded quality factor is related to the *full width at half maximum* (FWHM) of the resonance. The definition of the FWHM is illustrated in Fig. C.2.

The maximum transmission is given by

$$S_{21}(\omega_0) = \frac{Z_0}{Z_C + Z_0}\frac{2R}{2R + Z_C + Z_0} = \frac{Z_0}{Z_C + Z_0}\frac{Q_L}{Q_E}$$

with the *external quality factor*

$$Q_E := \frac{Z_C + Z_0}{2}\sqrt{\frac{C}{L}}$$

and the *internal quality factor*

$$Q_I := R\sqrt{\frac{C}{L}}.$$

The loaded quality factor is determined by the internal and external quality factors by

$$\frac{1}{Q_L} = \frac{1}{Q_E} + \frac{1}{Q_I}.$$

When $R_S \ll \omega_0(L_0 + L_S)$ the following are good approximations

$$L \sim (L_0 + L_S)$$
$$R \sim \frac{L}{CR_S}$$

and the internal quality factor is given by

$$Q_I = \frac{1}{R_S}\sqrt{\frac{L}{C}}.$$

C.1.1. Sensitivity of inductance measurement

The inductance is determined from the resonance frequency ω_0. The resonance frequency is in turn obtained from the transmission measurement where a set of complex voltages is measured for an array of frequencies. To find the sensitivity of the inductance measurement we need to calculate the error propagation from the voltage measurement of the VNA to the inductance obtained by fitting the data. The resolution of the measurement will be proportional to the excitation voltage applied to the resonator. The maximum excitation that can be used in a measurement is limited by the ac current excitation at the sample, which must typically be much smaller than the critical current of the sample. The ac excitation can be found starting from the output voltage $V_{out} = S_{21}V_{in}$ of the resonator:

$$I_{sample}(\omega = \omega_0) = V_{out}\frac{Z_C + Z_0}{Z_0\omega_0 L}$$

The sensitivity of the inductance measurement is linked to the quantity

$$S_L := |\frac{dV_{out}(\omega_0)}{dL}| = |\frac{dS_{21}(\omega_0)}{d\omega}|\frac{d\omega_0}{dL}V_{in} = (Q_L/L)V_{out}$$

The interesting quantity is S_L/I_{sample}:

$$S_L/I_{sample} = \frac{Z_0}{Z_C + Z_0}\omega_0 Q_L$$

If the external quality factor is not much larger than the internal quality factor, we have $Q_L \sim Q_E$ and we find

$$S_L/I_{sample} \sim \frac{Z_0}{Z_C + Z_0}\omega_0 Q_E = \frac{Z_0}{2L}$$

The resolution of the inductance measurement is therefore inversely proportional to the total inductance in the resonator.

C.2. Hanger-type resonators

Another type of LC resonator used for inductance measurements in our research group are “hanger-type” resonators. This design uses capacitive coupling to a feedline. The advantage is that multiple resonators with different resonance frequency can be coupled to a single feedline. As we will see, this type of resonator can yield higher sensitivity in inductance measurements for high quality factors, i.e. when using all-superconducting on-chip resonators. The disadvantage is that DC access requires additional inductive or resistive decoupling elements.

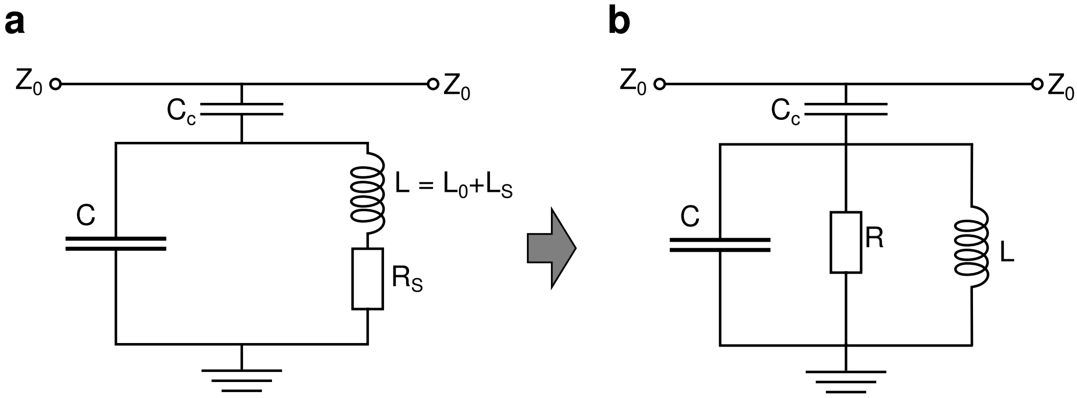

Fig. C.3.: **a**, Circuit diagram of the "hanger-type" resonator. Z_0 is the impedance of the transmission lines and can be set to 50 Ω. **b**, Norton equivalent of the circuit used for network analysis.

The network analysis of the circuit is based on the work of B. A. Mazin [94].

For the feedline shunted to ground by the impedance Z, the S parameters are given by

$$S_{21} = \frac{1}{1+\frac{Z_0}{2Z}}$$
$$S_{11} = \frac{-\frac{Z_0}{2Z}}{1+\frac{Z_0}{2Z}}$$

For the parallel LCR with coupling capacitance C_c the impedance is given by

$$Z = 1/(i\omega C_c) + \frac{R}{1+2iQ_i\Delta\omega/\omega_0} = 1/(i\omega C_c) + \frac{R(1-2iQ_i\Delta\omega/\omega_0)}{1+4Q_i^2\Delta\omega^2/\omega_0^2}$$

The minimum of $|S_{21}(\omega)|$ occurs when the inductive components of the coupling capacitor and the RLC resonator compensate each other and $\mathrm{Im}(Z(\omega)) = 0$. At the new resonance frequency ω_0^* we have $Q_i(\omega_0^* - \omega_0) \gg 1$, therefore the condition $\mathrm{Im}(Z(\omega)) = 0$ leads to

$$\frac{1}{\omega_0^* C} = -\frac{R}{2Q_i\Delta\omega/\omega_0}$$
$$\Delta\omega = \omega_0^* - \omega_0 = -\frac{\omega_0\omega_0^* C_c R}{2Q_i} \sim -\frac{\omega_0 C_c}{2C}$$
$$\Delta\omega/\omega_0 = -\frac{C_c}{2C}$$

write $Z(\omega)$ as function of $\Delta\omega^* = \omega - \omega_0^*$. To first order in $\Delta\omega^*/\omega_0$:

$$\begin{aligned}
\mathrm{Re}(Z(\omega)) &= \frac{R}{4Q_i^2\Delta\omega^2/\omega_0^2} \sim \frac{RC^2}{Q_i^2C_c^2} \text{ at } \omega = \omega_0^* \\
\mathrm{Im}(Z(\omega)) &= \frac{-1}{\omega C_c} - \frac{R}{2Q_i(\Delta\omega^* + \Delta\omega)/\omega_0} \sim \frac{R\Delta\omega^*\omega_0}{2Q_i\Delta\omega^2} = \frac{2RC^2}{Q_iC_c^2}\frac{\Delta\omega^*}{\omega_0}
\end{aligned}$$

and close to the resonance frequency ω_0^* we have the approximation

$$Z(\omega) \sim \frac{RC^2}{Q_i^2C_c^2}(1 + 2iQ_i\frac{\Delta\omega^*}{\omega_0}) =: A(1+\delta)$$

And S_{21} is given by

$$\begin{aligned}
S_{21}(\delta) = \frac{2}{2 + Z_0/Z} = \frac{2}{2 + \frac{Z_0}{A(1+\delta)}} = \frac{2A(1+\delta)}{2A(1+\delta) + Z_0} &= \frac{2A/(2A+Z_0) + \delta'}{1+\delta'} \\
\text{with } \delta' &:= \delta\frac{2A}{2A+Z_0}
\end{aligned}$$

the loaded quality factor is

$$\begin{aligned}
Q_L &= Q_i\frac{2A}{2A+Z_0} \\
S_{21,min} = \frac{2A}{2A+Z_0} &= \frac{Q_c}{Q_i+Q_c} = \frac{Q_L}{Q_i} \\
Q_c = 2AQ_i/Z_0 = \frac{2RC^2}{Q_iC_c^2Z_0} &= \frac{2C}{\omega_0C_c^2Z_0}
\end{aligned}$$

and the ratio C/C_c can be linked to the coupling quality factor by

$$\frac{C}{C_c} = \sqrt{\frac{Q_cZ_0}{2Z_{\text{char}}}}$$

with $Z_{\text{char}} := \sqrt{L/C}$.

Our final expression for the transmission of the resonator is

$$S_{21}(\omega) = \frac{\frac{Q_c}{Q_i+Q_c} + 2iQ_L\Delta\omega^*/\omega_0}{1 + 2iQ_L\Delta\omega^*/\omega_0} \tag{C.6}$$

For an over-coupled resonator $S_{21,min} \sim 0$ and $|S_{21}|^2 = 1/2$ for $\Delta\omega = \omega_0/(2Q_L)$.

C.2.1. Sensitivity

Again we first need to find the current excitation in the sample at resonance

$$I_{sample} = V_x/\omega_0^* L$$

$$|V_x| = V_{out}|\frac{Z_{RLC}(\omega_0^*)}{Z(\omega_0^*)}| \sim V_{out}\frac{Q_i C_c}{C} = V_{in}\frac{Q_L C_c}{C}$$

In order to find the quantity $S_L := |\frac{dV_{out}(\omega_0)}{dL}|$ we use

$$S_{21}(\omega) = \frac{\frac{2A}{2A+Z_0} + \delta'}{1+\delta'} \sim (\frac{2A}{2A+Z_0} + \delta')(1-\delta') \sim \frac{2A}{2A+Z_0} + (1 - \frac{2A}{2A+Z_0})\delta'$$

$$\text{with } 1 - \frac{2A}{2A+Z_0} = \frac{Q_i}{Q_i+Q_c}$$

and

$$|dS_{21}/d\omega|_{\omega=\omega_0^*}| = 2Q_L/\omega_0 \frac{Q_i}{Q_i+Q_c}$$

$$S_L = Q_L/L \frac{Q_i}{Q_i+Q_c} V_{in}$$

$$S_L/I_{sample} = \frac{Q_i C \omega_0}{(Q_i+Q_c)C_c} = \omega_0 \frac{Q_i}{Q_i+Q_c}\sqrt{\frac{Q_c Z_0}{2Z_{\text{char}}}}$$

The sensitivity scales with $\omega_0\sqrt{Q_c}$. This is unlike the case of the resistively coupled resonator, where the sensitivity depends only on $1/L$ and not the quality factor. We conclude that the "hanger-type" resonator can be used to obtain higher sensitivity for large quality factors. For a given internal quality factor Q_i, the maximum value of the sensitivity is obtained for $Q_c = Q_i$, i.e. for critical coupling.

D. Vortex inductance measurements at high in-plane fields

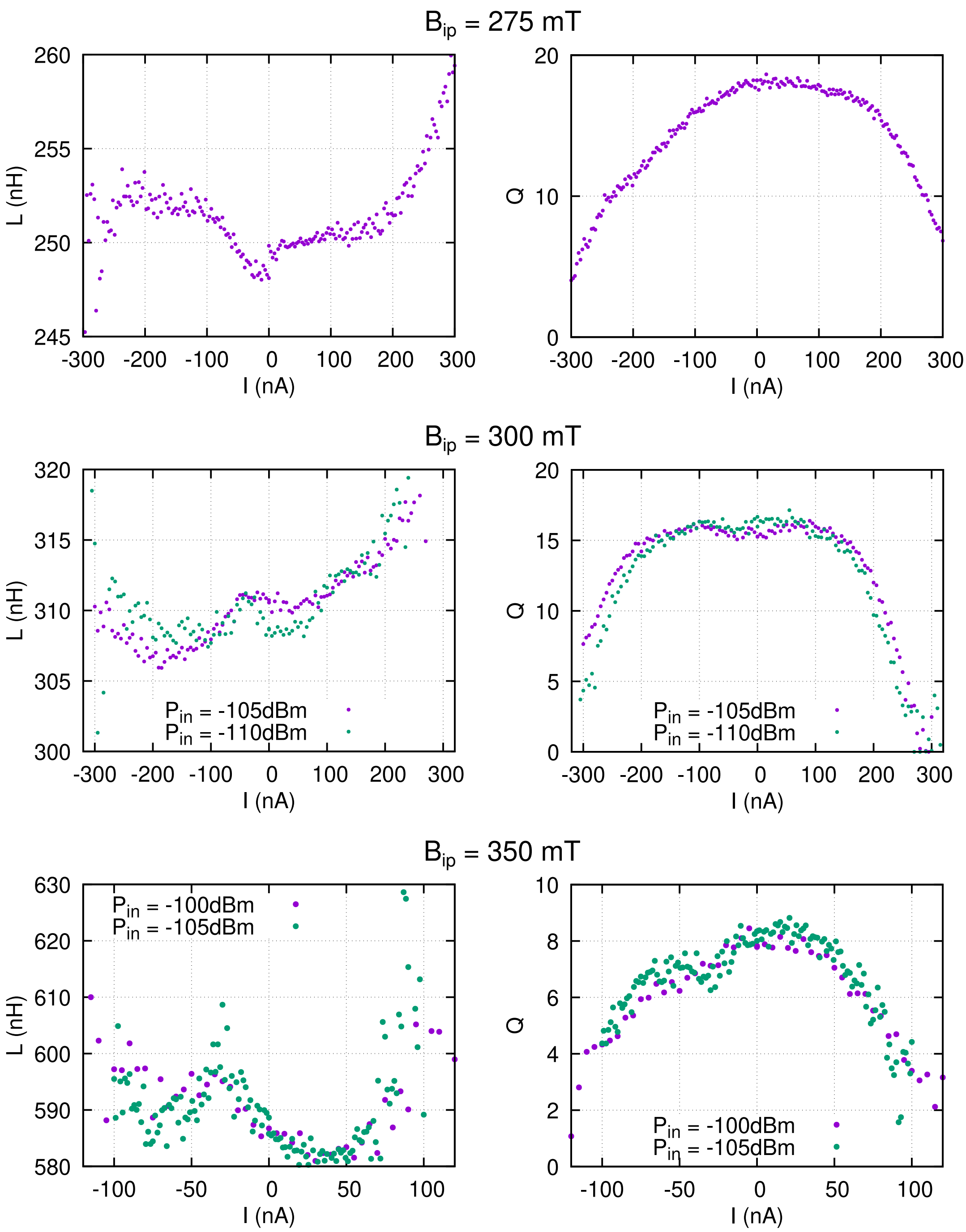

Fig. D.1.: Measurements of $L(I)$ and $Q(I)$ at zero out-of-plane field at $T \sim 100\,\mathrm{mK}$.

Bibliography

[1] Alex de Vries. "The growing energy footprint of artificial intelligence". In: *Joule* 7.10 (Oct. 2023), pp. 2191–2194. ISSN: 2542-4785. DOI: 10.1016/j.joule.2023.09.004. URL: https://doi.org/10.1016/j.joule.2023.09.004.

[2] Neil C. Thompson and Svenja Spanuth. "The decline of computers as a general purpose technology". In: *Commun. ACM* 64.3 (Feb. 2021), pp. 64–72. ISSN: 0001-0782. DOI: 10.1145/3430936. URL: https://doi.org/10.1145/3430936.

[3] Charles E. Leiserson et al. "There's plenty of room at the Top: What will drive computer performance after Moore's law?" In: *Science* 368.6495 (2020), eaam9744. DOI: 10.1126/science.aam9744. eprint: https://www.science.org/doi/pdf/10.1126/science.aam9744. URL: https://www.science.org/doi/abs/10.1126/science.aam9744.

[4] IEEE International Roadmap for Devices and Systems. *Cryogenic Electronics and Quantum Information Processing*. en. 2023. DOI: 10.60627/042B-J892. URL: https://irds.ieee.org/images/files/pdf/2023/2023_IRDS_CEQIP.pdf.

[5] B. D. Josephson. "Possible new effects in superconductive tunnelling". In: *Phys. Lett.* 1.7 (1962), pp. 251–253. URL: http://linkinghub.elsevier.com/retrieve/pii/0031916362913690.

[6] Naoki Takeuchi et al. "Adiabatic Quantum-Flux-Parametron: A Tutorial Review". In: *IEICE Transactions on Electronics* 105.6 (June 2022), pp. 251–263. DOI: 10.1587/transele.2021SEP0003.

[7] R. Landauer. "Irreversibility and Heat Generation in the Computing Process". In: *IBM Journal of Research and Development* 5.3 (1961), pp. 183–191. DOI: 10.1147/rd.53.0183.

[8] Naoki Takeuchi et al. "An adiabatic superconductor 8-bit adder with 24kBT energy dissipation per junction". In: *Applied Physics Letters* 114.4 (Jan. 2019), p. 042602. ISSN: 0003-6951. DOI: 10.1063/1.5080753. eprint: https://pubs.aip.org/aip/apl/article-pdf/doi/10.1063/1.5080753/13036671/042602_1_online.pdf. URL: https://doi.org/10.1063/1.5080753.

[9] E. Bauer et al. "Heavy Fermion Superconductivity and Magnetic Order in Noncentrosymmetric $CePt_3Si$". In: *Phys. Rev. Lett.* 92 (2 Jan. 2004), p. 027003. DOI: 10.1103/PhysRevLett.92.027003. URL: https://link.aps.org/doi/10.1103/PhysRevLett.92.027003.

[10] Fuyuki Ando et al. "Observation of superconducting diode effect". In: *Nature* 584.7821 (Aug. 2020), pp. 373–376. ISSN: 1476-4687. DOI: 10.1038/s41586-020-2590-4. URL: https://doi.org/10.1038/s41586-020-2590-4.

[11] José A. Flores-Livas et al. "A perspective on conventional high-temperature superconductors at high pressure: Methods and materials". In: *Physics Reports* 856 (2020). A perspective on conventional high-temperature superconductors at high pressure: Methods and materials, pp. 1–78. ISSN: 0370-1573. DOI: https://doi.org/10.1016/j.physrep.2020.02.003. URL: https://www.sciencedirect.com/science/article/pii/S0370157320300363.

[12] Christian Baumgartner et al. "Supercurrent rectification and magnetochiral effects in symmetric Josephson junctions". In: *Nature Nanotechnology* 17.1 (Jan. 2022), pp. 39–44. ISSN: 1748-3395. DOI: 10.1038/s41565-021-01009-9. URL: https://doi.org/10.1038/s41565-021-01009-9.

[13] Michael Tinkham. *Introduction to Superconductivity: Second Edition (Dover Books on Physics) (Vol i)*. 2nd ed. Dover Publications, June 2004. ISBN: 0486435032. URL: http://www.worldcat.org/isbn/0486435032.

[14] Daniel Gall. "Electron mean free path in elemental metals". In: *Journal of Applied Physics* 119.8 (Feb. 2016), p. 085101. ISSN: 0021-8979. DOI: 10.1063/1.4942216. eprint: https://pubs.aip.org/aip/jap/article-pdf/doi/10.1063/1.4942216/15177542/085101_1_online.pdf. URL: https://doi.org/10.1063/1.4942216.

[15] I. O. Kulik and A. N. Omel'yanchuk. "Contribution to the microscopic theory of the Josephson effect in superconducting bridges". In: *JETP Lett. (USSR) (Engl. Transl.), v. 21, no. 4, pp. 96-97* (Feb. 1975). URL: https://www.osti.gov/biblio/4209268.

[16] K. K. Likharev. "Superconducting weak links". In: *Rev. Mod. Phys.* 51 (1 Jan. 1979), pp. 101–159. DOI: 10.1103/RevModPhys.51.101. URL: https://link.aps.org/doi/10.1103/RevModPhys.51.101.

[17] A. A. Golubov, M. Yu. Kupriyanov, and E. Il'ichev. "The current-phase relation in Josephson junctions". In: *Rev. Mod. Phys.* 76 (2 Apr. 2004), pp. 411–469. DOI: 10.1103/RevModPhys.76.411. URL: https://link.aps.org/doi/10.1103/RevModPhys.76.411.

[18] W. Haberkorn, H. Knauer, and J. Richter. "A theoretical study of the current-phase relation in Josephson contacts". In: *physica status solidi (a)* 47.2 (1978), K161–K164. DOI: https://doi.org/10.1002/pssa.2210470266. eprint: https://onlinelibrary.wiley.com/doi/pdf/10.1002/pssa.2210470266. URL: https://onlinelibrary.wiley.com/doi/abs/10.1002/pssa.2210470266.

[19] Akira Furusaki and Masaru Tsukada. "A unified theory of clean Josephson junctions". In: *Physica B: Condensed Matter* 165-166 (1990). LT-19, pp. 967–968. ISSN: 0921-4526. DOI: https://doi.org/10.1016/S0921-4526(09)80069-0. URL: https://www.sciencedirect.com/science/article/pii/S0921452609800690.

[20] Akira Furusaki, Hideaki Takayanagi, and Masaru Tsukada. "Josephson effect of the superconducting quantum point contact". In: *Phys. Rev. B* 45 (18 May 1992), pp. 10563–10575. DOI: 10.1103/PhysRevB.45.10563. URL: https://link.aps.org/doi/10.1103/PhysRevB.45.10563.

[21] C. W. J. Beenakker. *Three "Universal" Mesoscopic Josephson Effects.* Ed. by Hidetoshi Fukuyama and Tsuneya Ando. Berlin, Heidelberg: Springer Berlin Heidelberg, 1992, pp. 235–253. ISBN: 978-3-642-84818-6.

[22] Yu. V. Nazarov. "Limits of universality in disordered conductors". In: *Phys. Rev. Lett.* 73 (1 July 1994), pp. 134–137. DOI: 10.1103/PhysRevLett.73.134. URL: https://link.aps.org/doi/10.1103/PhysRevLett.73.134.

[23] A. Manchon et al. "New perspectives for Rashba spin–orbit coupling". In: *Nature Materials* 14.9 (Sept. 2015), pp. 871–882. ISSN: 1476-4660. DOI: 10.1038/nmat4360. URL: https://doi.org/10.1038/nmat4360.

[24] A. Buzdin. "Direct Coupling Between Magnetism and Superconducting Current in the Josephson φ_0 Junction". In: *Phys. Rev. Lett.* 101 (10 Sept. 2008), p. 107005. DOI: 10.1103/PhysRevLett.101.107005. URL: https://link.aps.org/doi/10.1103/PhysRevLett.101.107005.

[25] F S Bergeret and I V Tokatly. "Theory of diffusive φ_0 Josephson junctions in the presence of spin-orbit coupling". In: (Sept. 2014). arXiv: 1409.4563 [cond-mat.supr-con].

[26] Francois Konschelle, Ilya V. Tokatly, and F. Sebastián Bergeret. "Theory of the spin-galvanic effect and the anomalous phase shift φ_0 in superconductors and Josephson junctions with intrinsic spin-orbit coupling". In: *Phys. Rev. B* 92 (12 Sept. 2015), p. 125443. DOI: 10.1103/PhysRevB.92.125443. URL: https://link.aps.org/doi/10.1103/PhysRevB.92.125443.

[27] Stefan Ilic et al. "Superconducting diode effect in diffusive superconductors and Josephson junctions with Rashba spin-orbit coupling". In: *Phys. Rev. B* 110 (14 Oct. 2024), p. L140501. DOI: 10.1103/PhysRevB.110.L140501. URL: https://link.aps.org/doi/10.1103/PhysRevB.110.L140501.

[28] Andreas Costa, Jaroslav Fabian, and Denis Kochan. "Microscopic study of the Josephson supercurrent diode effect in Josephson junctions based on two-dimensional electron gas". In: *Phys. Rev. B* 108 (5 Aug. 2023), p. 054522. DOI: 10.1103/PhysRevB.108.054522. URL: https://link.aps.org/doi/10.1103/PhysRevB.108.054522.

[29] Ramón Aguado. "Majorana quasiparticles in condensed matter". In: *La Rivista del Nuovo Cimento* 40.11 (Nov. 2017), pp. 523–593. ISSN: 1826-9850. DOI: 10.1393/ncr/i2017-10141-9. URL: https://doi.org/10.1393/ncr/i2017-10141-9.

[30] William Mayer et al. "Superconducting Proximity Effect in InAsSb Surface Quantum Wells with In Situ Al Contacts". In: *ACS Appl. Electron. Mater.* 2.8 (Aug. 2020), pp. 2351–2356. ISSN: 2637-6113. DOI: 10.1021/acsaelm.0c00269. URL: https://pubs.acs.org/doi/10.1021/acsaelm.0c00269.

[31] Kaushini S. Wickramasinghe et al. "Transport properties of near surface InAs two-dimensional heterostructures". In: *Applied Physics Letters* 113.26 (Dec. 2018), p. 262104. ISSN: 0003-6951. DOI: 10.1063/1.5050413. eprint: https://pubs.aip.org/aip/apl/article-pdf/doi/10.1063/1.5050413/14521159/262104_1_online.pdf. URL: https://doi.org/10.1063/1.5050413.

[32] Teng Zhang et al. "Mobility exceeding 100 000 cm^2/V s in modulation-doped shallow InAs quantum wells coupled to epitaxial aluminum". In: *Phys. Rev. Mater.* 7 (5 May 2023), p. 056201. DOI: 10.1103/PhysRevMaterials.7.056201. URL: https://link.aps.org/doi/10.1103/PhysRevMaterials.7.056201.

[33] Tomohiro Yokoyama, Mikio Eto, and Yuli V. Nazarov. "Josephson Current through Semiconductor Nanowire with Spin–Orbit Interaction in Magnetic Field". In: *Journal of the Physical Society of Japan* 82.5 (2013), p. 054703. DOI: 10.7566/JPSJ.82.054703. eprint: https://doi.org/10.7566/JPSJ.82.054703. URL: https://doi.org/10.7566/JPSJ.82.054703.

[34] Tomohiro Yokoyama, Mikio Eto, and Yuli V. Nazarov. "Anomalous Josephson effect induced by spin-orbit interaction and Zeeman effect in semiconductor nanowires". In: *Phys. Rev. B* 89 (19 May 2014), p. 195407. DOI: 10.1103/PhysRevB.89.195407. URL: https://link.aps.org/doi/10.1103/PhysRevB.89.195407.

[35] A. Costa et al. "Sign reversal of the Josephson inductance magnetochiral anisotropy and 0–π-like transitions in supercurrent diodes". In: *Nature Nanotechnology* 18.11 (Nov. 2023), pp. 1266–1272. ISSN: 1748-3395. DOI: 10.1038/s41565-023-01451-x. URL: https://doi.org/10.1038/s41565-023-01451-x.

[36] Neda Lotfizadeh et al. "Superconducting diode effect sign change in epitaxial Al-InAs Josephson junctions". In: *Communications Physics* 7.1 (Apr. 2024), p. 120. ISSN: 2399-3650. DOI: 10.1038/s42005-024-01618-5. URL: https://doi.org/10.1038/s42005-024-01618-5.

[37] Christian Baumgartner. *Semiconductor-Superconductor Josephson Junctions in the Presence of Zeeman and Spin-Orbit Fields*. Aug. 2023. URL: https://epub.uni-regensburg.de/52717/.

[38] S. Reinhardt et al. "Link between supercurrent diode and anomalous Josephson effect revealed by gate-controlled interferometry". In: *Nature Communications* 15.1 (May 2024), p. 4413. ISSN: 2041-1723. DOI: 10.1038/s41467-024-48741-z. URL: https://doi.org/10.1038/s41467-024-48741-z.

[39] Abhiram Soori. "Josephson diode effect in one-dimensional quantum wires connected to superconductors with mixed singlet-triplet pairing". In: (2024). eprint: arXiv:2409.02794.

[40] M Smidman et al. "Superconductivity and spin–orbit coupling in non-centrosymmetric materials: a review". In: *Reports on Progress in Physics* 80.3 (Jan. 2017), p. 036501. DOI: 10.1088/1361-6633/80/3/036501. URL: https://dx.doi.org/10.1088/1361-6633/80/3/036501.

[41] J.D. Jackson. *Classical Electrodynamics*. Wiley, 1999. ISBN: 0-471-30932-X.

[42] William Mayer et al. "Gate controlled anomalous phase shift in Al/InAs Josephson junctions". In: *Nature Communications* 11.1 (Jan. 2020), p. 212. ISSN: 2041-1723. DOI: 10.1038/s41467-019-14094-1. URL: https://doi.org/10.1038/s41467-019-14094-1.

[43] Matthieu C. Dartiailh et al. "Phase Signature of Topological Transition in Josephson Junctions". In: *Phys. Rev. Lett.* 126.3 (Jan. 2021), p. 036802. DOI: 10.1103/PhysRevLett.126.036802. URL: https://link.aps.org/doi/10.1103/PhysRevLett.126.036802.

[44] G.P. Mazur et al. "Gate-tunable Josephson diode". In: *Phys. Rev. Appl.* 22 (5 Nov. 2024), p. 054034. DOI: 10.1103/PhysRevApplied.22.054034. URL: https://link.aps.org/doi/10.1103/PhysRevApplied.22.054034.

[45] Simon Reinhardt et al. "Magnetochiral vortex ratchet effect in two-dimensional arrays of φ_0-Josephson junctions". In: (June 2024). arXiv: 2406.13819 [cond-mat.supr-con].

[46] Richard S Newrock et al. "The two-dimensional physics of Josephson junction arrays". In: *Journal of Physics C: Solid State Physics* 54 (2000), pp. 263–512. URL: https://api.semanticscholar.org/CorpusID:119006266.

[47] Joseph P. Straley and George Michael Barnett. "Phase diagram for a Josephson network in a magnetic field". In: *Phys. Rev. B* 48 (5 Aug. 1993), pp. 3309–3315. DOI: 10.1103/PhysRevB.48.3309. URL: https://link.aps.org/doi/10.1103/PhysRevB.48.3309.

[48] Martijn Lankhorst et al. "Annealed Low Energy States in Frustrated Large Square Josephson Junction Arrays". In: *Condensed Matter* 3.2 (2018). ISSN: 2410-3896. DOI: 10.3390/condmat3020019. URL: https://www.mdpi.com/2410-3896/3/2/19.

[49] S. Teitel and C. Jayaprakash. "Josephson-Junction Arrays in Transverse Magnetic Fields". In: *Phys. Rev. Lett.* 51 (21 Nov. 1983), pp. 1999–2002. DOI: 10.1103/PhysRevLett.51.1999. URL: https://link.aps.org/doi/10.1103/PhysRevLett.51.1999.

[50] Prashant Chauhan et al. "Measurements of cyclotron resonance of the interfacial states in strong spin–orbit coupled 2D electron gases proximitized with aluminum". In: *Applied Physics Letters* 120.14 (Apr. 2022), p. 142105. ISSN: 0003-6951. DOI: 10.1063/5.0087401. eprint: https://pubs.aip.org/aip/apl/article-pdf/doi/10.1063/5.0087401/16446060/142105_1_online.pdf. URL: https://doi.org/10.1063/5.0087401.

[51] G. L. J. A. Rikken et al. "Two-terminal resistance of quantum Hall devices". In: *Phys. Rev. B* 37 (11 Apr. 1988), pp. 6181–6186. DOI: 10.1103/PhysRevB.37.6181. URL: https://link.aps.org/doi/10.1103/PhysRevB.37.6181.

[52] Dhavala Suri et al. "Non-reciprocity of vortex-limited critical current in conventional superconducting micro-bridges". In: *Applied Physics Letters* 121.10 (2022), p. 102601. DOI: 10.1063/5.0109753. eprint: https://doi.org/10.1063/5.0109753. URL: https://doi.org/10.1063/5.0109753.

[53] Yasen Hou et al. "Ubiquitous Superconducting Diode Effect in Superconductor Thin Films". In: *Phys. Rev. Lett.* 131 (2 July 2023), p. 027001. DOI: 10.1103/PhysRevLett.131.027001. URL: https://link.aps.org/doi/10.1103/PhysRevLett.131.027001.

[54] Ryohei Wakatsuki et al. "Nonreciprocal charge transport in noncentrosymmetric superconductors". In: *Science Advances* 3.4 (2017), e1602390.

[55] Shintaro Hoshino et al. "Nonreciprocal charge transport in two-dimensional noncentrosymmetric superconductors". In: *Phys. Rev. B* 98 (5 Aug. 2018), p. 054510. DOI: 10.1103/PhysRevB.98.054510. URL: https://link.aps.org/doi/10.1103/PhysRevB.98.054510.

[56] W. Gillijns et al. "Origin of Reversed Vortex Ratchet Motion". In: *Phys. Rev. Lett.* 99 (24 Dec. 2007), p. 247002. DOI: 10.1103/PhysRevLett.99.247002. URL: https://link.aps.org/doi/10.1103/PhysRevLett.99.247002.

[57] D. E. Shalóm and H. Pastoriza. "Vortex Motion Rectification in Josephson Junction Arrays with a Ratchet Potential". In: *Phys. Rev. Lett.* 94 (17 May 2005), p. 177001. DOI: 10.1103/PhysRevLett.94.177001. URL: https://link.aps.org/doi/10.1103/PhysRevLett.94.177001.

[58] Verónica I. Marconi. "Rocking Ratchets in Two-Dimensional Josephson Networks: Collective Effects and Current Reversal". In: *Phys. Rev. Lett.* 98 (4 Jan. 2007), p. 047006. DOI: 10.1103/PhysRevLett.98.047006. URL: https://link.aps.org/doi/10.1103/PhysRevLett.98.047006.

[59] J. E. Villegas et al. "A Superconducting Reversible Rectifier That Controls the Motion of Magnetic Flux Quanta". In: *Science* 302.5648 (2003), pp. 1188–1191. DOI: 10.1126/science.1090390. eprint: https://www.science.org/doi/pdf/10.1126/science.1090390. URL: https://www.science.org/doi/abs/10.1126/science.1090390.

[60] Clécio C. de Souza Silva et al. "Controlled multiple reversals of a ratchet effect". In: *Nature* 440.7084 (Mar. 2006), pp. 651–654. ISSN: 1476-4687. DOI: 10.1038/nature04595. URL: https://doi.org/10.1038/nature04595.

[61] Qiming Lu, C. J. Olson Reichhardt, and C. Reichhardt. "Reversible vortex ratchet effects and ordering in superconductors with simple asymmetric potential arrays". In: *Phys. Rev. B* 75 (5 Feb. 2007), p. 054502. DOI: 10.1103/PhysRevB.75.054502. URL: https://link.aps.org/doi/10.1103/PhysRevB.75.054502.

[62] Alexander-Georg Penner et al. "Resistivity Tensor of Vortex-Lattice States in Josephson Junction Arrays". In: *Phys. Rev. Lett.* 131 (20 Nov. 2023), p. 206001. DOI: 10.1103/PhysRevLett.131.206001. URL: https://link.aps.org/doi/10.1103/PhysRevLett.131.206001.

[63] L. Fuchs et al. "Anisotropic Vortex Squeezing in Synthetic Rashba Superconductors: A Manifestation of Lifshitz Invariants". In: *Phys. Rev. X* 12 (4 Nov. 2022), p. 041020. DOI: 10.1103/PhysRevX.12.041020. URL: https://link.aps.org/doi/10.1103/PhysRevX.12.041020.

[64] M. S. Rzchowski et al. "Vortex pinning in Josephson-junction arrays". In: *Phys. Rev. B* 42 (4 Aug. 1990), pp. 2041–2050. DOI: 10.1103/PhysRevB.42.2041. URL: https://link.aps.org/doi/10.1103/PhysRevB.42.2041.

[65] Rosario Fazio and Herre van der Zant. "Quantum phase transitions and vortex dynamics in superconducting networks". In: *Physics Reports* 355.4 (2001), pp. 235–334. ISSN: 0370-1573. DOI: https://doi.org/10.1016/S0370-1573(01)00022-9. URL: https://www.sciencedirect.com/science/article/pii/S0370157301000229.

[66] Yuli V. Nazarov and Yaroslav M. Blanter. *Quantum Transport: Introduction to Nanoscience*. Cambridge University Press, 2009.

[67] Albert Schmid. "Diffusion and Localization in a Dissipative Quantum System". In: *Phys. Rev. Lett.* 51 (17 Oct. 1983), pp. 1506–1509. DOI: 10.1103/PhysRevLett.51.1506. URL: https://link.aps.org/doi/10.1103/PhysRevLett.51.1506.

[68] S. A. Bulgadaev. "Phase diagram of a dissipative quantum system". In: *JETP Letters* 39 (6 1984), p. 264. URL: http://jetpletters.ru/ps/0/article_19477.shtml.

[69] A. Murani et al. "Absence of a Dissipative Quantum Phase Transition in Josephson Junctions". In: *Phys. Rev. X* 10 (2 Apr. 2020), p. 021003. DOI: 10.1103/PhysRevX.10.021003. URL: https://link.aps.org/doi/10.1103/PhysRevX.10.021003.

[70] Roman Kuzmin et al. "Observation of the Schmid-Bulgadaev dissipative quantum phase transition". In: (Apr. 2023). arXiv: 2304.05806 [quant-ph].

[71] Manuel Houzet, Tsuyoshi Yamamoto, and Leonid I. Glazman. “Microwave spectroscopy of the Schmid transition”. In: *Phys. Rev. B* 109 (15 Apr. 2024), p. 155431. DOI: 10.1103/PhysRevB.109.155431. URL: https://link.aps.org/doi/10.1103/PhysRevB.109.155431.

[72] Nicolas Paris et al. “Resilience of the quantum critical line in the Schmid transition”. In: (July 2024). arXiv: 2407.01699 [cond-mat.str-el].

[73] A. Alan Middleton and Ned S. Wingreen. “Collective transport in arrays of small metallic dots”. In: *Phys. Rev. Lett.* 71 (19 Nov. 1993), pp. 3198–3201. DOI: 10.1103/PhysRevLett.71.3198. URL: https://link.aps.org/doi/10.1103/PhysRevLett.71.3198.

[74] M.D. Groner et al. “Electrical characterization of thin Al2O3 films grown by atomic layer deposition on silicon and various metal substrates”. In: *Thin Solid Films* 413.1 (2002), pp. 186–197. ISSN: 0040-6090. DOI: https://doi.org/10.1016/S0040-6090(02)00438-8. URL: https://www.sciencedirect.com/science/article/pii/S0040609002004388.

[75] Daniel M. Kaplan, Victor A. Sverdlov, and Konstantin K. Likharev. “Coulomb gap, Coulomb blockade, and dynamic activation energy in frustrated single-electron arrays”. In: *Phys. Rev. B* 68 (4 July 2003), p. 045321. DOI: 10.1103/PhysRevB.68.045321. URL: https://link.aps.org/doi/10.1103/PhysRevB.68.045321.

[76] K. B. Efetov and A. Tschersich. “Coulomb effects in granular materials at not very low temperatures”. In: *Phys. Rev. B* 67 (17 May 2003), p. 174205. DOI: 10.1103/PhysRevB.67.174205. URL: https://link.aps.org/doi/10.1103/PhysRevB.67.174205.

[77] C. G. L. Bøttcher et al. “Superconducting, insulating and anomalous metallic regimes in a gated two-dimensional semiconductor–superconductor array”. In: *Nature Physics* 14.11 (Nov. 2018), pp. 1138–1144. ISSN: 1745-2481. DOI: 10.1038/s41567-018-0259-9. URL: https://doi.org/10.1038/s41567-018-0259-9.

[78] T. S. Tighe et al. “Measurements of charge soliton motion in two-dimensional arrays of ultrasmall Josephson junctions”. In: *Phys. Rev. B* 47 (2 Jan. 1993), pp. 1145–1148. DOI: 10.1103/PhysRevB.47.1145. URL: https://link.aps.org/doi/10.1103/PhysRevB.47.1145.

[79] P. Delsing et al. “Thermal activation and injection of charge solitons in 2D-arrays of small Josephson junctions.” In: *Physica B: Condensed Matter* 194-196 (1994), pp. 993–994. ISSN: 0921-4526. DOI: https://doi.org/10.1016/0921-4526(94)90826-5. URL: https://www.sciencedirect.com/science/article/pii/0921452694908265.

[80] P. Delsing et al. “Charge solitons and quantum fluctuations in two-dimensional arrays of small Josephson junctions”. In: *Phys. Rev. B* 50 (6 Aug. 1994), pp. 3959–3971. DOI: 10.1103/PhysRevB.50.3959. URL: https://link.aps.org/doi/10.1103/PhysRevB.50.3959.

[81] E. Šimánek. “Origin of the resistivity minima in granular superconductors”. In: *Phys. Rev. B* 25 (1 Jan. 1982), pp. 237–244. DOI: 10.1103/PhysRevB.25.237. URL: https://link.aps.org/doi/10.1103/PhysRevB.25.237.

[82] M. T. Tuominen et al. “Experimental evidence for parity-based 2e periodicity in a superconducting single-electron tunneling transistor”. In: *Phys. Rev. Lett.* 69 (13 Nov. 1992), pp. 1997–2000. DOI: 10.1103/PhysRevLett.69.1997. URL: https://link.aps.org/doi/10.1103/PhysRevLett.69.1997.

[83] M. V. Feigel’man, S. E. Korshunov, and A. B. Pugachev. “Parity effect and charge-binding transition in submicron Josephson junction arrays”. In: *Journal of Experimental and Theoretical Physics Letters* 65.7 (Apr. 1997), pp. 566–571. ISSN: 1090-6487. DOI: 10.1134/1.567397. URL: https://doi.org/10.1134/1.567397.

[84] Hiroki Ikegami and Yasunobu Nakamura. “Insulating phase in two-dimensional Josephson junction arrays investigated by nonlinear transport”. In: *Phys. Rev. B* 106 (18 Nov. 2022), p. 184511. DOI: 10.1103/PhysRevB.106.184511. URL: https://link.aps.org/doi/10.1103/PhysRevB.106.184511.

[85] M. Kjaergaard et al. “Quantized conductance doubling and hard gap in a two-dimensional semiconductor–superconductor heterostructure”. In: *Nature Communications* 7.1 (Sept. 2016), p. 12841. ISSN: 2041-1723. DOI: 10.1038/ncomms12841. URL: https://doi.org/10.1038/ncomms12841.

[86] Christian Baumgartner et al. “Josephson Inductance as a Probe for Highly Ballistic Semiconductor-Superconductor Weak Links”. In: *Phys. Rev. Lett.* 126 (3 Jan. 2021), p. 037001. DOI: 10.1103/PhysRevLett.126.037001. URL: https://link.aps.org/doi/10.1103/PhysRevLett.126.037001.

[87] Qingzhen Wang et al. *Spatial dependence of local density of states in semiconductor-superconductor hybrids.* 2024. eprint: https://arxiv.org/abs/2406.06410.

[88] Joseph Yuan et al. “Experimental measurements of effective mass in near-surface InAs quantum wells”. In: *Phys. Rev. B* 101 (20 May 2020), p. 205310. DOI: 10.1103/PhysRevB.101.205310. URL: https://link.aps.org/doi/10.1103/PhysRevB.101.205310.

[89] Akira Sato and Akio Iwasa. “Non-temperature dependent resistor at low temperatures”. In: *Physica B: Condensed Matter* 329-333 (2003). Proceedings of the 23rd International Conference on Low Temperature Physics, pp. 1660–1661. ISSN: 0921-4526. DOI: https://doi.org/10.1016/S0921-4526(02)02452-3. URL: https://www.sciencedirect.com/science/article/pii/S0921452602024523.

[90] S. Reinhardt et al. “Lab::Measurement—A portable and extensible framework for controlling lab equipment and conducting measurements”. In: *Computer Physics Communications* 234 (2019), pp. 216–222. ISSN: 0010-4655. DOI: https://doi.org/10.1016/j.cpc.2018.07.024. URL: https://www.sciencedirect.com/science/article/pii/S0010465518302819.

[91] F. Pobell. *Matter and Methods at Low Temperatures*. Springer Berlin Heidelberg, 2007. ISBN: 9783540463603. URL: https://books.google.de/books?id=mRZ0uPfiWTQC.

[92] M. Göppl et al. "Coplanar waveguide resonators for circuit quantum electrodynamics". In: *Journal of Applied Physics* 104.11 (Dec. 2008), p. 113904. ISSN: 0021-8979. DOI: 10.1063/1.3010859. eprint: https://pubs.aip.org/aip/jap/article-pdf/doi/10.1063/1.3010859/14109820/113904_1_online.pdf. URL: https://doi.org/10.1063/1.3010859.

[93] David M Pozar. *Microwave engineering; 3rd ed.* Hoboken, NJ: Wiley, 2005.

[94] Benjamin A. Mazin. "Microwave Kinetic Inductance Detectors". PhD thesis. California Institute of Technology, 2005. DOI: 10.7907/GZ72-V784. URL: https://resolver.caltech.edu/CaltechETD:etd-10042004-120707.

E. Acknowledgments

Work in experimental physics research is a team effort, and none of the results would have been possible without the continuous support of colleagues, students, and technicians. A supportive environment is key to make it through the ups and downs of a doctoral thesis. I would like to thank everyone from our group and the chair for supporting me and for making my time in the group so enjoyable.

In particular I would like to thank

- My advisor Prof. Dr. Christoph Strunk for allowing me to work in his group, giving me the time and freedom to work on my ideas and for always being open minded to new ideas. Thank you also for allowing me attend so many international conferences and workshops, the trips to Japan, Montenegro, Slovakia, and Denmark were very inspiring and motivating. Thank you also for the support and advice with the challenge of finding a postdoc position abroad.

- Dr. Nicola Paradiso for co-supervising this thesis and for the many discussions about experiments and data. Thank you also for the pleasant teamwork on papers and for keeping an optimistic mindset in every situation.

- My fellow phd students Lorenz Fuchs and Christian Baumgartner for motivating me to join the work group and for laying the groundwork of semiconductor-superconductor research in our group. Your great work certainly provided a great boost to my research.

- Prof. Dr. Jaroslav Fabian for co-refereeing this thesis.

- Prof. Dr. Jaroslav Fabian, Prof. Dr. Denis Kochan, and Dr. Andreas Costa for the theory support and the close long time collaboration. Thank you also for the nice workshop and activities in Bratislava.

- Dr. Andreas Costa for proofreading the theory chapter of this thesis

- Prof. Dr. Dieter Weiss for allowing me to work at his chair, for providing the clean room and other infrastructure, and for creating such a great environment for scientific research.

- Prof. Dr. Michael J. Manfra and his group for providing the Al/InAs material of outstanding quality, which made this work possible.

- Prof. Dr. Felix von Oppen, Prof. Dr. Leonid Glazman, and Alexander Penner for the theoretical work on the vortex ratchet effect. Thank you also for the enjoyable time at FU Berlin and the fruitful discussions.

- Alexander Penner for many discussions on the modeling of the vortex ratchet effect and for the extensive work on numerical simulations.

- My students Josua Thieme, Hannes Schmid, Leo Pfaffinger, and Tim Ascherl for the great work and the nice times together in the lab.

- Our secretaries Elke Haushalter and Claudia Moser for the help in many situations and for the support with all bureaucratic affairs, and for always having an open ear for any kind of problem.

- All members of our group, especially Thomas Huber, Alexander Weitzel, Lorenz Bauriedl, Johanna Berger, Lea Pfaffinger, Jay Schmidt, Simon Feyrer and Dr. Leandro Tosi for the time together at work, many tasty cakes, and also for many outdoor and indoor activities outside of the physics world.

- Christian Haimerl and Thomas Solleder for the continuous and reliable supply with liquid helium and nitrogen.

- Our group's technician Tom Haller for the help with many technical problems and for his advise on many engineering challenges.

- Dieter Riedl and Monika Meier and all the other members of the Electrical and the Mechanical workshops for the friendly attitude despite my many odd requests and for all the rapid and reliable work on many projects.

- My family and friends for the support during the last five years.